Reviews of Modern Plasma Physics (2024) 8:5
https://doi.org/10.1007/s41614-023-00138-z

REVIEW PAPER

Transport from electron-scale turbulence in toroidal magnetic confinement devices

Y. Ren[1] · W. Guttenfelder[1] · S. M. Kaye[1] · W. X. Wang[1]

Received: 21 February 2022 / Accepted: 21 November 2023

Abstract

Plasma transport driven by turbulence ultimately determines the energy confinement performance of controlled fusion devices regardless of their confinement schemes and configurations. A large variety of plasma instabilities have been proposed for driving turbulence responsible for anomalous plasma transport beyond classical/neoclassical transport due to collisions. Although ion-scale turbulence usually dominates due to its large eddy size and saturation level, electron-scale turbulence has been recognized to be important in regions where ion-scale turbulence is suppressed (e.g., in internal transport barrier and in spherical tokamak H-mode plasmas) or is close to marginality. Electron-scale turbulence has been shown to nonlinearly interact with ion-scale turbulence, which modifies the dynamics of both and affects the resulting plasma transport, particularly when ion-scale instability is weakly driven. In this review paper, we focus on electron-scale turbulence that is believed to operate in magnetically confinement fusion devices and aim to provide a review of theoretical, numerical, and experimental developments in understanding electron-scale turbulence and its role in driving anomalous plasma turbulence. In particular, we focus on the electrostatic electron temperature gradient (ETG) mode which is the most widely recognized plasma instability underlying electron-scale turbulence observed in magnetically confined plasmas. We note that there are other less studied instabilities that might be responsible for observed electron-scale turbulence, most notably ubiquitous mode, and short-wavelength ion temperature gradient (SWITG) mode, which will be briefly touched on in this review.

Keywords Electron-scale turbulence · Energy confinement · Plasma thermal transport · Toroidal magnetic confinement devices

---

Y. Ren
yren@pppl.gov

[1] Princeton Plasma Physics Laboratory, Princeton, NJ 08543, USA

1 Introduction

Plasma turbulence is widely recognized as a major mechanism in driving plasma anomalous transport in controlled fusion devices (Tang 1978; ITER Physics Expert Group on Confinement et al. 1999; Gormezano 2007; Horton 1999, 2003). Given the ultimate transport limit set by classical and neoclassical transport (Braginskii 1965; Hinton and Hazeltine 1976; Chang and Hinton 1982), the energy confinement performance of future controlled fusion devices depends on how plasma turbulence can be reduced/controlled. The existence of plasma turbulence in high-temperature fusion plasmas is almost guaranteed due to the non-thermal equilibrium nature of confined high-temperature fusion plasmas where equilibrium steady-state temperature and density gradients are sources of free energy readily to drive plasma instabilities resulting in plasma turbulence. Unlike magnetohydrodynamic (MHD) instabilities that are of system (global) scale (Freidberg 1987; Furth 1963) and usually lead to macroscopic changes in the plasma, these gradient-driven instabilities are of much smaller spatial scale, e.g., at ion/electron-gyroradius scale, and lead to plasma micro-turbulence resulting in particle, momentum, and energy transports. Note that in contrast to MHD instabilities that could happen on an Alfvén transit time scale ($\sim \mu s$ for typical tokamak plasmas), the plasma macroscopic change due to micro-turbulence happens on the confinement time scale ($\sim$ ms for typical tokamak plasmas).

Since plasmas are characterized by different spatial and temporal scales, a variety of plasma instabilities with different characteristic spatial and temporal scales can be excited and result in distinct plasma turbulence. For magnetized plasmas as in magnetic confinement fusion devices, typical characteristic spatial scales are Debye length (e.g., 43 μm), electron gyroradius (e.g., 75 μm), ion gyroradius (e.g., 4.6 mm), and electron parallel mean free path (e.g., 269 m), just to name a few (the numbers in the bracket were obtained with typical tokamak parameters with electron/deuterium temperature of 1 keV, an electron density of 3×10^{13} cm^{-3}, and magnetic field strength of 1 T). Electron–ion collision frequency, ion/electron transit frequency (i.e., $v_{\rm th}k_{||}$ where $v_{\rm th}$ is the thermal velocity and $k_{||}$ is the parallel wavenumber along the equilibrium magnetic field), electron bounce frequency, and ion/electron diamagnetic frequency are some characteristic frequencies relevant to instability/turbulence characterization. Some well-known ion-scale instabilities are Ion Temperature Gradient (ITG) mode (Coppi 1967; Kadomitsev and Pogutse 1970; Horton 1981; Evensen 1998; Brower 1989; Greaves 1992; Rettig 2001), Trapped Electron Mode (TEM) (Kadomtsev and Pogutse 1967, 1969, 1971; Nordman 1990; Ernst et al. 2004; Dannert and Jenko 2005; Ernst et al. 2006; Ernst 2009), Kinetic Ballooning Modes (KBMs) (Tang 1980; Cheng 1982), and microtearing mode (MTM) (Hazeltine and Strauss 1976; Drake 1980; Guttenfelder 2011). On the other hand, the short-wavelength (electron-scale) Electron Temperature Gradient (ETG) mode (Kadomitsev and Pogutse 1970; Rozhanskii 1981; Lee 1987; Horton 1988; Jenko 2000; Dorland 2000) has been shown to be important to drive anomalous electron thermal transport. Here, characterizing instabilities according to characteristic spatial scales is not an arbitrary choice. The spatial and temporal scales of a plasma instability/turbulence are usually related to one or more of the aforementioned characteristic scales and thus are much larger or smaller than some other characteristic scales. This provides important information on the essential physics of a particular instability/turbulence. As a well-known example, the large difference between ion and electron transit frequencies makes it possible to assume adiabatic electrons in the ITG mode, which significantly simplifies analytic analysis and reduces the computational costs of numerical simulations by not treating electrons as another kinetic species. Note that the adiabatic response means that the density fluctuation of a particular species is proportional to the potential fluctuation (see Sects. 2.1.1 and 2.2.1 for more discussions on the adiabatic response).

As we have pointed out, plasma transport in toroidal confinement devices is the natural consequence of the non-equilibrium state of confined plasmas, where thermodynamic forces (e.g., temperature gradients) would drive plasma transport. In thermodynamics, phenomenological laws are used to describe the relationship between transport fluxes and thermodynamic forces, e.g., the proportionality of the diffusion flux of a substance to the concentration gradient by Fick's law. More generally, the transport fluxes are related to thermodynamic forces through the transport matrix, meaning that a particular flux would be driven by a set of thermodynamic forces, and the transport coefficients in the transport matrix would satisfy the Onsager symmetry (Onsager 1931). This also applies to magnetically confined plasmas, where analyses in Refs. (Shaing 1988; Sugama 1996) show that with a proper choice of the pairs of transport fluxes and thermodynamic forces, the flux-surface averaged quasi-linear transport matrix satisfies the Onsanger symmetry for both the neoclassical and turbulence-driven transport processes. It is also shown that because of the quasi-neutrality condition and Ampere's law, both the neoclassical and turbulence-driven particle fluxes are intrinsically ambipolar for axisymmetric systems (e.g., a tokamak). The diagonal terms of the transport matrix connect transport fluxes to their underlying gradients (e.g., particle flux to density gradient and heat flux to temperature gradient), and the off-diagonal terms of the transport matrix represent the contribution from other gradients or forces. Thus, the diffusive part of a transport flux comes from the diagonal terms, e.g., particle flux driven by density gradient, while the pinch part of the transport flux is driven by other gradients or forces and is not diffusive. As a rough estimate, the diffusive part of the transport driven by micro-turbulence often can be approximated by a random walk process where the diffusion coefficient of a transport process can be written as $\delta x^2/\delta t$ (δx is the step size of the random walk process and δt is the step time). With regard to micro-turbulence in confined plasmas, δx is the turbulence correlations length, proportional to (but larger than) ion gyroradius, ρ_i, for ion modes and electron gyroradius, ρ_e, for electron modes, and δt is the turbulence decorrelation time, taken as particle transit time, $v_{\mathrm{th(e,i)}}/qR$, around a torus (e.g., in a tokamak), where $v_{\mathrm{th(e,i)}}$ is particle thermal velocity (the e denotes electron and the subscript i denotes ion), q is the safety factor, and R is the plasma major radius. This estimated diffusion coefficient is proportional to $\sqrt{m}T^{3/2}$ where m is particle mass and T is the temperature for the particle species. It is clear that the diffusion coefficient with such a scaling would lead to a factor of $\sqrt{m_i/m_e}$ (m_i and m_e are ion mass and electron mass, respectively) larger transport flux for ion-scale turbulence than for electron-scale turbulence (assuming gradients are comparable). In terms of deuterium plasmas, the factor is about 60, and thus, it is natural to expect ion-scale turbulence to dominate in driving anomalous transport in confined plasmas. Note that this simple estimate is closely resembling the gyro-Bohm scaling in thermal diffusivity in magnetically confined plasmas in terms of temperature and mass dependencies ($\chi_{\text{gyro-Bohm}} = \chi_{\text{Bohm}}\rho/a$ where $\chi_{\text{Bohm}} = T/eB$ (e is the electron charge and B is the magnetic field strength), ρ is gyroradius, and a is the plasma minor radius) (Kadomtsev 1975). Indeed, there is plenty of evidence of the existence of ion-scale turbulence and its contribution to the majority of measured transports observed in experiments (Greaves 1992; Brower 1989; Idomura 1999; Dimits 2000). For example, studies of ITG turbulence show that turbulence-generated zonal flow is an important mechanism for ITG turbulence (Lin 1998; Diamond 2005) and there is a nonlinear upshift of ITG onset threshold (Dimits 2000) due to zonal flows compared to the linear threshold. Plenty of experimental evidence also exists for the generation of zonal flows by the ion-scale turbulence and the regulation of ion-scale turbulence by zonal flows (Fujisawa 2008). However, it is also found that electron thermal transport remains highly anomalous even when ion-scale turbulence is suppressed by large E×B shear or negative magnetic shear and ion thermal transport was reduced to the neoclassical level, e.g., inside internal transport barriers in tokamak plasmas (Kessel 1994; Shirai 1998; Stallard 1999; Akers 2003; ITER Physics Expert Group on Confinement et al. 1999; Connor 2004; Ernst et al. 2004) and also in the core region of spherical tokamak (ST) H-mode plasmas (Akers 2003; Kaye 2007a, b; Ren 2017). On the other hand, electron-scale turbulence, particularly that driven by the ETG mode could survive the E×B shear due to its higher linear growth rate, to drive observed anomalous electron thermal transport in these plasmas. As we have shown above, the obvious obstacle for electron-scale turbulence to generate large anomalous transport is its presumed small radial extent which is thought to be characterized by ρ_e (i.e., too small a step in the random walk process). A much larger radial structure beyond ρ_e is needed if ETG turbulence is to be able to generate experimentally relevant transport. Mechanisms, such as electromagnetic effects (Rozhanskii 1981; Kim and Horton 1991) and radial streamers (Jenko 2000; Dorland 2000), have been proposed. The former involves an electromagnetic structure with a spatial scale on the order of electron skin depth, c/ω_{pe} (c is the speed of light and ω_{pe} is the electron plasma frequency) which could produce, through magnetic stochasticity, the radial electron thermal transport that is similar to the Ohkawa scaling (Ohkawa 1978). The latter, the radial streamers, are radially elongated E×B drift eddies whose radial correlation length is much larger than ρ_e and could produce electron thermal transport that is multiples of the electron gyro-Bohm unit. On the other hand, ETG turbulence was found to produce experimentally relevant electron thermal transport in the H-mode pedestal region with isotropic eddies and weak zonal flows, which is thought to be a result of much larger normalized equilibrium gradients in the pedestal region than in the core region (Told 2012; Hatch 2015; Guttenfelder 2021). We note that since ETG turbulence almost exclusively drives electron thermal transport, the understanding and controlling of ETG turbulence could be important for future burning plasmas where the fusion-generated α particles mainly heat electrons.

In addition to the ETG mode, there are other temperature-gradient-driven electron-scale instabilities that can potentially drive electron thermal transport, e.g., short-wavelength ITG (SWITG) mode (Hirose 2002; Smolyakov 2002; Gao 2005; Chowdhury 2009, 2012) and ubiquitous mode (UM) (Coppi and Rewoldt 1974; Coppi and Pegoraro 1977; Migliuolo 1995; Shen 2019). We note that these modes typically are unstable at wavelengths larger than those of the ETG mode, but still significantly smaller than ion gyroradius. More recently, the magnetic-shear-stabilized universal mode (Tsang 1978; Ross and Mahajan 1978; Antonsen 1978; Lee 1980; Chen 1982) has also been shown to be unstable for a wide range of perpendicular wavenumbers, $0.7 \lesssim k_\perp \rho_i \lesssim 100$, with a relatively weak magnetic shear, i.e., $L_s/L_n \gtrsim 17$, where L_s and L_n are the scale lengths of magnetic shear and density, respectively (Landreman 2015; Helander and Plunk 2015). Driven by density gradient alone, the universal mode could be unstable in the weak shear region near the minimum point in the q profile in a tokamak plasma. However, the transport driven by the universal mode remains to be explored with nonlinear simulation. We note that among the mentioned electron-scale instabilities above, the ETG mode is the most comprehensively studied theoretically, numerically, and experimentally. We will focus on the ETG mode in the rest of the paper but will provide some discussions on other modes in Sect. 6.

This paper is organized as follows. In Sect. 2, we present theoretical and numerical aspects of the ETG mode research, focusing on explaining the ETG mode physics with simplified geometries and physical processes. We start with the most basic form of the ETG mode: a shearless slab geometry with fluid electrons and adiabatic ions (with significant simplifications in electron fluid equations) to give readers a basic picture of the slab ETG mode, followed by a heuristic derivation of the ETG mode in the toroidal geometry, showing the basic physics picture of coupling of temperature gradient and magnetic in driving the toroidal ETG mode that is most relevant to tokamak plasmas. To facilitate comparisons with experimental results, we will present the parametric dependence of the ETG mode linear threshold, which, simply expressed in analytic forms, can provide quick first-hand guidance during experiments. Furthermore, nonlinear simulations revealing the potential roles of ETG turbulence in driving electron thermal transport and its cross-scale interactions with ion-scale turbulence are also reviewed. In Sect. 3, we will be focusing on experimental aspects of ETG turbulence and electron thermal transport, including experimental methods of measuring electron-scale turbulence with emphasis on turbulence diagnostics on present fusion devices and experimental validations of ETG turbulence models in terms of linear stability, nonlinear transport levels, and, more comprehensively, turbulence characteristics coupled with turbulence diagnostic measurements. We devote Sect.4 to the ETG mode in the H-mode pedestal region, partly due to the importance of the pedestal region in determining the overall energy confinement in magnetic confinement devices and partly due to quite different linear and nonlinear characteristics of the ETG mode in the steep-gradient region of the pedestal. Finally, we will present discussions and a summary in Sect. 6, including future directions of research on electron-scale turbulence.

2 The ETG mode in theory and numerical simulations

The ETG mode has been extensively studied both analytically and numerically, and numerous results have been reported in the literature. Early studies have been focusing on various aspects of the linear stability of the ETG mode, e.g., the parametric dependence of linear growth, the parametric dependence of critical temperature gradient threshold, parallel and radial mode structures, etc. Quasilinear and mixing length techniques have been employed to estimate electron thermal transport achievable by ETG turbulence, which has been shown to be experimentally relevant. In the last decade or 2, massive nonlinear gyrokinetic simulations have been applied to ETG turbulence with realistic geometries of fusion devices, further demonstrating the relevance of ETG turbulence in determining T_e profile and confinement property of present and future tokamaks. More recently, more powerful computational power allows the simulation of ion-scale and electron-scale turbulence simultaneously, where cross-scale interactions between electron and ion-scale dynamics have been shown to be potentially important for both ion-scale and electron-scale turbulence. This finding points to the importance of developing reduced transport models taking account of cross-scale coupling for more precise predictions of the confinement performance of future devices. In this section, we will first introduce the basic physics of the ETG mode using a simple fluid model, and we will discuss a variety of improvements to the basic model which gradually drove the development of more realistic or more experimentally relevant ETG theories. We will also present some important linear aspects of the ETG mode: the parametric dependence of critical temperature gradient and linear growth rate. Finally, we will discuss nonlinear aspects of the ETG mode physics, including saturation mechanisms (particularly those that allow the ETG mode to generate experimentally relevant electron thermal transport), the role of zonal flows (which is very different from that of the ITG mode), nonlinear gyrokinetic predictions of experimentally relevant electron thermal transport with multiple codes, and cross-scale interactions between ETG and ion-scale modes.

2.1 Linear stability of the ETG mode

We will first revisit the linear stability of the ETG mode. The ETG mode, also called η_e mode, has been identified along with the ITG mode, the so-called η_i mode (Kadomitsev and Pogutse 1970), where η is the ratio between the density gradient scale length and the temperature gradient scale length. Linear stability analysis provides important information on the possible operational regime of a particular mode in experiments and thus could provide quick guidance to experiment execution and experiment planning. Although fluid equations often lack many kinetic effects as in gyro-fluid/gyrokinetic equations, e.g., kinetic damping, they are analytically easier to deal with to illustrate the essential physics of a particular instability.

2.1.1 A simple fluid model of the ETG mode in a shearless slab geometry

Here, we would like to revisit the derivation of the local fluid ETG mode in a shearless ("shearless" means that the magnetic field does not change direction) slab geometry which illustrates the essential physics of the slab ETG mode. We note that this is possibly the simplest form of the ETG mode. However, since it has the minimum physics for the slab ETG mode, it is the basis of more realistic models, e.g., in Refs.(Rozhanskii 1981; Lee 1987; Horton 1988; Hirose 1990; Shukla 1990). We closely follow a similar derivation of the slab ITG mode in Ref. (Kadomitsev and Pogutse 1970), taken into account assumptions appropriate for the ETG mode regime (it is well known that linear ETG and ITG modes are identical if non-adiabatic species are switched). We assume a uniform magnetic field in the z-direction ($\vec{B} = B_0\vec{e}_z$), all equilibrium changes in the x-direction (e.g., density and temperature), and equilibrium quantities invariant in the y direction (see Fig. 1 for the geometry). We assume that electron gyroradius, ρ_e, is much smaller than any gradient scale length, e.g., density gradient scale length ($L_n = -1/(\mathrm{d}\ln n/\mathrm{d}x)$) and temperature gradient scale length ($L_T = -1/(\mathrm{d}\ln T/\mathrm{d}x)$), where n and T are the density and temperature, respectively. We also assume cold electrons, namely $|\omega/k_z| >> v_{\mathrm{the}}$. This assumption has important implications for the electron parallel momentum equation and the electron energy balance equation, which we will detail below. For simplicity, we assume that the perturbation is electrostatic only, namely $\vec{E} = -\nabla\varphi$, where $\vec{E}$ is the perturbed electrostatic electrical field and φ is the perturbed electrostatic potential. This is a valid assumption for low β (the ratio between plasma thermal pressure and magnetic pressure) plasmas. Here, we focus on small perturbations in the form

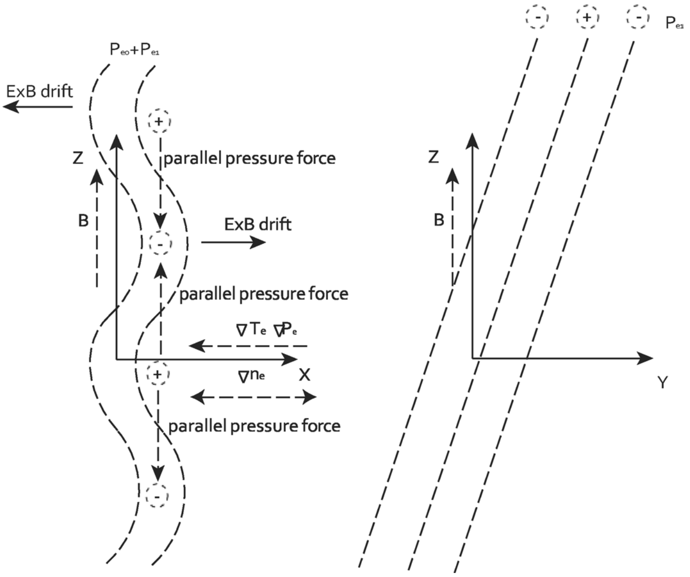

Fig. 1 A schematic of the slab ETG geometry. Left: the view in the x–z-plane (the y-direction is pointing into the plane). Temperature and density gradients, ∇T_e and ∇n_e, (and pressure gradient) are in the x direction (here, T_e and pressure decrease toward the positive x direction, while n_e gradient can be in either positive or negative x-direction). The equilibrium uniform magnetic field, B, is in the z-direction. The contours of the total electron pressure (the equilibrium pressure plus perturbed pressure, i.e., $P_{e0} + P_{e1}$) are shown as wide dashed lines. P_{e1} is due to the perturbed E×B drift in the x-direction as described by Eq. 4. Due to a small $k_{||}$ component, perturbed pressure gradients would be established along the equilibrium magnetic field lines, resulting in the corresponding perturbed pressure term in the parallel electron momentum equation that accelerates electrons. The − and + signs denote the relative change in the local electron pressure with respect to the equilibrium. Right: the view in the y–z-plane (the x-direction is pointing out of the plane). The dashed lines denote contours of $P_{e0} + P_{e1}$ and they also denote the constant phase lines of the plane wave perturbation in the y–z-plane

of $f(y,z,t) = f(k_y, k_z, \omega)\exp(j(k_y y + k_z z) - j\omega t)$ where j denotes the imaginary part. We start with the linearized electron continuity equation

$$\frac{\partial n_{e1}}{\partial t} + n_{e0}\nabla \cdot \vec{v}_{e1} + \nabla n_{e0} \cdot \vec{v}_{e1} = \frac{\partial n_{e1}}{\partial t} + n_{e0}\frac{\partial v_{e1z}}{\partial z} + v_{e1x}\frac{dn_{e0}}{dx} = 0, \tag{1}$$

where subscripts of “1” and “0” denote perturbation and equilibrium quantities, respectively. We also note that for φ and components of $\vec{E}$, we do not use subscripts of “1” or “0”, since the corresponding equilibrium quantity is either zero or does not enter the equations. Note that in deriving this, we use the fact that the divergence of the E×B drift velocity and the divergence of diamagnetic particle flux in a uniform magnetic field is zero, and thus, only parallel compression and the convection of equilibrium density are left in Eq. 1 (see Fig. 1 for an illustration). To determine the perturbed electron velocity, we need to use the perpendicular and parallel momentum equations of electrons

$$v_{e1x} = E_y / B_0, \tag{2}$$

$$m_e n_{e0}\frac{\partial v_{e1z}}{\partial t} = -e n_{e0} E_z - \frac{\partial P_{e1}}{\partial z}, \tag{3}$$

where E_y and E_z denote the perturbed electric field in the y-direction and z-direction, respectively, and P_{e1} is the perturbed electron scalar pressure. We note that since the divergence of diamagnetic particle flux in a uniform magnetic field is zero (meaning that the perturbed electron diamagnetic drift velocity is not needed in evaluating Eq. 1), we only keep the E×B drift (a first-order term) in the electron perpendicular momentum equation, Eq. 2, and the electron inertia term is also ignored. For both momentum equations, we ignore the stress tensor term, assuming the diamagnetic flow is small compared to the E×B drift. Next, we need to determine p_{e1} which can be obtained from the electron energy balance equation (see Fig. 1 for an illustration of how parallel pressure gradient is generated)

$$\frac{\partial P_{e1}}{\partial t} + \nabla P_{e0} \cdot \vec{v}_{e1} = 0, \tag{4}$$

where we ignore all perpendicular compressional terms in alignment with the continuity equation, and in addition, we ignore the parallel compressional term in Eq. 4 due to the fact that its contribution is small because of the assumption of cold electrons, i.e., $|\omega / k_z| >> v_{the}$. Using the plane waveform for perturbations, we can use $\partial / \partial t = -j\omega$ and $\nabla = j\vec{k}$ for all the equations above. We first substitute Eq. 2 into Eq. 4 using $\vec{E} = -j\vec{k}\varphi$ to express perturbed electron pressure as a function of φ. We then substitute the resulting expression of perturbed electron pressure into Eq. 3 and again express E_Z in terms of φ to obtain an expression of v_{e1z} as a function of φ

$$v_{e1z} = -\frac{k_z e}{m_e \omega}\left(1 + \frac{\omega_{ep}^*}{\omega}\right)\varphi, \tag{5}$$

where e is the electron charge and $\omega^*_{ep} = -(1+\eta_e)k_yT_{e0}/(eB_0L_{n_e})$. Thus, the perturbed electron density could be obtained by substituting Eqs. 5 and 2 into Eq.1

$$\frac{n_{e1}}{n_{e0}} = -\frac{k_y}{n_{e0}\omega B_0}\frac{dn_{e0}}{dx}\varphi - \frac{k_z^2 e}{m_e\omega^2}\left(1+\frac{\omega^*_{ep}}{\omega}\right)\varphi. \tag{6}$$

Now, we resort to the quasi-neutrality condition between electrons and ions to obtain an expression for φ. The ion density response is assumed to be adiabatic, namely $n_{i1}/n_{i0} = -e\varphi/T_{i0}$, which is justifiable when we assume $k_y\rho_i >> 1$ (here, we assume that Z=1 for the ion species). This assumption effectively means that ions are moving in straight lines on the spatial scale of the waves, and they are essentially unmagnetized. The assumption of adiabatic ions also requires that $|\omega/k_y| << v_{thi}$ (v_{thi} is the ion thermal velocity), which is justifiable with $|\omega| << \omega_{ic}$ (ω_{ic} is the ion gyro-frequency), a condition well satisfied by drift waves in fusion plasmas, e.g., the ITG mode, TEM, and the ETG mode. The adiabatic ion response physically means that in the ion momentum equation, the electrostatic electric field is balanced by the ion pressure perturbation and the ion inertia term is negligible. For simplicity, we assume $T_{e0} = T_{i0}$, and since we also assume that there is only one ion species with Z=1, we can simply use $n_{e0} = n_{i0}$ from the quasi-neutrality condition. Using $n_{e1}/n_{e0} = n_{i1}/n_{i0}$, we obtain the following dispersion relation:

$$1 - \frac{\omega^*_{\rm in}}{\omega} - \frac{k_z^2T_{i0}}{m_e\omega^2} - \frac{k_z^2T_{i0}\omega^*_{ep}}{m_e\omega^3} = 0, \tag{7}$$

where $\omega^*_{\rm in} = -k_yT_{i0}/(eB_0L_{n_e})$ which is the electron diamagnetic drift frequency with ion temperature. Note that $\omega^*_{ep}/\omega^*_{\rm in} = (T_{e0}/T_{i0})(1+\eta_e) = 1+\eta_e$ with $\eta_e = {\rm dln}T_{e0}/{\rm dln}n_{e0}$ (we use $T_{e0} = T_{i0}$ here). Examining the derivation of the dispersion relation, we can identify that the first term on the left-hand side (LHS) is due to the ion adiabatic response, the second term on the LHS is due to the E×B drift convection of the equilibrium density, the third term on the LHS is a part of the parallel compression in Eq. 1 due to the acceleration of electrons by the electrostatic electric field, and the fourth term on the LHS is from the parallel acceleration of electrons due to the perturbed parallel pressure gradient induced by the E×B drift convection of the equilibrium pressure. Now, we can further simplify Eq. 7 using the assumption of $|\omega/k_z| >> v_{\rm the}$ and $T_{e0} = T_{i0}$, which results in neglecting the $k_z^2T_{i0}/m_e\omega^2$ term with respect to 1. Physically, this means that with $|\omega/k_z| >> v_{\rm the}$ and $T_{e0} = T_{i0}$, the electron inertia term in the electron parallel momentum equation cannot be balanced by the electrostatic electric field generated by the ion adiabatic response, because ions are as cold as electrons ($T_{e0} = T_{i0}$). We note that this also means that the electron sound wave would be ordered out by $\omega/k_z >> v_{\rm the}$ and $T_{e0} = T_{i0}$. Recall that the electron sound wave is due to the balance of the electron inertia and the ion pressure perturbation. On the other hand, with $\omega/k_z >> v_{\rm the}$ and $T_{i0} >> T_{e0}$ (hot ions and cold electrons), the electron sound wave can exist in a homogeneous plasma, i.e., $\omega^*_{ep} = \omega^*_{\rm in}$. With the simplifications above, we have

$$1-\frac{\omega^*_{\mathrm{in}}}{\omega}-\frac{k_z^2T_{i0}\omega^*_{ep}}{m_e\omega^3}=0. \tag{8}$$

Noticing that there are three terms on the LHS of Eq. 8, the last of which has a small coefficient, namely $|k_z^2T_{i0}/m_e\omega^2| << 1$, we can find three solutions for Eq. 8 by examining the relative magnitude of these three terms:

(1) If $|\frac{k_z^2T_{i0}\omega^*_{ep}}{m_e\omega^3}| << |\frac{\omega^*_{\mathrm{in}}}{\omega}|$, the first two terms on the LHS could balance each other with a solution as $\omega=\omega^*_{\mathrm{in}}$. We note that one situation that would lead to this solution is the absence of T_e gradient, i.e., $\eta_e=0$. In this context, $\frac{k_z^2T_{i0}\omega^*_{ep}}{m_e\omega^3}=\frac{k_z^2T_{e0}\omega^*_{\mathrm{in}}}{m_e\omega^3}=\frac{k_z^2T_{e0}}{m_e\omega^2}\frac{\omega^*_{\mathrm{in}}}{\omega}$. It is obvious that $|\frac{k_z^2T_{i0}\omega^*_{ep}}{m_e\omega^3}| << |\frac{\omega^*_{\mathrm{in}}}{\omega}|$ is satisfied, since we assume $|\omega/k_z| >> v_{\mathrm{the}}$, i.e., $\frac{k_z^2T_{e0}}{m_e\omega^2} << 1$. Clearly, $\omega=\omega^*_{\mathrm{in}}$ is just the usual drift wave propagating in the y-direction at electron diamagnetic drift velocity. Note that with the solution of $\omega=\omega^*_{\mathrm{in}}$, $k_z^2T_{i0}/m_e\omega^2 << 1$ and $|\frac{k_z^2T_{i0}\omega^*_{ep}}{m_e\omega^3}| << 1$ have to be satisfied, where the former means that $k_z/k_y << \rho_e/|L_{ne}|$ and the latter means that $|(1+\eta_e)|(k_z/k_y)^2/(|L_{ne}|/\rho_e)^2 << 1\,(T_{e0}=T_{i0})$ is used here). Thus, $k_z/k_y << \rho_e/|L_{ne}|$ requires that $|(1+\eta_e)|$ cannot be too large. Physically, this solution is due to the balance between the electron density perturbation due to the E×B drift convection of the equilibrium density and the ion adiabatic response. No parallel physics is involved, which is evident in the independence of k_z in the solution.

(2) The second solution is obtained if the last two terms on the LHS of Eq. 8 are much larger than 1. We can call this solution the low-frequency limit, where $\omega^*_{\mathrm{in}}/\omega >> 1$. Note that the first solution has $\omega=\omega^*_{\mathrm{in}}$. Balancing the two terms, we obtain $\omega^3=-\omega(k_z^2T_{e0}/m_e)(1+\eta_e)$. Since $|\omega/k_z| >> v_{\mathrm{the}}$ applies, $\omega\neq 0$, and thus we reduce the above expression to $\omega^2=-(k_z^2T_{e0}/m_e)(1+\eta_e)$. Obviously, this solution has an unstable and purely growing branch if $1+\eta_e>0$. Note that another stable oscillating solution exists if $1+\eta_e<0$ (e.g., when $L_{n_e}<0$), although we focus on the unstable solution here. Since our assumption, $k_z^2T_{i0}/m_e\omega^2 << 1$, applies, $\eta_e >> 1$ has to be satisfied in order for the solution to be valid. Note that by neglecting 1 in Eq. 8, we assume that the ion adiabatic response is not important, and the quasi-neutrality condition is satisfied solely due to electron dynamics. In this context, the density perturbation is not important for this mode. In the electron continuity equation, density perturbation due to the E×B drift convection of the equilibrium density is balanced by the parallel compression of electrons, and thus, there is no first-order electron density perturbation.

(3) The third solution of the equation can be obtained by balancing the first term and the third term on the LHS of Eq. 8, which leads to $\omega^3=(k_z^2T_{e0}/m_e)(1+\eta_e)\omega^*_{\mathrm{in}}$ (note that we use $\omega^*_{ep}=(T_{e0}/T_{i0})(1+\eta_e)\omega^*_{\mathrm{in}}$ here). We call this solution the high-frequency limit, where $\omega^*_{\mathrm{in}}/\omega << 1$, in contrast to the two solutions above. One of the three roots is an unstable propagating wave driven by ETG regardless of the sign of η_e. This unstable mode is driven by ETG and propagates in the electron diamagnetic drift direction and is the typical electrostatic slab ETG mode we will refer to in the rest of the paper. Note that this is different from the second solution

where with negative η_e, there is no unstable solution. Again, certain conditions have to be satisfied for the solution to be valid. Note that $k_z^2 T_{i0}/m_e \omega^2 << 1$, meaning $|(1+\eta_e)\omega^*_{\mathrm{in}}/\omega| >> 1$, and at the same time, $|\omega^*_{\mathrm{in}}/\omega| << 1$, which implies $|\eta_e| >> 1$. Note that this requirement of $|\eta_e| >> 1$ is similar to that of the fluid ITG mode on $\eta_i >> 1$ in Ref. (Coppi 1967). Thus, the fluid solution here for the slab ETG mode requires $|\eta| >> 1$, not an exact threshold, and it is also clear that the cold electron fluid assumption, i.e., $|\omega/k_z| >> v_{\mathrm{the}}$, requires $|\eta_e| >> 1$. Thus, to obtain an η_e threshold for the slab ETG mode, one has to go beyond the fluid limit. Indeed, a kinetic analysis of the shearless slab ITG mode (applicable to the shearless slab ETG mode due to the isomorphism between electrons and ions in linear physics) shows that the linear threshold of $\eta_e > 0$, η_{ec}, for the shearless slab ETG mode, is $\eta_{ec} = 2(1 - k_\perp^2 \rho_e^2)/(1 + k_\perp^2 \rho_e^2)$ (Hahm and Tang 1989), and if finite Larmor radius (FLR) effect is small, i.e., $k_\perp^2 \rho_e^2 \rightarrow 0$, the expression is further simplified as $\eta_{ec} = 2$. We note that a later analysis based on a fluid model for the toroidal ETG mode gives a stability threshold of $\eta_{e,c} = \frac{2}{3}$ (Horton 1988) (see the next section for more discussions; recall that we only discussed the slab ETG here). We note that whether to include the compressional terms from magnetic drifts (both magnetic gradient and curvature drifts) in the continuity and energy balance equations in the fluid model marks the difference between the slab and toroidal ETG modes. The slab ETG mode only includes the parallel compression due to the parallel electron motion, while the toroidal ETG mode has to include the perpendicular compressional terms due to perpendicular magnetic drifts. The difference in these compressional terms actually leads to different saturation mechanisms of ETG turbulence (Jenko and Dorland 2002), which we will discuss in Sect. 2.2. Furthermore, we note that by neglecting the second term on the LHS of Eq. 8, we assume that the density perturbation induced by the E×B drift convection of equilibrium density is not important. The quasi-neutrality condition is satisfied by balancing the electron density perturbation due to parallel compression with the ion adiabatic response.

We would like to further explore the mechanism behind this shearless slab ETG mode solution by noticing the balancing of the first and last terms in Eq. 8. As we have pointed out above, the first term comes from the quasi-neutrality condition with ions and the last term comes from parallel density compression due to the parallel electron velocity driven by the perturbed parallel pressure gradient generated by the E×B drift convection of the equilibrium pressure. This means that it is the coupling between the equilibrium electron pressure gradient and parallel electron motion through the E×B drift that leads to instability. In other words, the parallel motion compresses electrons and leads to an electron density increase which adiabatic ions would respond to neutralize and establish an electric field. This electric field would generate an E×B drift dragging cold electrons in (with a proper relative phase) and further increase the parallel pressure gradient, leading to more compression of electrons. This kind of feedback loop leads to the growth of the slab ETG mode. A more detailed physics picture of the slab ITG mode with all the phase relations between different quantities taken into account can be found in Ref. (Cowley 1991), which is perfectly applicable to the simple model of the slab ETG presented here. Of course, this overly simplified model only demonstrates the existence of the ETG mode in a local slab geometry, and further linear analyses have explored more complete models including magnetic shear effects (e.g., using a sheared slab geometry) (Kadomitsev and Pogutse 1970; Lee 1987; Idomura 2000a; Guang-De and Jia-Qi 2004; Idomura 2005, radial localization in x (~ radial) in the slab geometry/radial mode structure (Kadomitsev and Pogutse 1970; Lee 1987), electromagnetic effects (e.g., considering parallel vector potential in finite β plasmas) (Rozhanskii 1981; Lee 1987; Kim and Horton 1991; Feng 2005; Maeyama 2021), the toroidal geometry (e.g., including magnetic drifts due to the inhomogeneous magnetic field of toroidal geometry and associated compressional terms in the continuity and energy balance equations in fluid model) (Horton 1988; Shukla and Weiland 1989; Hirose 1990; Dong 2002), a more complete pressure equation with heat flux (Horton 1988; Shukla and Weiland 1989), and kinetic damping due to magnetic drift and electron parallel transit motion (Hirose 1990; Kim and Horton 1991).

Since the toroidal ETG mode may be of more importance than the slab ETG mode to electron thermal transport in toroidal confinement devices, it is beneficial to present a simple physics picture of this mode to illustrate the underlying basic physics process. Here, we present an intuitive picture of the toroidal ETG mode, following a physics picture of the toroidal ITG mode in M.A. Beer's Ph.D. thesis (Beer 1995) (as we have pointed out that the ETG mode mirrors the ITG mode with the roles of electrons and ions switched). The instability is due to the interaction between the radial electron temperature gradient and electron toroidal magnetic

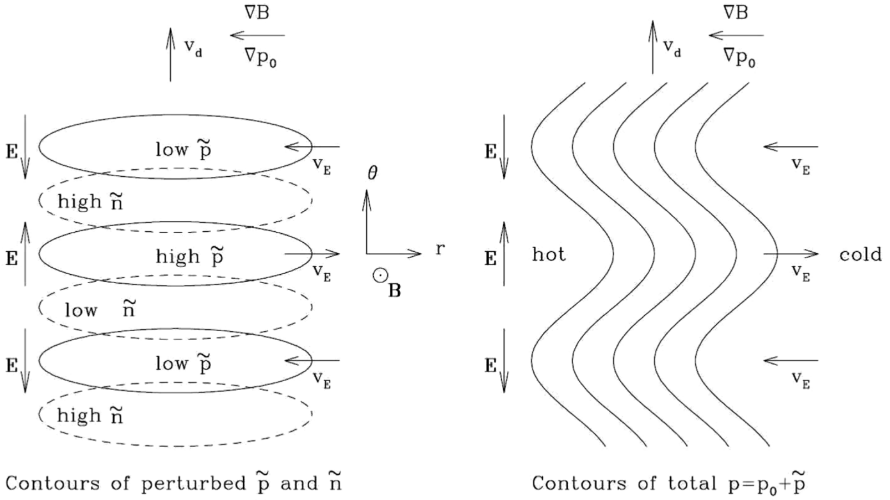

Contours of perturbed $\tilde{p}$ and $\tilde{n}$ Contours of total $p=p_0+\tilde{p}$

Fig. 2 A schematic of feedback loop for the toroidal ETG mode. (Left) electron density perturbation (dashed line contours) generated by an initial electron pressure perturbation (due to temperature perturbation) (solid line contours); (right) contours of total electron pressure. The directions of E, V_d, and V_E are denoted by arrows at their respective location. The directions of the equilibrium ∇B and ∇P_0 are also shown by arrows. The figure is adapted from Fig. 1.1 in Ref. (Beer 1995), with permission of the author gradient and curvature drifts, $\vec{V}_d = \frac{v_{||}^2 + v_\perp^2/2}{\Omega B^2}\vec{B} \times \nabla B$ (where $v_{||}$ is the parallel electron velocity, $v_\perp$ is the perpendicular electron velocity, $\vec{B}$ is the vector of magnetic field, and Ω is the electron gyro-frequency). As seen in Fig. 2, with the background magnetic field in the out-of-plane direction and both the magnetic gradient and equilibrium pressure gradient in the same direction (i.e., pointing inward at the outer mid-plane of a tokamak, and note that the radial direction is horizontal), electrons are drifting upwards (see the upward pointing arrows for V_d). With an initial electron temperature perturbation and assuming a flat density profile, contours of the total electron pressure $P = P_0 + \tilde{P}$ (where P_0 is the equilibrium electron pressure and $\tilde{P}$ is the electron pressure perturbation due to the electron temperature perturbation) are shown in the right panel of Fig. 2. Note that the contours of equilibrium pressure would be vertical straight lines (not shown). Contours of $\tilde{P}$ shown in the left panel of Fig. 2 (solid line) have hot spots (high $\tilde{P}$) and cold spots (low $\tilde{P}$) next to each other. Because $\vec{V}_d$ is temperature dependent, namely hotter electrons drifting faster and colder electrons drifting slower, this leads to the accumulation of electrons below the cold spots and above the hot spots and the depletion of electrons below the hot spots and above the cold spots (see the dashed line contours in the left panel). With assumptions of adiabatic ions (applicable for the ETG mode) and quasi-neutrality condition, the high-density spots (high $\tilde{n}$) correspond to low electrostatic potential spots, and the low-density spots (low $\tilde{n}$) correspond to high electrostatic potential spots, and a poloidal (θ direction) electric field with directions denoted by arrows in Fig. 2 would be generated between the high- and low-density spots. The poloidal electric field and the toroidal magnetic field generate a radial E×B drift, V_E, in the direction denoted by arrows in Fig. 2. It is obvious that the generated V_E moves hotter plasmas into the hot spots and colder plasmas into the cold spots (see the right panel in Fig. 2), enhancing the initial perturbation and forming a feedback loop in order for the ETG mode to grow in amplitude. We note that this instability critically depends on the relative direction of ∇B and ∇P_0. When they are in the same direction as in the outer mid-plane, as described above, the ETG mode is unstable. With them in different directions as in the inner mid-plane (now hotter plasma would be on the right with the same gradient B direction versus hotter plasma on the left as shown in Fig. 2), the generated E×B drift would move colder plasmas into the hot spots and hotter plasmas into the cold spots, suppressing the initial perturbation and the ETG mode would be stable.

Here, we would like to provide further comments on the assumption of adiabatic ions (electrons) in ETG (ITG) mode. To illustrate the essential unstable mechanism of the ETG mode, we fully utilized the simplicity of applying adiabatic ion response in the analysis as adiabatic electron response is often used for the linear ITG mode (note the isomorphy between ETG and ITG modes with just roles of electron and ions switched), which makes the analysis more tractable and more understandable. This, however, does not imply that the adiabatic assumption should be taken for granted in assessing the nonlinearity of ETG and ITG modes. The adiabatic assumption leads to zero electron particle flux in ITG turbulence and zero ion particle flux in ETG turbulence, since there is zero phase shift between density fluctuations and electrostatic potential fluctuations for the adiabatic species. As we have discussed in Sect. 1, analyses of the relationship between transport fluxes and thermodynamic forces show that the total turbulence-driven particle flux must be intrinsically ambipolar in axisymmetric systems (Shaing 1988; Sugama 1996), and as a result, the total particle flux has to be zero. Given the importance of ITG turbulence in driving particle and thermal transports in magnetic confinement devices, using the assumption of adiabatic electrons for the ITG mode is not a good choice and should generally be limited to illustrating its linear physics. On the other hand, since ETG turbulence mainly drives electron thermal transport, using the assumption of adiabatic ions for the ETG mode is a better choice. However, as we will discuss in Sect. 2.2.4, using the adiabatic ions in nonlinear gyrokinetic ETG simulation could lead to saturation problems. Even for the ETG mode, adiabatic ions may not be a good assumption in the H-mode pedestal region as will be discussed in Sect. 4.

2.1.2 Linear stability threshold of the ETG mode

From the analysis in Sect. 2.1.1, we can see the driving parameter for the ETG mode is η_e, i.e., the ratio between normalized T_e gradient and n_e gradient (both for the slab and toroidal ETG mode). Thus, it is reasonable to expect that there would be a threshold in η_e beyond which the slab/toroidal ETG mode would become linearly unstable. The derivation in Sect. 2.1.1 only shows that in order for the slab ETG mode solution in the fluid limit to be valid, $\eta_e >> 1$ has to be satisfied, namely either large normalized T_e gradient or small normalized n_e gradient. This, of course, is not quantitative enough to provide guidance to experiments. Horton (1988) derived a dispersion relation for the toroidal ETG mode with a kinetic ion response using a set of fluid equations. The fluid equations incorporate more realistic effects that are not captured by the simple model derived in the last section. The toroidal geometry employed in the model leads to compressional terms due to E×B drift, diamagnetic drift, and polarization drift in the continuity equation, and it also leads to the inclusion of compressional terms due to E×B drift and diamagnetic drift in the electron energy equation where the collisionless FLR heat flux (Braginskii 1965) is also included. The inclusion of these terms is apparently important for establishing the linear threshold for the ETG mode. Using a local approximation, it was shown that the critical $\eta_e \simeq \frac{2}{3}$, while for small density gradient (e.g., in the core of an H-mode plasma), the unstable range of the normalized ETG is

$$-x_1 - \sqrt{x_1^2 - x_2} < \frac{R}{L_{T_e}} < -x_1 + \sqrt{x_1^2 - x_2}, \tag{9}$$

where R is the major radius of a flux surface in a circular tokamak. x_1 and x_2 are defined as follows:

$$x_1 =(4/k^4\tau)(1 + k^2 d_e)(1 + \Gamma\tau k^2) - (2/k^2\tau)(1 + 2\Gamma\tau + \Gamma\tau k^2), \tag{10}$$

$$x_2 =(4/k^4\tau)(1 + 2\Gamma\tau + \Gamma\tau k^2)^2 - [16\Gamma(1 + \tau)/k^4\tau](1 + k^2 d_e), \tag{11}$$

where k the normalized wavenumber (to ρ_{ei}, electron gyroraduis with ion temperature), $\Gamma = 5/3$ (coefficient in the adiabatic equation of state), $\tau = T_e/T_i$, ω_{ce} is the electron gyro-frequency, and $d_e = 1 + \omega_{ce}^2/\omega_{pe}^2$. We can see that if $x_1^2 - x_2 < 0$, there is no unstable solution. Using the expressions of x_1 and x_2 in Eqs. 10 and 11, we can reduce $x_1^2 - x_2$ to the following form:

$$x_1^2 - x_2 = \frac{16}{k^8\tau}\left[1 + k^2(1 + \frac{\omega_{ce}^2}{\omega_{pe}^2})\right]\left[(1 + k^2\Gamma\tau)^2\left(k^2\frac{\omega_{ce}^2}{\omega_{pe}^2} - 1\right) + 2 - k^4\Gamma\tau(1+\tau)\right]. \tag{12}$$

Examining Eq. 12, we can see that the sign of $x_1^2 - x_2$ is determined by the right-most term in the square brackets on the right-hand side (RHS) of Eq. 12 since the other two terms are always positive. Since k, τ, and Γ are of the order of unity, the sign of this right-most term is determined by $\omega_{ce}^2/\omega_{pe}^2$. If $\omega_{ce}^2/\omega_{pe}^2$ is a few times of one as easily achievable in the conventional tokamaks (e.g., a toroidal field of 3 T and density of 2×10^{13} cm^{-3} leading to $\omega_{ce}^2/\omega_{pe}^2 \approx 4.4$), this right-most term would be positive, meaning that there is an unstable-ETG-mode regime for R/L_{T_e}. If $\omega_{ce}^2/\omega_{pe}^2 << 1$, this right-most term can be negative (thus for $x_1^2 - x_2 < 0$ to be negative), where no unstable ETG solution could be found, and $\omega_{ce}^2/\omega_{pe}^2 << 1$ can easily be achieved in low-field STs (e.g., NSTX with a toroidal field of 0.5 T and density of 2×10^{13} cm^{-3} to get $\omega_{ce}^2/\omega_{pe}^2 \approx 0.12$). The stability boundary in the L_n and L_{T_e} parametric space is shown in Fig. 3, where a clear threshold of 2/3 in η_e

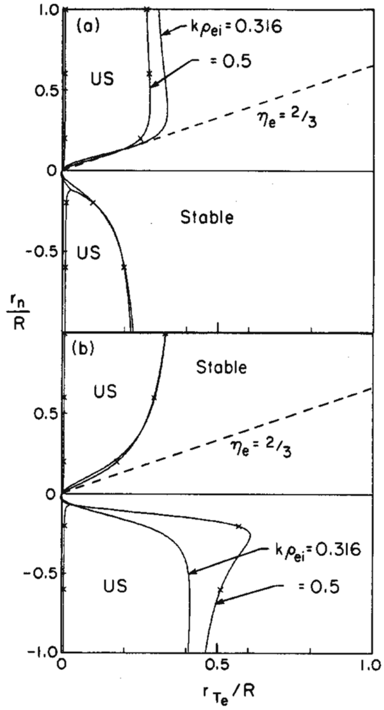

Fig. 3 ETG stability boundary in the r_n/R and r_{T_e}/R parametric space ('US' for unstable) for two wavenumbers from the dispersion relation neglecting the FLR electron heat flux (**a**) and including the FLR heat flux (**b**). Note that a smaller r_n/R or r_{T_e}/R means a larger gradient and vice versa. To be consistent throughout the paper for the denotation of gradient scale length, we use L to denote gradient scale length in the discussion of the figure instead of r as used in the figure. The figure is from Fig. 1 in Horton (1988). Reprinted from Horton (1988), with the permission of AIP Publishing

(without the FLR heat flux in the electron energy balance equation) can be clearly seen in Fig. 3 in the small L_n/R and L_{T_e}/R region (a) and the threshold changes to about 1 as shown in (b) with the FLR heat flux in the electron energy balance equation. Here, we would like to emphasize that since L_n/R and L_{T_e}/R are used in Fig. 3 to denote gradients, a smaller L_n/R or L_{T_e}/R means a larger gradient and vice versa. Another notable thing is that at larger L_n/R (smaller density gradient), the stability curve becomes almost vertical, meaning that the threshold is almost purely in L_{T_e}/R and the threshold has a very weak dependence on L_n/R. Furthermore, the condition $\eta_e > 2/3$ or 1 is important, since any space in Fig. 3 with $\eta_e < 2/3$ or 1 is a stable region, which means that $\eta_e > 2/3$ or 1 is a necessary but not sufficient condition for the ETG mode to be unstable.

Having shown the threshold in η_e for the ETG mode and the insensitivity of the T_e gradient threshold to the density gradient when the density gradient is sufficiently small, we would like to discuss the parametric dependence of the threshold in T_e gradient, since T_e gradient is the driving force for the ETG mode and the threshold in T_e gradient is more meaningful with a small density gradient. One thing that can be immediately expected from the discussion above is that the threshold in T_e gradient is a function of the density gradient only when the density gradient is large enough, and it would make a transition to be almost independent of the density gradient as the density gradient is lowered. Equation 9 provides a parametric dependence of ETG threshold on a limited number of parameters in the low-density gradient regime for a circular tokamak equilibrium and you might expect the results in Horton (1988) have reached the limit of analytical theory. Jenko (2001) have carried out an extensive amount of linear stability analysis using a linear initial value gyrokinetic code, GS2 (Kotschenreuther 1995) (with full kinetic particle species, electromagnetic effects, and a Lorentz collision operator), to numerically map out the parametric dependence of the threshold of R/L_{T_e} for the ETG mode based on a large aspect ratio circular flux-surface MHD equilibrium (Connor 1978) and fit it to an analytical form. Note that as an initial value code, the GS2 code finds the most unstable mode for a particular set of equilibrium parameters and a given perpendicular wavenumber. The analytical formula has also been corrected with finite aspect ratio and elongation (triangularity was found to have little effect on the linear threshold), which makes it more relevant to current tokamak experiments. Thus, the resulting formula is very useful for quickly assessing the stability of the ETG mode during experiments. The obtained parametric dependence of the critical ETG threshold is as follows:

$$(R_0/L_{T_e})_{crit} = \max\left\{ \left(1 + Z_{eff}\frac{T_e}{T_i}\right)(1.33 + 1.99\hat{s}/q)(1 - 1.5\epsilon)\left(1 + 0.3\epsilon\frac{d\kappa}{d\epsilon}\right), 0.8R_0/L_{n_e} \right\}, \tag{13}$$

where R_0/L_{T_e} is the T_e gradient normalized by the major radius of the flux-surface center of a tokamak (R_0), Z_{eff} is the effective ionic charge, $\hat{s}$ is the magnetic shear, q is the safety factor, ϵ is the inverse aspect ratio, and κ is the plasma flux-surface elongation. The expression, $(1 + Z_{eff}T_e/T_i)(1.33 + 1.99\hat{s}/q)$, comes from a linear combination of two formulas obtained analytically in two limiting cases in Romanelli (1989); Hahm and Tang (1989), where Hahm and Tang

(1989) has $(R_0/L_{T_e})_{\mathrm{crit}} = 1.88(1 + Z_{\mathrm{eff}}T_e/T_i)\hat{s}/q$ without considering perpendicular compression (the sheared slab ETG mode) and Romanelli (1989) has $(R_0/L_{T_e})_{\mathrm{crit}} = 4/3(1 + Z_{\mathrm{eff}}T_e/T_i)$ without considering parallel compression (note that this result of Romanelli's was obtained for the toroidal ITG mode in the limit of interchange instability with negligible parallel dynamics and is applied to the ETG mode due to the isomorphism between ETG and ITG modes; also note that the result of Hahm and Tang (1989) was also obtained for the ITG mode in the sheared slab limit and is applied to the ETG mode due to the same reason). By examining Eq. 13, we can immediately draw some interesting conclusions about the ETG mode. One obvious observation is that the critical threshold is the maximum of two individual terms, one of which is a function of density gradient alone. This means that if the density gradient is large enough, the density gradient term can solely determine the critical threshold linear ETG stability, implying that properly controlled density profiles in fusion devices could linearly stabilize the ETG mode and can be used as an experimental knob to control ETG turbulence. This observation has been validated in experiments (Ren 2011, 2012), which will be reviewed in detail in Sect. 4. We note that this dependence on the density gradient (no dependence on the density) agrees with the behavior of the stability boundary shown in Fig. 3. The critical η_e from Eq. 13 is 0.8, which is fairly close to values of 2/3 (without the FLR heat flux) and 1 (with the heat flux or from a local kinetic dispersion relation) shown in Horton (1988). The independence on the density gradient seen in Fig. 3 with small density gradient is consistent with the second term in the max function overtaking the density gradient term and determining $(R_0/L_{T_e})_{\mathrm{crit}}$. Further examination of Eq. 13 shows that $(R_0/L_{T_e})_{\mathrm{crit}}$ is positively correlated with Z_{eff}, T_e/T_i and $\hat{s}/q$, meaning that increasing these parameters would increase the linear threshold and lead to the stabilization of the ETG mode. It is important to point out that there are restrictions to applying Eq. 13, namely $0 \leqslant \tau = T_e/T_i \leqslant 5$, $0.2 \leqslant \hat{s} \leqslant 3$, $0.5 \leqslant q$, $0 \lesssim \hat{s}/q \lesssim 2$, $\alpha < 0.1$ (the normalized pressure gradient in the $s - \alpha$ model (Connor 1978)) and $0 \lesssim \epsilon \lesssim 0.3$. However, R_0/L_{n_e} is arbitrary. It is pointed out that Eq. 13 works best near its nominal values: $\tau = 1$, $\hat{s} = 0.8$, $q = 1.4$, and $\alpha = 0$ (Jenko 2001).

Other authors have also carried out similar studies of the T_e gradient threshold of the ETG mode. Notably, Dong (2002, 2003) derived a set of coupled integral dispersion equations for low β plasmas with electromagnetic effects (i.e., with perturbed parallel vector potential) in a toroidal geometry with circular magnetic flux surfaces using ballooning representation (Connor 1979), which is solved to obtain eigenvalues in ω and corresponding eigenfunctions for both unstable and stable modes to obtain the critical T_e gradient. The results were fitted to analytical forms. It was found that close to the linear stability threshold, the maximum linear growth rate (with respect to poloidal wavenumber k_θ), $\gamma_{\max}$, is an offset linear function of η_e

$$\gamma_{\max} = \sigma\omega_e^*(\eta_e - \eta_e^c), \tag{14}$$

where σ is a proportional factor and η_e^c is the critical threshold of η_e, both of which are functions of other dimensionless parameters, i.e., $\hat{s}$, q, $\epsilon_n = L_n/R$ (toroidicity) and τ. Note that $R/L_{T_e} = \eta_e/\epsilon_n$, and the critical R/L_{T_e}, $(R/L_{T_e})^c$, can be easily obtained from η_e^c. A large effort was made to study the parametric dependence of σ

Fig. 4 η_e^c (**a**) and $(R/L_{T_e})^c$ (**b**) as a function of ϵ_n. Different symbols denote different τ: $\tau = 3$ (small open circles), $\tau = 2$ (large open circles), $\tau = 1$ (filled circles), and $\tau = 1/3$ (open triangles). The lines are from polynomial fittings with ϵ_n. The figure is reprinted from Fig. 1 in Dong (2003), with the permission of International Atomic Energy Agency

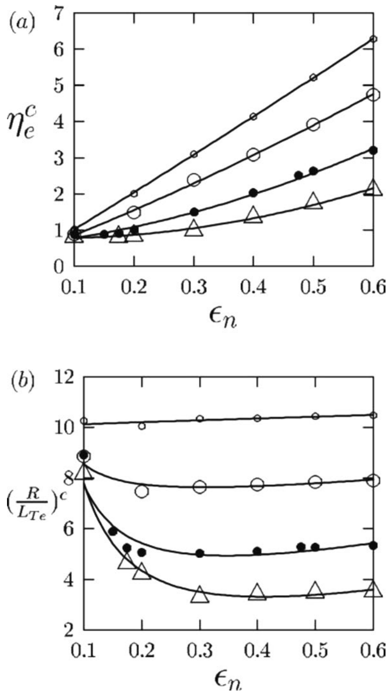

and $(R/L_{T_e})^c$ (Dong 2003), where numerical scans in τ, ϵ_n, $\hat{s}$ and q were carried out. As an example, we show η_e^c and $R/L_{T_e}^c$ as a function of ϵ_n in Fig. 4a and b, respectively, with a nominal value of 1 for $\hat{s}$ and 1.5 for q. The polynomial fitting was carried out to obtain analytical forms for the dependence (see the solid lines in the figure). It is clear that η_e^c is positively correlated with ϵ_n. On the other hand, $(R/L_{T_e})^c = \eta_e^c/\epsilon_n$ is insensitive to the whole range of ϵ_n ($0.1 \leqslant \epsilon_n \leqslant 0.6$) with $\tau = 3$ while it is only sensitive in a lower ϵ_n range with other τ values. This is clearly in agreement with Eq. 13 qualitatively in the sense that $(R/L_{T_e})^c$ should be independent of the density gradient when it is small, and in other words, a large ϵ_n with a large τ would make the second term in the max function in Eq. 13 so large that $(R/L_{T_e})^c$ is independent of ϵ_n over the whole range. As a result, η_e^c and $(R/L_{T_e})^c$ can be fitted as functions of ϵ_n and τ

$$\eta_e^c(\tau, \epsilon_n) = c_1(\tau)\epsilon_n^2 + c_2(\tau)\epsilon_n + c_3(\tau), \tag{15}$$

$$\left(\frac{R}{L_{T_e}}\right)^c(\tau, \epsilon_n) = c_1(\tau)\epsilon_n + c_2(\tau) + c_3(\tau)/\epsilon_n, \tag{16}$$

where c_1, c_2 and c_3 are found to be

$$
\begin{aligned}
c_1 &= \frac{1}{0.0818\tau^3 - 0.121\tau^2 + 0.0489\tau + 0.207} \\
c_2 &= -0.429\tau^3 + 2.148\tau^2 + 1.159\tau - 1.131 \\
c_3 &= 0.0294\tau^3 - 0.101\tau^2 - 0.258\tau + 0.881.
\end{aligned} \tag{17}
$$

The proportional factor σ can be fitted similarly as a function of τ and ϵ_n; see Ref. (Dong 2003) for details. In addition, the authors have applied the same procedures to study the dependence of η_e^c and $(R/L_{T_e})^c$ on ϵ_n and τ for a negative $\hat{s}$ of -1, where it was found that the linear threshold for the same shear magnitude is higher for the negative shear than for the positive shear, provided other parameters kept the same. The same procedure was also applied to the dependence on $\hat{s}$ and q where qualitative agreement with Horton (2000); Jenko (2001) is found.

Many effects would impact the stability of the ETG mode, and some parametric dependence is discussed in this section (particularly in the linear threshold expressions in Eqs. 13 and 15). One particularly important parameter not covered above is plasma β which introduces electromagnetic effects in the ETG mode. Electromagnetic effects introduce magnetic fluctuations in addition to potential fluctuations, and magnetic fluctuations are found to have radial localization on the order of c/ω_{pe} instead of ρ_e, typical for potential fluctuations (Lee 1987; Rozhanskii 1981), which could be an important difference. Although electromagnetic effects are usually ignored in low β plasmas due to the strong magnetic field in magnetic confinement devices, they could be important for intrinsically high β STs and future high β fusion reactors. Linearly, it is shown that electromagnetic effects are stabilizing to the slab ETG mode and destabilizing to the toroidal ETG mode (Kim and Horton 1991). It was found that the main effect of finite β is to reduce the parallel compression. Since the parallel compression drives the slab ETG mode, the reduction of the parallel compression by finite β would lead to the stabilization of the slab ETG mode. On the other hand, since the parallel compression stabilizes the toroidal ETG mode, the reduction of the parallel compression by finite β would lead to the destabilization of the toroidal ETG mode. This theory-predicted destabilizing effect of finite β on the toroidal ETG mode seems to be consistent with the numerical study of the parametric dependence of $(R_0/L_{T_e})_{\mathrm{crit}}$ by Jenko (2001) where finite-β-induced magnetic field fluctuations are found to be slightly destabilizing. However, we note that the $(R_0/L_{T_e})_{crit}$ described by Eq. 13 has no explicit β dependence, since the $(R_0/L_{T_e})_{\mathrm{crit}}$ dependence on β is too weak (Jenko 2001).

2.2 Nonlinear saturation of the ETG mode and electron thermal transport

The most important aspect of the ETG mode is the plasma transport it drives which critically depends on its nonlinear saturation, e.g., saturated amplitude and wavenumber spectrum. It is well known that the electrostatic ETG mode cannot drive electron particle transport, because ions respond adiabatically, leading to zero phase shifts between electrostatic potential and density fluctuations. Thus, almost all calculations of ETG-turbulence-driven plasma transport focused on electron thermal transport, and more recently, current driven by the ETG mode was investigated with gyrokinetic simulations (Yi 2016). There have been numerous studies of the ETG mode nonlinear saturation and the associated electron thermal transport in the literature, including mixing-length and quasi-linear estimates (Rozhanskii 1981; Lee 1987; Horton 1988; Dong 2002, 2003), simulations based on Braginskii's fluid equations/gyro-fluid equations (Horton et al. 1990; Drake 1988; Labit and Ottaviani 2007; Li and Kishimoto 2002) and gyrokinetic equations (Jenko 2000; Idomura 2000a; Dorland 2000; Jenko and Dorland 2002; Lin 2005). For gyrokinetic simulations, there are local flux-tube simulations, which saves computational time by simulating only a fraction of the plasma volume following local magnetic field lines, and global simulations, which take into account of profile variation but require much more computational resources. We note that recently developed gyro-fluid and gyrokinetic equations have vastly improved our understanding of the nonlinear saturation physics of the ETG mode, and they brought the ETG mode to a solid footing as a major candidate for driving anomalous electron thermal transport. In this section, we focus on the nonlinear saturation physics of the ETG mode and the associated electron thermal transport elucidated by gyro-fluid and gyrokinetic simulations.

2.2.1 Relevance of the ETG mode to electron thermal transport

Applying massively parallelized nonlinear gyrokinetic codes to simulate collisionless ETG turbulence has brought breakthroughs in demonstrating the relevance of ETG-turbulence-driven electron thermal transport for high-temperature toroidal fusion devices (Jenko 2000; Dorland 2000; Jenko and Dorland 2002). In short, the simulations with gyrokinetic codes, Gyrokinetic Electromagnetic Numerical Experiment (GENE) code and GS2 (Kotschenreuther 1995), have shown that by forming radially elongated turbulence eddies, as reported in the literature (Drake 1988; Cowley 1991), ETG turbulence can generate electron thermal transport significantly higher than that given by the electron gyro-Bohm value. Employing a large aspect ratio MHD equilibrium with $q = 1.4$, $\hat{s} = 0.8$, $R/L_T = 6.9$, $R/L_n = 2.2$, $T_e = T_i$, $Z_{\text{eff}} = 1$, $\alpha = 0.45$ ($\alpha = -q^2 R\beta'$ is the Shafranov shift parameter and β' is the radial derivative of β), and $r/R = 0.18$, the gyrokinetic Vlasov–Maxwell equations are solved on a fixed grid with a typical simulation domain with a size of $L_x = 175\rho_e$, $1 < L_x/L_y < 4$, and grid size of $\Delta x = \Delta y = 1.8\rho_e$ (parallel grid of 16–32 per 2π). The adiabatic ion response is used in the simulations and trapped electrons are neglected [poor code performance due to violent ETG turbulence at this operating point leads to neglecting trapped electrons, and a slightly different operating point, i.e., with lowered $\hat{s}$, was chosen to avoid this issue as discussed in Sect. 2.2.4 (Nevins 2006)]. The thermal diffusivity is obtained using $\chi = Q/(-n^{(0)}\nabla T^{(0)})$, where $n^{(0)}$ and $T^{(0)}$ are the equilibrium density and temperature (and χ is dimensional here and its normalization is shown below), respectively, and Q is the radial turbulent electron heat flux (in x direction) defined as Jenko (2000)

$$Q = \left\langle\left\langle \frac{m_e}{2} \int \mathrm{d}\vec{v}(v_{Ex} + v_{||}b_x)v^2\tilde{f}_e \right\rangle\right\rangle, \tag{18}$$

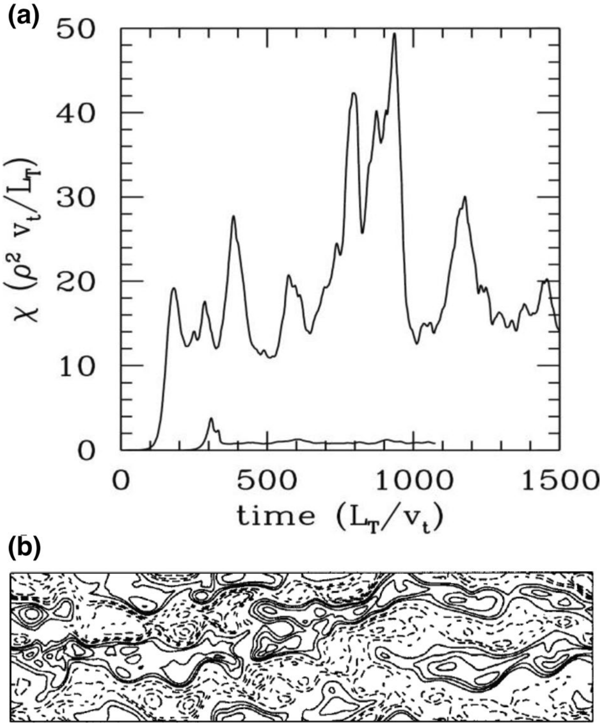

Fig. 5 **a** χ_e^{ETG} (upper curve)and χ_e^{ITG} (lower curve) with the same equilibrium quantities. **b** Perturbed electrostatic potential contours in the outboard *x*–*y*-plane. The snapshot was taken at the end of the ETG simulation shown in (**a**). The size of the domain shown in (**b**) is $256\rho_e \times 64\rho_e$. The simulations use a large aspect ratio MHD equilibrium without trapped electrons. Panel a is adapted from Fig. 1 and panel b is adapted from Fig. 2 in Dorland (2000). Reprinted with permission from Dorland (2000). Copyright (2000) by the American Physical Society

where $\tilde{f}_e$ is the perturbed electron distribution function, v_{Ex} is the E×B convection, $v_{||}b_x$ is the parallel velocity projected to radial (x) direction from the magnetic flutter effect, and the double bracket shows averaging over the whole simulation domain. Note that Q is expressed in the unit of $(nT/L_n)\rho v_t/L_n$ after normalization, and thus, χ is normalized to $\rho v_t/L_n$ (ρ and v_t are quantities for a particular species). It can be clearly seen in Fig. 5a that the electron thermal diffusivity driven by ETG turbulence, χ_e^{ETG}, is much larger than the electron thermal diffusivity driven by ITG turbulence, χ_e^{ITG}, in their respective normalizing unit (gyro-Bohm units for electrons and ions, respectively). Given the large normalized χ_e driven by ETG turbulence, it is almost comparable to χ_e driven by ITG turbulence, overcoming the large difference between thermal diffusivities from ETG and ITG turbulence mentioned in Sect. 1 due to scale separation. The large normalized ETG-driven thermal diffusivity is found to be associated with large amplitude and radially elongated structures, streamers, at the outboard mid-plane during the steady-state phase, which is shown in Fig. 5b. These streamers have radial lengths about $100\rho_e$, which is much larger than the radial extent of the electrostatic potential of about ρ_e from the linear stability analysis of the ETG mode, e.g., see (Lee 1987), which is the primary reason why the electron thermal diffusivity is much larger than the electron gyro-Bohm value. It is pointed out in Dorland (2000) that the formation of ETG turbulence streamers is due to the a-factor-of-($k_\perp \rho_e$) smaller growth rate of its secondary instability, which saturates the primary modes (streamers here), than the conventional Kelvin–Helmholtz (KH) instability. Since ITG turbulence has a secondary instability growth rate higher than that of conventional KH (Rogers 2000), the secondary instability of ETG turbulence is thus much weaker compared with that of ITG turbulence, particularly at smaller wavenumbers, leading to a much higher normalized saturation level of ETG turbulence than that of ITG turbulence. ETG turbulence simulations with ions as a kinetic species with the same equilibrium quantities have demonstrated similar behavior of ETG turbulence as that with adiabatic ions (Jenko 2000). We note that we are discussing the initial saturation mechanisms here, while the subsequent evolution (after this initial saturation phase) and long-time saturation of ETG turbulence could involve ion-scale/electron-scale zonal flows and multiscale interactions (Parker 2006; Colyer 2017; Nakata 2012; Howard 2016; Holland 2017).

Scans in $\hat{s}$ and α (β is varied consistently with α in the scans) with the GENE code have been carried out to assess the dependence of ETG-turbulence-driven thermal transport on these parameters. The qualitative results are shown in Fig. 6. It can be seen that the ETG turbulence-driven electron thermal transport is high for low α and high $\hat{s}$ (($Q \gtrsim 100$)), where ETG streamers are present. The low-transport region ($Q \sim 20$) marked by high α and low $\hat{s}$ is coinciding with the absence of ETG streamers. Note that the transition between low and high transport regions is quite sharp, i.e., a ~10% change in α being sufficient for the transport state to change. It is pointed out that this high α and low $\hat{s}$ regime corresponds to characteristic plasma parameters in ITB's in "advanced" tokamaks (Stallard 1999). Furthermore, these finite $\beta \leqslant 10\%$ simulations show that electrostatic energy transport is dominant, while transport due to the magnetic flutter effect only amounts to a few percent at

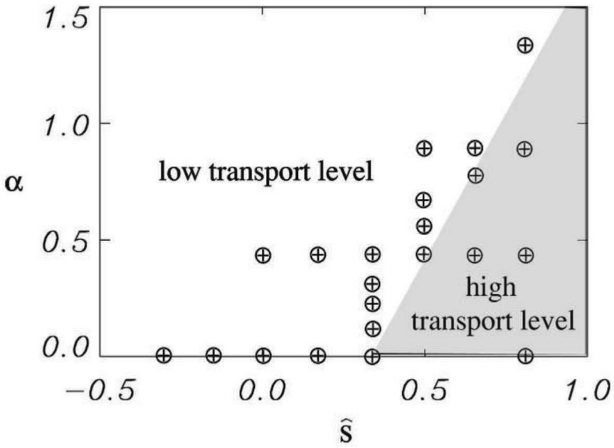

Fig. 6 Nonlinear simulation scans in $\hat{s}$ and α with other parameters fixed at nominal values. The figure is from Fig. 3 in Dorland (2000). Reprinted with permission from Dorland (2000). Copyright (2000) by the American Physical Society

best. Having established the importance of weak secondary instability in allowing ETG turbulence to have higher normalized thermal transport than ITG turbulence, Jenko et al. (2002) identified two different secondary instabilities the properties of which would determine the final saturation level of ETG turbulence. It is found that one instability (so-called Rogers secondary) is driven by the perpendicular shear of the perpendicular E×B flow, while the other so-called Cowley secondary (Cowley 1991) is driven by the perpendicular shear of the parallel flow (note that the dominant perpendicular compressional terms due to magnetic drift are the hallmark of the toroidal ETG mode, while the dominant parallel compressional terms due to parallel flow are the main feature of the slab ETG mode as discussed in Sect. 2.1.1). The former is weakened by adiabatic ion response in the ETG mode (in contrast to the adiabatic electron response in the ITG mode), while the latter is not. Thus, the Rogers secondary in ETG turbulence is much weaker than in ITG due to the difference in the response of adiabatic species. Since only the Rogers secondary plays a role in turbulence saturation of purely curvature-driven toroidal ETG or ITG mode, the much weaker Rogers secondary in the ETG mode allows it to saturate at much higher normalized amplitude and to drive much higher normalized electron thermal transport, while in slab cases, due to the insensitivity of the Cowley secondary to the response of adiabatic species, ETG and ITG turbulence lead to similar normalized saturation levels (see Fig. 7).

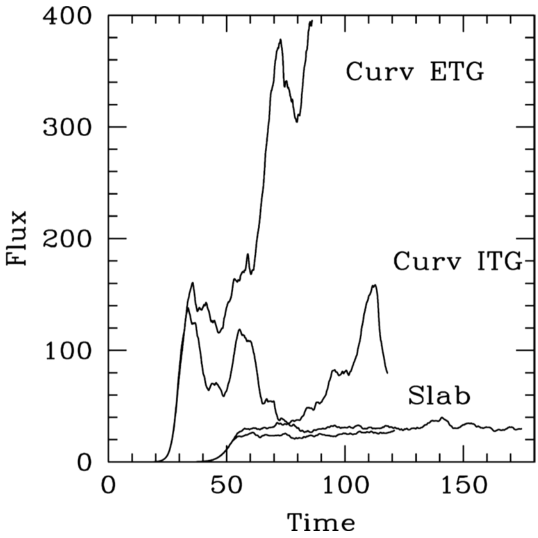

Fig. 7 Comparison of normalized heat flux driven by perpendicular compression-induced instabilities “Curv” and by parallel compression-induced instabilities “Slab”. Note the much larger normalized heat flux driven by “Curv” ETG mode than “Curv” ITG mode and the similar flux level between “Slab” ETG and ITG modes. For t > 90, the flux from the “Curv” ETG mode continues to grow. The simulations use a large aspect ratio MHD equilibrium without trapped electrons. The figure is from Fig. 1 in Jenko and Dorland (2002). Reprinted with permission from Jenko and Dorland (2002). Copyright (2002) by the American Physical Society

Here, we would like to explain a little more the difference between the electron and ion adiabatic responses, as it is pointed out as the reason behind the difference in the Rogers secondary growth relative to that of the primary instability in ETG and ITG modes. The electron adiabatic response in the ITG mode comes from the lowest order parallel dynamics of the passing electrons, leading to a density response $\delta n_e/n_e \sim -e(\varphi - \bar{\varphi})/T_e$, where $\bar{\varphi}$ denotes the flux-surface average of φ. Note that the parallel motion of adiabatic electrons is limited in the flux surface and cannot respond to the potential difference between flux surfaces (Hammett 1993; Dorland 1993), allowing zonal flows to be established. On the other hand, the ion adiabatic response in the ETG mode comes from finite Larmor radius averaging in the limit of $k_\perp^2 \rho_i^2 >> 1$, which gives a density response that is proportional to φ. The ion adiabatic response is not bounded to a particular flux surface, and it can eliminate cross-flux-surface charge separation. We note that given this difference, one would expect a much weaker zonal flow generation in ETG turbulence than in ITG turbulence, and this is actually the same thing as saying the Rogers secondary is weaker in ETG turbulence, as the Rogers secondary is the secondary instability trying to establish zonal flows.

It is obvious that the saturation of ETG turbulence is important, since the saturated state ultimately determines the level of electron thermal transport that it can drive. Thus, it is reasonable to ask if there are other saturation mechanisms in addition to the one mentioned above if the difference in saturation mechanisms would lead to a different transport level, and what parameters control the particular saturation mechanism. An alternative saturation mechanism for ETG turbulence was proposed by Lin et al. (2005), where the saturation involves nonlinear toroidal coupling by transferring energy from unstable mode to damped mode. The authors used a global δf particle-in-cell (PIC) gyrokinetic code, GTC (Lin 1998), with Cyclone

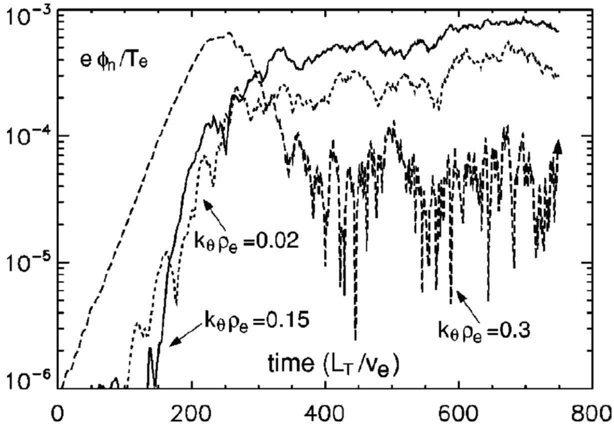

Fig. 8 Temporal evolution of three toroidal modes with $k_\theta \rho_e$ of 0.3 (dashed line), 0.15 (solid line), and 0.02 (dotted) line. Note that $k_\theta \rho_e = 0.3$ mode has the largest growth rate, saturates first, and then declines. The global simulations are based on Cyclone benchmark base case parameters (Dimits 2000) for a circular plasma in the domain of $r/a = 0.25$ to 0.75. The figure is from Fig. 2 in Lin (2005). Reprinted from Lin (2005), with the permission of AIP Publishing

benchmark base case parameters (Dimits 2000) in the middle of simulation domain [the domain is circular from $r/a = 0.25$ to 0.75, where r is the minor radius and a is the minor radius of the last closed flux surface (LCFS)] to study the electrostatic ETG mode with adiabatic ions. Figure 8 shows that the most unstable mode, $k_\theta \rho_e$ =0.3, grows from random fluctuations until it saturates at about $t \approx 210(L_T/V_{\text{the}})$ ($k_\theta = nq/r$ and $m = nq$, where n and m are the toroidal and poloidal mode numbers, respectively), while the two other lower wavenumbers, i.e., $k_\theta \rho_e$=0.15 and 0.02, start to grow at a later time and have two stages of growth, one stage of growing at much faster than linear growth rate (showing that they are nonlinearly driven) and the second one with a much lower growth rate. It is interesting to see that the lowest wavenumber mode, $k_\theta \rho_e$=0.02, actually starts to grow before the second lowest wavenumber, $k_\theta \rho_e$=0.15, showing that the downshift of ETG toroidal spectrum is not the conventional inverse cascade where local interaction in the wavenumber space is required. Note that the amplitude of the most unstable mode actually declines after the linear growth and becomes several times smaller than the other two lower wavenumber modes, showing that the spectral peak of the ETG turbulence spectrum shifts to lower wavenumbers as the ETG mode nonlinearly saturates (we note that this downshift of the ETG turbulence spectrum is not a unique feature of global simulations and also occurs in local flux-tube simulations (Nevins 2005; Dimits 2007) with similar plasma parameters). Similar to Jenko (2000) and Dorland (2000), elongated streamers are the dominant feature of the saturated ETG turbulence. However, these streamers are nonlinearly driven secondary ballooning modes with much lower n number than the linearly unstable ballooning modes. The zonal flow component, i.e., the (n=0,m=0) mode, is also generated by nonlinear mode coupling but has too low an amplitude to affect the turbulence. Furthermore, the length of the streamers is found to scale with system size with a scan in $\rho_e^* = \rho_e/a$. On the other hand, no evidence of secondary instability (KH-like instability) (Jenko 2000; Dorland 2000) was found by examining the saturation of a single toroidal eigenmode (the radially elongated ballooning structure for a particular n mode number resulting from magnetic-curvature-induced coupling in m modes was allowed to grow first to act as a pump eigenmode). Instead, the single-n eigenmode saturates from parallel mode structure modification due to the coupling with (n=0,m=1) mode. Another difference from Jenko (2000) and Dorland (2000) is that χ_e is not correlated with streamer length and at gyro-Bohm level, much smaller than what was obtained in Jenko (2000) and Dorland (2000)). In fact, the authors found that electrons do not rotate around streamers as fluid elements due to their predominant motion along magnetic field lines and that their radial excursion is only about 1/10 of the streamer length. They proposed that electron heat transport is diffusive and is driven by resonant electrons through phase-space island overlap. The authors also speculated that to reach the right saturation level, all toroidal modes should be kept in a simulation. However, a later comparison of flux-tube-filtered and global PIC simulations (Bottino 2007) shows that with a subset of toroidal modes, the saturation level is only slightly higher and the nonlinear downshift in wavenumber spectrum is correctly reproduced, showing that a subset of toroidal modes can be used instead of a full torus simulation. We note that this nonlinear toroidal mode coupling saturation mechanism has been put on a more theoretical footing in Chen (2005). In summary, there are two main findings from Lin (2005) that are in contrast to Jenko (2000) and Dorland (2000)): the initial saturation mechanism and predicted electron thermal transport. We will take a closer look at these two issues next.

2.2.2 The initial saturation mechanism

Let us discuss the initial saturation mechanism first. From above, we can reasonably conclude that the initial saturation mechanism ("initial saturation" means the saturation right after the linear phase) of the ETG mode is very different from that of the ITG mode where zonal flows play a critical role by breaking ITG streamers. In addition to the mechanism presented above (i.e., secondary instabilities and nonlinear toroidal mode coupling), other authors have also provided insight into the problem of the initial saturation mechanism of the ETG mode. In Idomura (2000b) and Idomura (2005), the authors have studied ETG turbulence in a reversed shear configuration in slab geometry (Idomura 2000b) and both reversed shear and positive shear configurations in toroidal geometry (Idomura 2005) with global gyrokinetic PIC simulations. A quasi-linear T_e profile relaxation was identified as the initial saturation mechanism for the positive shear configuration (Idomura 2005), where quasi-linear transport driven by several most unstable modes relaxes the T_e gradient on the turbulence time scale, leading to the saturation of these modes. This is different from that in Jenko (2000), although a KH-like secondary instability providing the initial saturation of ETG is not completely ruled out. However, the authors pointed out that the initial saturation level of $\chi_e/\chi_{GB} \sim 30$ is larger than $\chi_e/\chi_{GB} \sim 10$ which is a threshold determined by the competition between the primary ETG mode and secondary K–H instability in a flux-tube model proposed in Jenko and Dorland (2002). The fact that the initial saturation level in the global simulation in Idomura (2005) is higher than that in Jenko and Dorland (2002) indicates that a different saturation mechanism is at work in the global simulation. On the other hand, the reversed shear configuration has a very different saturation mechanism, where a forward (inverse) cascade in k_x (k_y) transfers fluctuation energy to $k_y \sim 0$ modes. More physically, mode-induced electron particle transport leads to charge separation and drives microscopic radial electric field leading to E×B shear flows that break up radial elongated linear mode structure (note that quasi-neutrality is not used in these simulations, since Debye shielding is included). Note that these global simulations do not have sources and, thus, profiles and driven turbulence would decay. In addition, Wang (2015), using a global particle-in-cell Gyrokinetic Tokamak Simulation (GTS) code (Wang 2010) for an ETG simulation of an NSTX RF-heated L-mode plasma, found that the initial saturation of ETG turbulence is due to a nonlocal (in the wavenumber space) strong energy coupling with electron geodesic acoustic mode, i.e., e-GAMs with high frequency and m=1. They show that in the linear phase, the most unstable mode is at $k_\theta \rho_s \sim 13$, with strong streamer features, namely $k_r << k_\theta$, and in the well-developed nonlinear phase, the dominant spectral peak has a clear downshift to $k_\theta \rho_s \sim 6$ due to nonlinear coupling with e-GAMs and low-frequency zonal flow. Furthermore, with positive shear configuration in a slab geometry, Li and Kishimoto (2008) proposed another initial saturation mechanism associated with long-wavelength anisotropic structures (LWSs) (Kim and Diamond

2003). These secondary large-scale instabilities act as an intermediator to nonlinearly couple all k_y modes, and thus, linearly unstable modes can be coupled with high k_y damped modes, saturating the most unstable modes and forming large-scale eigenmodes. These LWSs have a very similar role as the quasi-modes in nonlinear toroidal coupling proposed in R Lin (2005).

We note that magnetic shear, $\hat{s}$, seems to be a critical physics parameter for controlling the initial saturation mechanism (Jenko 2000; Idomura 2000a; Dorland 2000; Jenko and Dorland 2002) and two regimes of $\hat{s}$ showing distinct electron transport features are normal-positive-shear and weak/negative-shear regimes. Obviously, negative magnetic shear is often associated with ITBs (Kessel 1994; Shirai 1998; Stallard 1999; Akers 2003; Connor 2004; Yuh 2009, 2011). The proposed mechanisms should be preferred in their respective regimes and act accordingly to generate the expected turbulence saturation in a particular $\hat{s}$ regime. As an example, the Rogers and Cowley secondary instabilities proposed in Jenko and Dorland (2002) actually fit into the picture quite nicely. The Rogers secondary instability relies on E×B perpendicular flow and is more likely to be important for the perpendicular-flow-dominant toroidal ETG mode, and on the other hand, the Cowley instability depends on the parallel flow and thus is more likely to be important for the parallel-flow-dominant slab ETG mode which is expected to be important for the reversed shear (including negative shear) regime (Idomura 2000b). In addition, because the Cowley secondary instability would have a much larger growth rate than the Rogers secondary instability, given the same primary instability amplitude (both growth rates are proportional to the amplitude of the primary instability and the constant of proportionality is much larger for the Cowley secondary instability), the Cowley secondary instability can more effectively break up the unstable linear modes (Jenko and Dorland 2002), which could be a reason why the predicted electron thermal transport is much larger in the positive $\hat{s}$ case. Given all the initial mechanisms published in the literature, what is the parametric dependence for different ETG initial saturation mechanisms is still an open question. However, given a finite boundary toroidal system, some kind of nonlinear mode coupling would reasonably be expected to play a role in the ETG mode nonlinear saturation.

2.2.3 The roles of zonal flows

However, one caveat is that although the initial saturation mechanism is a good qualitative indicator of turbulent transport level, the subsequent nonlinear evolution could be more important for quantitative predictions. One example seen in Fig. 7 is that with an initial saturation of the “curv ETG” at $t \approx 35$, it subsequently grows to a much larger value. Thus, properly treating the nonlinear evolution phase is very important for achieving accurate predictions. This is where zonal flows are expected to have greater importance. As we have discussed, zonal flows are not expected to be important for the initial saturation of unstable ETG modes due to their small amplitude at an early time. However, due to the variety of mechanisms of zonal flow generation (Li and Kishimoto 2002, 2004; Idomura 2000b, 2005; Kawai 2020), zonal flows are almost always generated, and it could be important in determining the final saturation level in transport depending upon the specific parameter regime.

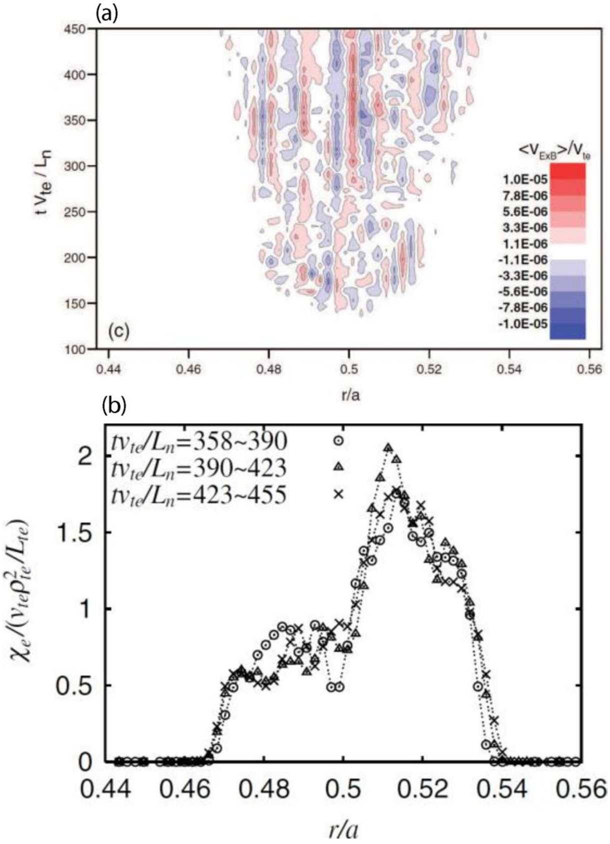

Fig. 9 **a** Normalized E×B flow as a function of normalized minor radius (*r*/*a*) and time ($t/(L_n/V_{\mathrm{the}})$); **b** normalized electron thermal diffusivity as a function of *r*/*a* averaged over three time periods denoted in the figure. Note the negative magnetic shear region is at $r/a < 0.5$ and the positive magnetic shear region is at $r/a > 0.5$. The global simulation is based on Cyclone benchmark base case parameters (Dimits 2000) for a circular plasma in the domain of $r/a = 0.2$ to 0.8. Panel a is adapted from Fig. 14 and panel b is adapted from Fig. 15 in Ref. (Idomura 2005), with the permission of International Atomic Energy Agency

One important example is ETG turbulence in the reversed/negative $\hat{s}$ plasmas, where the ETG mode can be effectively treated as the slab ETG mode (Idomura 2005). The global gyrokinetic PIC simulations show that quasi-steady zonal flows start to appear at about $t = 300$ (L_n/v_{the}) in the negative-shear region $(r/a < 0.5)$ and are sustained until the end of simulations (see Fig. 9a and note that the initial saturation is at about $t \sim 160 - 207$ (L_n/v_{the})). Although not shown here, we note that a secondary instability with $k_\theta \rho_e \sim 0.1$ is excited in the negative shear region during the nonlinear evolution phase around $t = 255$ (L_n/v_{the}). After the saturation of this secondary mode, quasi-steady zonal flows shown in Fig. 9a are sustained and thus, ETG turbulence is regulated. On the other hand, large streamers with $k_\theta \rho_e \sim 0.17$ appear in the positive shear region $(r/a > 0.5)$. The zonal flow (streamer) formation in the negative-shear (positive shear) region leads to a large difference in χ_e in two regions and a jump in the χ_e can be seen at the $q_{\min}$ surface at $r/a = 0.5$ as seen in Fig. 9b. The simulation results also show that zonal flows are not important for the positive magnetic shear (both in the positive shear region in the reversed shear configuration and in the positive shear configuration), where large streamer structures seen in the quasi-steady state that stem from the toroidal coupling of ballooning type modes are sustained. This conclusion for the positive magnetic shear is in agreement with the other studies reported in the literature (Jenko 2000; Idomura 2000a; Dorland 2000; Jenko and Dorland 2002; Li and Kishimoto 2002, 2004; Idomura 2005; Lin 2005; Chen 2005). In the slab geometry, this preferential generation of large secondary structures like zonal flows (streamers) in weak shear (positive shear) regime is shown to relate to the spectral anisotropy of turbulent fluctuations, namely zonal flows preferred for radially elongated fluctuations and streamers preferred for poloidally elongated fluctuations (Li 2005). Even with positive magnetic shear, zonal flows may become important in the final steady-state phase as demonstrated in Parker (2006); Colyer (2017). Parker 2006 shows that the fine zonal flows with $k_r\rho_i > 1$ and $k_r\rho_e < 1$ continue to grow in proportion to time after the initial saturation of ETG turbulence and eventually suppresses ETG turbulence by E×B shear. In Colyer (2017), the authors studied this problem with electrostatic ETG flux-tube simulations with a MAST H-mode plasma equilibrium (Field et al. 2004) using the GS2 gyrokinetic code (Kotschenreuther 1995), where zonal flows

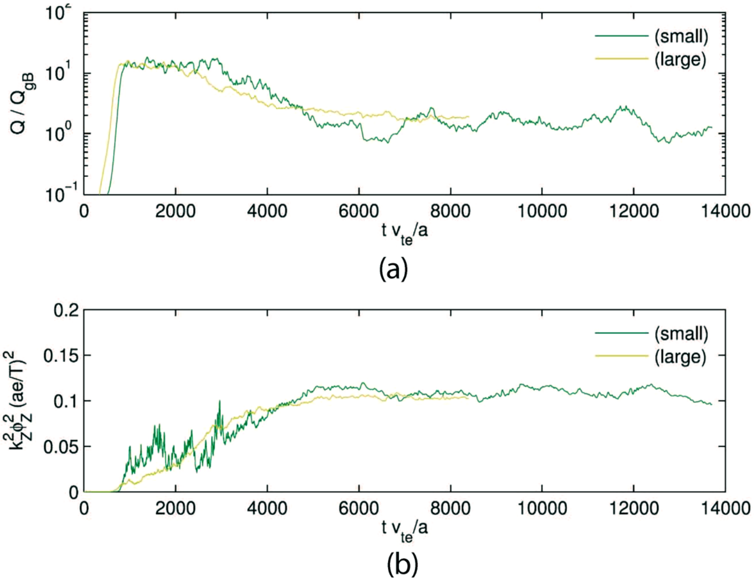

Fig. 10 **a** Temporal evolution of normalized heat flux, Q/Q_{gB}, (normalized to electron gyro-Bohm unit); **b** the zonal velocity squared, $(k_Z\phi_Z)^2$, for two simulations (with large simulation box (yellow line) and with small simulation box (green line)) with electron collisionality $\mu = 0.2\mu_{nom}$, where $\mu_{\rm nom}$ is the experimental electron collisionality and $a/L_{T_e} = 3.3$. The local flux-tube GS2 simulations are based on equilibrium parameters at $t = 0.289$ s and $r/a = 0.65$ of the MAST H-mode shot 8500 with an NBI heating power of 2 MW. The figure is reprinted from Fig. 2 in Ref. (Colyer 2017). © IOP Publishing. Reproduced with permission. All rights reserved

are seen to grow slowly after the initial saturation (at $t \sim 800\ (a/v_{the})$) of the ETG mode (see Fig. 10b), feedback to the underlying ETG turbulence to reduce electron heat flux, and eventually reach a steady state with a much lower electron heat flux than the quasi-steady phase right after the initial saturation (see Fig. 10a). Note that these simulations were run for a much longer time than any other simulation presented above and the run time is much longer than the electron-ion collision time (which is about 250 (a/v_{the})). The authors show that the saturation of zonal flows is due to the balancing between the zonal flow drive and collisional damping due to electron-ion collisions (Kim 2003), which results in a collisionality dependence of normalized electron heat flux, $Q/Q_{gB} \propto \nu_e^*$. This observation potentially could be consistent with the energy confinement scaling for STs (Kaye 2007a; Valovič 2011). However, we must caution that whether the predicted electron thermal transport in the late-time low-transport phase (see Q/Q_{gB} at $t \gtrsim 6000\ a/V_{te}$ in Fig. 10a) is able to match the experimental electron heat flux at the simulated radial location is unclear in Colyer (2017). We will come back to this point in Sect. 3. Note this conclusion of needing long-time simulations for ETG turbulence is not necessarily conflicting with other simulation results above. The ST parameter regime is quite different from that of conventional tokamaks, e.g., the cyclone base benchmark case often used for ETG turbulence simulations. The authors also pointed out that for the cyclone base case, the ETG mode is far from the linear threshold while in the MAST case shown in Fig. 10, the ETG mode is close to the linear threshold, which may also play a role in the long-time zonal flow evolution. We also note that ETG turbulence could also be saturated by ion-scale zonal flow due to cross-scale coupling (between ion and electron scales) with quite different parameters from MAST (Nakata 2012; Howard 2016; Holland 2017), which will be discussed in Sect. 2.2.5.

2.2.4 Consistent electron thermal transport prediction from gyrokinetic codes

Now, we can move on to the problem of much lower electron thermal transport predicted in Lin (2005) in comparison with Jenko (2000); Dorland (2000) even with similar equilibrium conditions. It is pointed out that the discrete particle noise in PIC simulations may be responsible for the lower transport (Nevins 2005), where the ETG mode is found to be linearly stabilized by spatial diffusion due to discrete particle noise. With the understanding of the noise issue of PIC codes, a cross-code verification exercise on ETG turbulence was carried out by Nevins (2006, 2007) with five different gyrokinetic codes including GYRO (Candy and Waltz 2003), GS2 (Kotschenreuther 1995), GENE (Jenko 2000), PG3EQ (Dimits 1996), and GEM (Chen and Parker 2003). Note that the first three codes are continuum codes and the last two are PIC codes. We note that PIC and continuum methods are merely numerical schemes to solve the gyrokinetic equations and both methods have cons and pros. We refer interested readers to a review of gyrokinetic simulations in Garbet (2010) for an extensive discussion of these numerical methods. In contrast to the typical Cyclone benchmark case for ITG turbulence, a slightly different operating point (with $\hat{s}$ changed to 0.1) was used for the benchmark of ETG turbulence across these different numerical codes. Note that this change of operating point makes electron turbulence moderate, so that the full toroidal physics, e.g., trapped electrons, can be

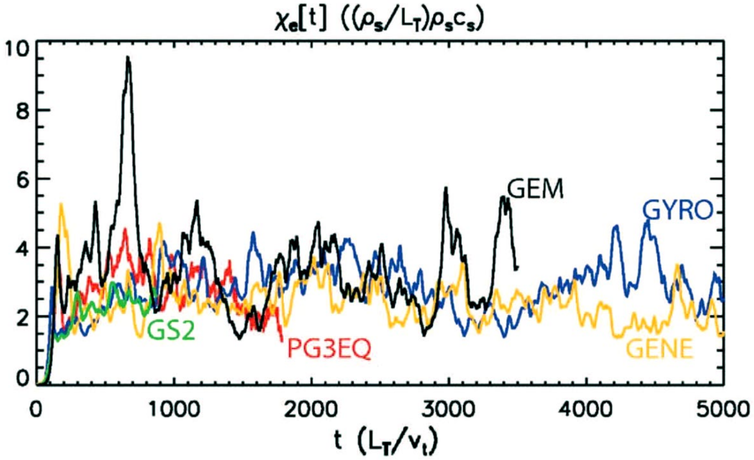

Fig. 11 The electron thermal conductivities from GEM (black), PG3EQ (red), GYRO (blue), GS2 (green), and GENE (yellow). The simulations are based on Cyclone benchmark base case parameters (Dimits 2000) for a circular plasma with $\hat{s}$ changed to 0.1, adiabatic ions, and trapped electrons including only electrostatic fields. The figure is from Fig. 1 in Ref. (Nevins 2007). Reprinted from Ref. (Nevins 2007), with the permission of AIP Publishing

retained (trapped electrons are neglected in Dorland (2000) and Jenko (2000) due to violent ETG turbulence with the typical Cyclone benchmark case). Assumptions of electrostatic turbulence and adiabatic ion response were also made. Good agreement in electron thermal diffusivity, χ_e, can be easily seen in Fig. 11. Quantitatively, the time-interval weighted average of electron thermal diffusivity over $t > 1000\ L_T/v_{\mathrm{the}}$ gives $\langle\chi_e\rangle/\chi_{e,gB} \approx 3.0 \pm 0.13$, were $\chi_{e,gB} = (\rho_e/L_T)\rho_e v_{\mathrm{the}}$. Although this value is much lower than reported in Jenko (2000); Dorland (2000), it still breaks the electron gyro-Bohm limit by a factor of three. Further scans in $\hat{s}$ show that the runs with adiabatic ions and $\hat{s} > 0.4$ would not saturate and give huge electron thermal transport with all codes. This is substantially different from Jenko (2000) and Dorland (2000), where $\chi_e/\chi_{e,gB} \approx 13$, and the reason behind this difference is found to be whether trapped electrons are included. Using kinetic ions instead of adiabatic ions for $\hat{s} > 0.4$ is shown to solve this non-saturation problem, and a steady increase in $\langle\chi_e\rangle/\chi_{e,gB}$ from 4.4 to 14.3 (with kinetic ions) is observed from $\hat{s} = 0.1$ to 0.6 (Nevins 2006). A larger $\hat{s}$ may reduce electron thermal transport due to the magnetic shear stabilization effect. Comparing with electron thermal diffusivities observed in DIII-D tokamak (Stallard 1999) and National Spherical Torus Experiment (NSTX) spherical tokamak (Stutman et al. 2004), the authors show that the predicted $\langle\chi_e\rangle/\chi_{e,gB}$ is sufficient to explain experimental observations (Nevins 2006). We have to note here that the reference parameters used in these simulations are for conventional tokamaks which are quite different from NSTX parameters, and thus, it requires special attention when one tries to address NSTX electron thermal transport. Some specific comparisons with NSTX experiments are presented in Sect. 3.

2.2.5 Multi-scale interactions between ETG and ion-scale turbulence

Multi-scale interaction is another important issue for ETG-turbulence-driven transport. The ETG mode is usually not the only unstable mode in high-temperature fusion plasma, and ion-scale (long-wavelength) modes, e.g., ITG and TEM, often coexist in the same parameter space. We note that there are exceptions where ion-scale modes are almost completely suppressed by E×B shear flow or reversed magnetic shear, e.g., in ITBs and STs, and ion thermal transport is reduced to the neoclassical level. Ion-scale turbulence could affect ETG turbulence through modification of background gradients, E×B shearing within ion-scale eddies, and normal energy cascade (from low-k to high-k) (Jenko 2004; Waltz 2007; Holland and Diamond 2004; Hardman 2019, 2020). Furthermore, in light of the aforementioned formation and interactions of large-scale (compared to electron gyroradius) secondary structures, e.g., streamers, zonal flows, e-GAMs, and more generally LWSs, with ETG turbulence, it is conceivable that ETG turbulence could affect ion-scale turbulence through these large secondary structures despite the large-scale separation in the characteristic spatial scale (in gyroradius) between ion and electron-scale modes (Li and Kishimoto 2002, 2003). Due to limitations of computational resources, earlier gyrokinetic studies usually separate simulations as ion-scale or electron-scale, namely artificially limiting the resolved wavenumber range in simulations. Strictly speaking, such a practice assumes the existence of distinct scale separation between ion and electron-scale turbulence (no overlap or no nonlocal mode coupling) due to the large mass difference between electron and ion (e.g., $m_d/m_e \sim 3600$ with m_d as the deuterium mass). However, as we just mentioned, due to the existence of the large-scale secondary structures of ETG turbulence and the high-k tail of ion-scale turbulence, it may not be possible to separate the dynamics into two distinct scales. Thus, it is reasonable to expect that the total electron thermal transport is not a simple addition of predictions from ion- and electron-scale simulations. In one early theoretical investigation (Li and Kishimoto 2002, 2003), Li and Kishimoto proposed a theory of nonlocal radial mode coupling between ITG turbulence and smaller scale zonal flows generated by ETG turbulence. Through nonlinear gyro-fluid simulations, they found that such a coupling has little effect on ITG turbulence when the ITG drive is strong. However, when ITG turbulence is weak, e.g., close to marginality, such a coupling could produce a large variation in ion thermal transport. Although it is commented that given weak zonal flow generated by ETG, this mechanism may not be important (Jenko 2004), in light of recent long-time simulations showing robust growth of zonal flows and their eventual regulating ETG turbulence (Colyer 2017), this mechanism may be plausible after all.

A theoretical investigation was carried out by Holland and Diamond (2004), where they performed analytic analyses of the coupling effects between drift-ion temperature gradient (DITG) (Horton 1981; Lee and Diamond 1986) turbulence (the ITG mode driven by the geometric mean of the ion pressure gradient and the unfavorable magnetic curvature) and ETG turbulence. They found that although the random flow shearing due to the short-wavelength portion of DITG turbulence on ρ_e scale ETG turbulence is weak, its effect on large-scale secondary structure (e.g., streamers and zonal flows) driven by ETG turbulence is significant, and thus, DITG turbulence can nonlinearly suppress ETG turbulence through flow shearing. They also found that DITG turbulence could induce fluctuations in the T_e gradient that drives the ETG mode, leading to a nonlinear modulation of ETG turbulence. In addition, the back reaction of ETG turbulence to DITG turbulence is found to scale with $\sqrt{m_e/m_i}$ and thus is insignificant. However, in their analysis, the linear growth rate is taken as approximately the nonlinear turbulence decorrelation rate, which is an overestimate (Howard 2016). With a real nonlinear turbulence decorrelation rate, the back reaction of ETG turbulence could be stronger, which is potentially in agreement with the enhancement of ITG turbulence by ETG turbulence seen in Howard (2016) when ITG turbulence is weakly driven (see later discussions). Early multi-scale simulations used reduced electron–ion mass ratio, e.g., $\sqrt{m_i/m_e} = 20$ or 30 (Waltz 2007; Candy 2007; Görler and Jenko 2008) to make required computational time realistic.

Another analytical analysis of multi-scale interaction was carried out by Hardman (2019). With $(m_e/m_i)^{1/2}$ as the small expansion parameter, the local δf gyrokinetic equations are expanded keeping terms with leading order of $(m_e/m_i)^{1/2}$ to obtain scale-separated equations for electrostatic turbulence (Hardman 2019). Although this expansion procedure is mathematically rigorous, it relies on the assumption of clear scale separation between ion and electron turbulence, namely that there is negligible turbulence spectral power in the intermediate spatial scale between ρ_i and ρ_e perpendicular to the equilibrium magnetic field. As a result of this assumption, the obtained scale-separated equations do not contain multi-scale interaction physics due to intermediate-scale structures, e.g., ETG streamers and zonal flows, which is different from the previous studies (Li and Kishimoto 2002, 2003; Holland and Diamond 2004). In the leading order of $(m_e/m_i)^{1/2}$, it is shown that the ion-scale turbulence evolves independently from the electron-scale turbulence, and the multi-scale interactions only exist in the electron-scale electron gyrokinetic equation, in the form of $\bar{\vec{v}}_E \cdot \nabla\tilde{g}$ and $\tilde{\vec{v}}_E \cdot \nabla\bar{g}$, where $\bar{\vec{v}}_E$ and $\tilde{\vec{v}}_E$ are the ion- and electron-scale E×B drifts, respectively; $\bar{g}$ and $\tilde{g}$ are the ion- and electron-scale electron distribution functions, respectively. The $\bar{\vec{v}}_E \cdot \nabla\tilde{g}$ term represents the convection of the electron-scale electron distribution function by the ion-scale E×B drift, which introduces velocity shear of $\tilde{g}$, while the gradient term $\nabla\bar{g}$ in $\tilde{\vec{v}}_E \cdot \nabla\bar{g}$ should be added to the equilibrium gradient drive of the instability, representing the modification of the equilibrium gradient by the ion-scale turbulence. Note that the velocity shear of $\tilde{g}$ from the $\bar{\vec{v}}_E \cdot \nabla\tilde{g}$ term can only occur in the parallel direction (the ion- and electron-scale turbulence is both assumed to have system scale in the parallel direction), since due to the scale separation, $\bar{\vec{v}}_E$, of the ion scale does not vary on the perpendicular scale of the electron-scale turbulence. The parallel variation of the gradient term $\nabla\bar{g}$ in $\tilde{\vec{v}}_E \cdot \nabla\bar{g}$ means that the instability drive for the electron-scale turbulence is not uniform in the parallel direction anymore. The multi-scale interaction effects from both the $\bar{\vec{v}}_E \cdot \nabla\tilde{g}$ term and the $\tilde{\vec{v}}_E \cdot \nabla\bar{g}$ term are verified using gyrokinetic simulations with small electron-scale flux tubes embedded in a larger ion-scale flux tube (Hardman 2020). In particular, it is shown that strongly driven ion-scale turbulence can stabilize strongly driven ETG modes through the parallel shearing of the ion-scale

E×B flow and the parallel variation of the ion-scale electron density gradient. On the other hand, the near-marginal ion-scale turbulence could change the linear growth rate of weakly driven ETG modes by an order unity factor by modifying the effective background T_e and n_e gradients, while the two stabilizing effects for the strongly driven ion-scale turbulence mentioned above become unimportant. We note that this parallel velocity shearing effect from the ion-scale turbulence is apparently missing from Holland and Diamond (2004). We note that although the conclusion that the back reaction of the electron-scale turbulence to the ion scale is negligible is in agreement with Holland and Diamond (2004), the back reaction of ETG turbulence in Holland and Diamond (2004) is of order $\sqrt{m_e/m_i}$, while it is of a higher order than $\sqrt{m_e/m_i}$ in Hardman 2019. We also note that this conclusion is in agreement only with the strongly driven case in Li and Kishimoto (2002, 2003).

By comparing simulations resolving both ion and electron scales and simulations only resolving ion scale or electron scale, Waltz (2007) show that there is little coupling between ion-scale and electron-scale turbulence in terms of the driven transport in a particular range (ion scale vs. electron scale), e.g., resolving electron-scale turbulence is not important for determining transport driven in the ion scale and vice versa. ETG-turbulence-driven transport manifests as a high-k tail in the transport spectrum without a visible peak in the ETG mode wavenumber range ($k_\theta \rho_s > 1$, where ρ_s is ion gyroradius with ion sound speed). Similar results were also observed in Candy (2007) which, in addition, shows the suppression of ETG turbulence (both transport and turbulence intensity) when the ion-scale drive was included (see Fig. 12) and a very little back reaction of ETG turbulence to ITG turbulence (consistent with Li and Kishimoto (2002), Li and Kishimoto (2003), Holland and Diamond (2004) and Hardman (2019) as pointed out). Clearly, linear theories could not

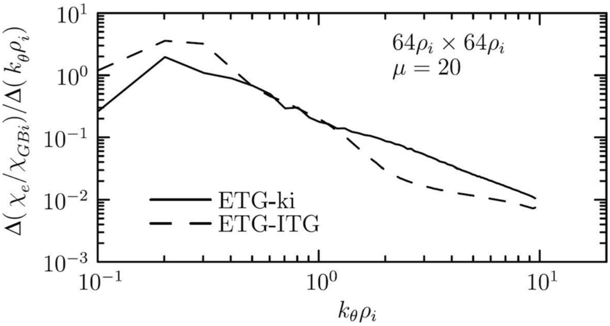

Fig. 12 Normalized electron thermal diffusivity spectra from a kinetic ion ETG simulation (solid line), i.e., no ITG drive ($a/L_{n_i} = a/L_{T_i} = 0.1$), and a kinetic ETG–ITG coupled simulation (dashed line), i.e., with ITG drive ($a/L_{n_i} = a/L_{n_e}$ and $a/L_{T_i} = a/L_{T_e}$). The increase of thermal diffusivity in the ion scale ($k_\theta \rho_i < 0.4$) in the kinetic ETG–ITG coupled simulation is due to the ITG drive, while there is an obvious decrease in thermal diffusivity in the electron-scale ($k\theta \rho_i > 1$) due to the ETG–ITG coupling, where k_θ is the binormal direction perpendicular to the magnetic field. These ion-scale ETG simulations were performed with the GYRO code based on Cyclone benchmark base case parameters (Dimits 2000) for an unshifted circular plasma with trapped electrons and reduced $m_i/m_e = 400$. The figure is reprinted from Fig. 3a in Ref. (Candy 2007). © IOP Publishing. Reproduced with permission. All rights reserved

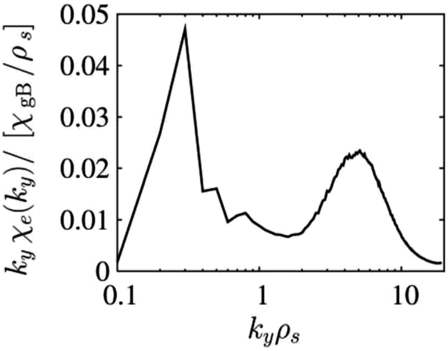

Fig. 13 The weighted normalized electron diffusivity spectrum. Note that using a weighting factor of k_θ with $\chi(k_y)$ makes the area under the curve represent electron thermal diffusivity in the linear-log plot. Here, k_y is the wavenumber in the binormal direction perpendicular to the magnetic field, and $\chi_{gB} = C_s\rho_s^2/R$, where C_s is the ion sound speed. The size of the simulation box is $64\rho_i \times 64\rho_i$. This collisionless electrostatic ion-scale ETG simulation was performed with the GENE code based on Cyclone benchmark base case parameters (Dimits 2000) for an unshifted circular plasma with $R/L_n = 0$, $R/L_{T_i} = 5.5$, $R/L_{T_e} = 6.9$, and reduced $m_i/m_e = 400$. The figure is from the right panel of Fig. 5 in Ref. (Görler and Jenko 2008). Reprinted with permission from Ref. (Görler and Jenko 2008). Copyright (2008) by the American Physical Society

explain the observed suppression of ETG turbulence by ITG turbulence. Note these multi-scale simulations are based on DIII-D mid-core parameters and have a very strong ITG drive, i.e., $R/L_{T_i} = 9$ for Waltz (2007) and $R/L_{T_i} = 6.9$ (Candy 2007) where the latter comes from the well-known cyclone benchmark base case (Dimits 2000) which is the basis for Candy (2007). The strong ITG may dominate the plasma turbulence dynamics, which could potentially render ETG turbulence almost irrelevant. Recognizing this, Görler and Jenko performed multi-scale simulations based on the cyclone benchmark base case parameter with reduced ITG drive, i.e., $R/L_{T_i} = 5.9$, using the GENE code vcvb(Görler and Jenko 2008), where they clearly found a scale separation in the electron thermal transport spectrum, namely clear spectral peaks in the ion-scale wavenumber range and the electron-scale wavenumber range (see Fig. 13), in contrast to those in Waltz (2007) and Candy (2007). Given the reduction in R/L_{T_i} is about 14% from 6.9 to 5.9 in comparison with the cyclone base case parameters (well within experimental uncertainty), such a sensitivity of multi-scale dynamics on the ITG drive is surprising and shows that ETG turbulence could be an important contributor to electron thermal transport. Despite the reduced mass ratio (only $\sqrt{m_i/m_e}$ up to 30) and simple circular magnetic geometry used in these simulations (without plasma shaping), they provide important guidance in the relation between ITG drive and the importance of ETG turbulence. We note that a similar scale separation in the electron thermal transport spectrum is also shown in Howard (2014) and Howard (2016) [see Fig. 3 in Ref. (Howard 2014) and Fig. 2 in Ref. (Howard 2014)] from a multi-scale simulation with realistic deuterium–electron mass ratio with all experimental inputs from an Alcator C-MOD L-mode discharge.

Using realistic mass ratios, meaning that $\sqrt{m_i/m_e} \sim 43$ (for hydrogen) and 60 (for deuterium), coupled ion-electron-scale simulations were carried out and reported in a series of papers by Howard (2014), Howard (2015), Howard (2016), Howard (2016), Holland (2017), Maeyama (2015), Maeyama (2017a), Maeyama (2017b), and Maeyama (2022). Particularly, in the earliest paper in this group, Howard (2014) began to use realistic deuterium–electron mass ratio together with all experimental inputs from Alcator C-MOD discharges. This is important, since previous multi-scale simulations are all based on idealized plasma equilibria (e.g., circular flux surfaces, large ITG and ETG driving force and reduced mass ratio, etc.) which is perfectly fine for exploration of physics of cross-scale coupling but is only remotely relevant to real tokamak experiments, particularly tokamaks with strong plasma shaping. The work of Howard et al. made it possible to directly compare simulation-predicted plasma transport with those inferred from experiments, a crucial part of model validation. Here, we defer the validation part to Sect. 3 and focus on the cross-scale coupling physics. In Howard (2014), the authors show a scale separation in ITG- and ETG-turbulence-driven electron thermal transport in multiscale simulations like that found in Görler and Jenko (2008). They also found an enhancement in plasma transport in the ion-scale wavenumber range in multi-scale simulations compared with ion-scale-only simulations. Although the mechanism behind this enhancement was not identified by the authors, they pointed out that the enhancement is dominated by a modest increase (~ 10 to 20%) of ion-scale fluctuation, while turbulence correlation lengths and cross-phase angles between fluctuating quantities show only minimum variation. Another group of authors Maeyama (2015) and Maeyama (2017b) focused on the physics underlying multi-scale interactions by extending previous studies to realistic hydrogen–electron mass ratio with cyclone base case parameter, including finite β effects, although the cyclone base case parameter is based on DIII-D deuterium plasmas and the realistic hydrogen–electron mass ratio used in the simulation is still a factor of two smaller than experiment. However, their investigation is still meaningful for revealing cross-scale coupling physics, and the realistic deuterium–electron mass ratio should be used when comparing with experiments as Howard et al. and Howard (2014), Howard (2015), Howard (2016), Howard (2016) and Holland (2017) have done. Comparing ITG-ETG coupled (full-k) simulation with ITG-only (low-k) and ETG-only (high-k) simulations in Fig. 14, the authors show that strongly unstable electrostatic-ITG-driven turbulence severely suppresses ETG turbulence (see the difference between full-k and high-k simulations in Fig. 14a), while ITG turbulence is essentially unaffected by ETG turbulence seen by comparing low-k and full-k simulations. On the other hand, including a finite $\beta = 2\%$, ITG turbulence is seen to be reduced in the low-k simulation in Fig. 14b compared to that in the low-k simulations in Fig. 14a, while ITG turbulence is seen enhanced in the full-k simulation with ETG turbulence again suppressed but to a lesser extent compared with that shown in Fig. 14a. We note that this reduction of ETG turbulence by ITG turbulence is also seen in Fig. 12 (Candy 2007). We also note that weaker ITG turbulence due to finite β stabilization leading to less suppressed ETG turbulence shown in Fig. 14b is consistent with that shown in Görler and Jenko (2008) where ITG turbulence is reduced by lowering R/L_{T_i}. On the other hand, the reduction of ITG turbulence is probably more dramatic in Görler and Jenko (2008), so a clearer scale separation in the electron thermal transport spectrum is seen in Fig. 13.

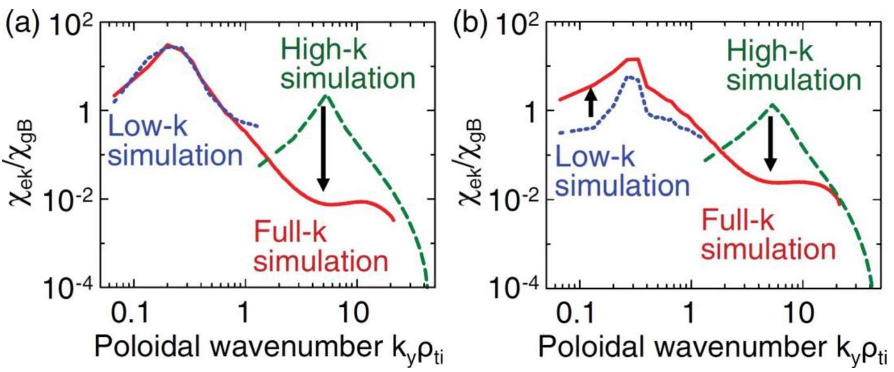

Fig. 14 Poloidal wavenumber spectra of normalized electron thermal diffusivity for **a** electrostatic ($\beta = 0.04\%$) and **b** electromagnetic ($\beta = 2\%$) cases. Results shown are from full-k simulations (red solid line), low-k simulations, resolving only $k_y\rho_{ti} < 1.3$, (blue dotted line), and high-k simulations, resolving only $k_y\rho_{ti} > 1.3$ (green dashed line), where ρ_{ti} is the ion gyroradius. These nonlinear flux-tube simulations were performed with the GKV code (Watanabe and Sugama 2005; Maeyama 2013a, b) based on Cyclone benchmark base case parameters (Dimits 2000) for an unshifted circular plasma with real hydrogen-to-electron mass ratio and finite β (compressional magnetic field perturbations are neglected). The figure is from Fig. 2 in Ref. (Maeyama 2015). Reprinted with permission from Ref. (Maeyama 2015). Copyright (2015) by the American Physical Society

To study the cross-scale coupling, the authors used the method of gyrokinetic entropy transfer (Nakata 2012). They showed that the nonlinear entropy transfer of ETG turbulence streamers is dominated by interactions with higher-k ($k_\perp\rho_{ti} \sim 1$) ITG turbulence eddies (see Fig. 15). The entropy transfer is defined as $I_{\vec{k}} = \sum_{\vec{p}}\sum_{\vec{q}} J_{\vec{k}}^{\vec{p},\vec{q}}$, where $J_{\vec{k}}^{\vec{p},\vec{q}}$ is the triad transfer describing entropy transfer from wavenumbers $\vec{p}$ and $\vec{q}$ to wavenumber $\vec{k}$ under the resonant condition, $\vec{p} + \vec{q} + \vec{q} = 0$ (see detailed definition of $J_{\vec{k}}^{\vec{p},\vec{q}}$ in Maeyama (2015)). Figure 15 shows the q wavenumber spectrum of $J_{\vec{k}}^{\vec{p},\vec{q}}$ for a particular ETG streamer wavenumber $\vec{k}$ =(0,4.4)ρ_{ti}^{-1}. Due to the symmetry property of the $J_{\vec{k}}^{\vec{p},\vec{q}}$, i.e., $J_{\vec{k}}^{\vec{q},\vec{p}} = J_{\vec{k}}^{\vec{p},\vec{q}}$, Fig. 15 contains all the information for this particular $\vec{k}$. It is shown that $J_{\vec{k}}^{\vec{p},\vec{q}}$

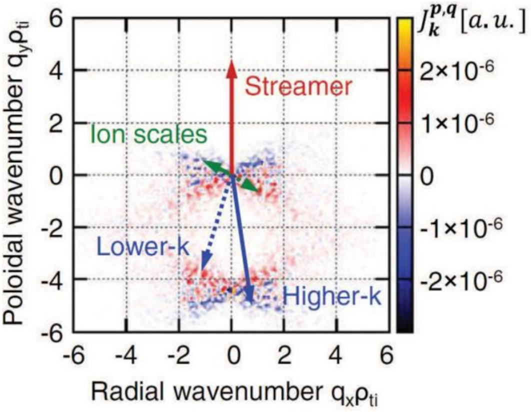

Fig. 15 q Wavenumber spectrum of the normalized triad transfer function, $J_{\vec{k}}^{\vec{p},\vec{q}}$ for a particular streamer $\vec{k}$ =(0,4.4)ρ_{ti}^{-1} which is averaged over a time period of $60 < tv_{ti}/R < 80$ with $\beta = 2\%$. Dominant triad couplings are denoted by arrows. Results are based on the full-k simulation shown in Fig. 14. The figure is from Fig. 3 in Ref. (Maeyama 2015). Reprinted with permission from Ref. (Maeyama 2015). Copyright (2015) by the American Physical Society

for the total entropy to the streamer, $\vec{k} = (0, 4.4)\rho_{ti}^{-1}$, has contributions from couplings of both lower k modes (lower than the streamer wavenumber, but still much higher than that of the ITG mode) and higher k modes (higher than the streamer wavenumber) with ITG modes of $k_\perp \rho_{ti} \sim 1$. Particularly, we note that $J_{\vec{k}}^{\vec{p},\vec{q}}$ with higher-k modes is negative, meaning that the streamer gives entropy to higher-k modes, while $J_{\vec{k}}^{\vec{p},\vec{q}}$ with lower k modes is positive, meaning that the streamer takes entropy from lower k modes. Thus, the normal entropy cascade occurs through nonlinear mode coupling with $k_\perp \rho_{ti} \sim 1$ short-wavelength ITG eddies and supports a similar conclusion from a theoretical point of view in Holland and Diamond (2004), implying that a stronger ITG turbulence would facilitate such a cascade and suppressing ETG streamers. Note that the shearing of ETG turbulence by ion-scale fluctuations was also studied with a different method in Howard (2016). The entropy transfer has been used to study the back reaction of ETG turbulence on ITG turbulence. The authors find that ETG turbulence contributes to the damping of ITG zonal flow and increases the damping rate by about 20 percent. Such a damping effect is particularly important as ITG turbulence is close to marginal stability as the finite β case shown in Fig. 14b, and the damping leads to weaker zonal flows, thus the enhancement in ITG-turbulence-driven transport seen in Fig. 14b. This damping effect also means that the efficiency of generating zonal flows by ion-scale turbulence would be lower with the presence of electron-scale turbulence compared with ion-scale only simulations, which was quantitatively verified in the paper. A similar argument was also presented in Howard (2016). These more realistic studies of ion-electrons-scale-turbulence have revealed previously neglected multi-scale physics, and they have shown that both ion- and electron-scale turbulence could be significantly affected, namely suppressed electron-scale turbulence in the presence of strong ion-scale drive and enhanced ion-scale turbulence and a scale separation in the electron thermal transport spectrum when ion-scale turbulence is close to marginality. The multiscale interactions between the ETG mode and MTM/TEM have been investigated with the method of gyrokinetic entropy transfer (Nakata 2012) in Maeyama (2017a) and Maeyama (2022)). Similar to the findings in Maeyama (2015), it is found that the ion-scale turbulence (due to ITG, MTM, or TEM) tends to suppress the electron-scale turbulence (ETG turbulence in this case), while the electron-scale turbulence tends to damp large-scale structures, i.e., ion-scale zonal flows in the case of ITG-ETG interaction, radially localized current sheets in the case of MTM-ETG interaction, and the resonance between trapped electrons and TEM in the case of TEM–ETG interaction (as collisionless TEM is considered in Maeyama (2022)). It can be seen that ITG could be enhanced due to ETG turbulence, while MTM and TEM tend to be suppressed.

3 Experimental studies of ETG turbulence and electron thermal transport

As we have presented in Sect. 2, ETG turbulence is now a major candidate in explaining highly anomalous electron thermal transport observed in fusion devices thanks to great advances in modern gyrokinetic theory, gyrokinetic codes, and computational power. On the other hand, models and numerical codes have to be validated with experiments with regard to ETG turbulence, which is the focus of this section. There are different levels of validation with experiments. The most straightforward one is to compare the predicted critical threshold and/or electron thermal transport by theoretical models and numerical codes with experiments, usually requiring the variation of R/L_{T_e} in the experiment to assess critical R/L_{T_e} threshold or in numerical simulations within experimental uncertainty to assess the sensitivity of the dependence of electron thermal transport on R/L_{T_e}, also called stiffness. The experimental electron thermal transport may be matched with the simulated electron thermal transport by varying simulation-input R/L_{T_e} within the experimental uncertainty of R/L_{T_e} if electron thermal transport is stiff enough, and it also means that the experimental profile would remain close to the local threshold and can be easily compared with simulations. However, if multiple modes are actually present in the experiment, such matching may not be achievable with ETG turbulence simulations alone. Thus, in this first level of validation, it is important to carry it out in a parametric regime where the ETG mode is the dominant instability. The next level of validation may include matching ion and electron thermal transports simultaneously (multi-scale simulations may become important) and comparing measured turbulence characteristics with simulations, since comparing multiple transport channels simultaneously and/or turbulence characteristics adds further constraints to theoretical models and numerical codes. On the other hand, the first level of validation for a particular fusion device also depends on its diagnostic capabilities. For example, for a device without comprehensive transport analysis (which requires a quite complete suite of equilibrium diagnostics to achieve), but with a diagnostic for electron-scale turbulence measurements, one would first try to compare turbulence measurements with global confinement trends. In this section, we will follow different levels of validation and begin with comparing the critical T_e gradient and/or electron thermal transport predicted by ETG theoretical models and numerical codes with experiments. We will then move on to ETG turbulence measurement and compare measured turbulence characteristics (and transport levels if possible) with theoretical models and numerical predictions.

3.1 Validation of ETG-turbulence-driven electron thermal transport

Here, we first take a look at experimental validation of the critical T_e gradient, $(R_0/L_{T_e})_{\mathrm{crit}}$, since there are analytic forms that explicitly parameterize it as a function of equilibrium quantities that are readily available in most major fusion devices. The most convenient form of $(R_0/L_{T_e})_{\mathrm{crit}}$ for the comparison with experiments is Eq. 13 which was obtained using linear gyrokinetic simulations (Jenko 2001). Using the linear critical T_e gradient to compare with experiments only makes sense for the ETG mode when there is no nonlinear upshift in the critical T_e gradient like the so-called Dimits shift for the ITG mode due to turbulence-generated zonal flows (Dimits 2000). As we discussed in Sect. 2.2.3, since zonal flows are weak with positive magnetic shear for ETG turbulence (e.g., the streamer regime of ETG turbulence), the ETG mode is unlikely to have a Dimits-shift-like nonlinear upshift in the critical temperature gradient (note that Eq. 13 is only valid for positive magnetic shears, i.e., $0.2 \leqslant \hat{s} \leqslant 3$). On the other hand, with weak/negative magnetic shear, a nonlinear upshift in the critical T_e gradient is possible, as shown in Peterson (2012) and Peterson (2011) (see Sect. 3.2.2 for more details), which is consistent with the preferential generation of zonal flows with weak/negative magnetic shear seen in the studies of zonal flow dependence on magnetic shear shown in Sect. 2.2.3 (e.g., see Idomura (2005) and Li (2005)). To obtain $(R_0/L_{T_e})_{crit}$ in experiments (if it exists) requires varying ∇T_e with the other equilibrium quantities kept constant to obtain electron heat flux as a function of ∇T_e. If a critical gradient exists, a sharp rise of electron heat flux would be seen when ∇T_e goes beyond this value. To make interpretation easier, a core localized electron heating scheme is preferred, so that the total electron heat flux outside the central heating volume is constant, and thus, electron heating with externally injected electromagnetic waves, e.g., electron cyclotron wave, is usually chosen. Hoang et al. used the fast-wave electron heating (FWEH) experiments to identify the critical ∇T_e on Tore Supra (Hoang 2001). The FWEH on Tore Supra has a localized power deposition within $r/a < 0.2$ and 90% of the power is absorbed by electrons. The injected heating power was varied from 1.5 to 7.5 MW (fast wave + Ohmic heating power). By carefully selecting discharges from an FWEH ^4H_e discharge database to keep density and q nearly constant, the authors indeed found that the dependence of electron heat flux (obtained from power balance analysis) on ∇T_e at each radial location can be fitted with an offset linear function, where the offset in ∇T_e denote the critical ∇T_e (see Fig. 16a). Note that a factor of ten variation in heat flux has been achieved. The extrapolation-determined critical ∇T_e at each radial location is plotted as a function of normalized radius in Fig. 16b. It can be seen that the critical ∇T_e is between 2 and 3 keV/m. The $(R_0/L_{T_e})_{\mathrm{crit}}$ is easily obtained from the critical ∇T_e and compared with Eq. 13 (Jenko and Dorland

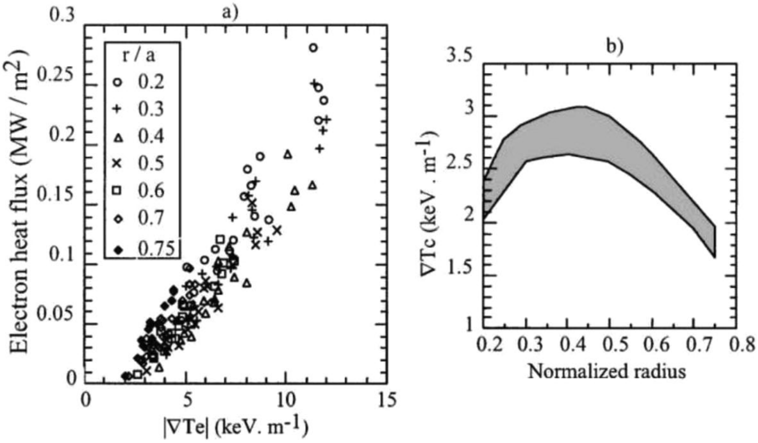

Fig. 16 **a** Electron heat flux as a function of ∇T_e at several different radial locations; **b** critical ∇T_e as a function of the normalized radius with critical ∇T_e obtained from extrapolating data shown in (**a**) for each radial location. Data are from fast wave electron heating (FWEH) plasmas on Tore Supra. The figure is from Fig. 2 in Hoang (2001). Reprinted with permission from Hoang (2001). Copyright (2001) by the American Physical Society

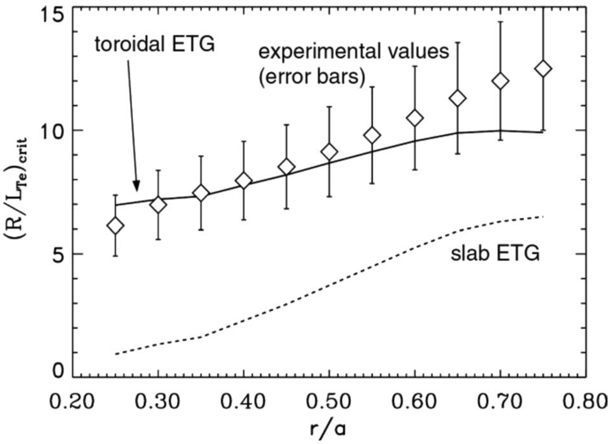

Fig. 17 $(R_0/L_{T_e})_{\rm crit}$ for the toroidal ETG mode compared with experimental determined $(R_0/L_{T_e})_{\rm crit}$ in Tore Supra at different radial locations. A $(R_0/L_{T_e})_{\rm crit}$ profile is also shown for slab ETG mode. Experimental $(R_0/L_{T_e})_{\rm crit}$ is from FWEH plasmas on Tore Supra as described in Hoang 2001. The figure is from Fig. 5 in Jenko and Dorland (2002). Reprinted with permission from Jenko and Dorland (2002). Copyright (2002) by the American Physical Society

2002) (see Fig. 17), where a good agreement with $(R_0/L_{T_e})_{\rm crit}$ of toroidal ETG mode (Eq. 13) for all radial locations can be clearly seen. In comparison, the slab ETG critical gradient (from Hahm and Tang (1989)) severely under-predicts experimental values. The result clearly shows that the ETG mode could produce the correct $(R_0/L_{T_e})_{\rm crit}$ in these experiments in Tore Supra. We note that Hoang (2001) also shows that the electron heat flux is better normalized to a form predicted by the electromagnetic ETG mode (Horton 2000), although a dominant electromagnetic contribution to electron thermal transport is not supported by fluid/gyro-fluid/gyrokinetic simulations (even in higher β STs) (Joiner 2006; Jenko 2000; Labit and Ottaviani 2007; Li and Kishimoto 2004; Colyer 2017; Maeyama 2015)). We note that studies of $(R_0/L_{T_e})_{\rm crit}$ on other tokamaks also show different degrees of consistency with the ETG mode. For example, an analysis of electron cyclotron resonant heating (ECRH) modulation experiment of FTU tokamak shows consistent $\hat{s}/q$ dependence as in Eq. 13 (Jacchia 2002), and another study of $(R_0/L_{T_e})_{\rm crit}$ of ASDEX Upgrade tokamak with ECRH shows that the obtained $(R_0/L_{T_e})_{\rm crit}$ has a better agreement with the ETG mode, while the TEM prediction is a factor of 2–3 higher (Ryter 2001).

Having shown that the ETG mode may be able to explain observed $(R_0/L_{T_e})_{\rm crit}$ on several tokamaks, the next crucial question is whether ETG-mode-driven turbulence could produce the highly anomalous electron thermal transport in fusion devices. The preliminary answer seems to be yes as we have discussed in Sect. 2.2. However, the simulations presented in Sect. 2.2.5 are often based on idealized plasma equilibria with circular magnetic flux surfaces. To make a connection with real experiments, the most logical way to answer this question is to apply numerical simulations with experimental inputs as much as possible and compare the predicted electron thermal transport with that obtained from

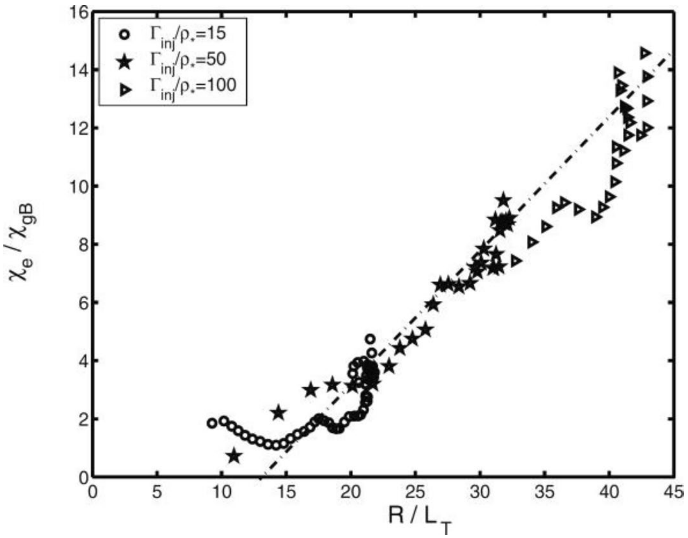

Fig. 18 Normalized electron thermal diffusivity as a function of the normalized electron temperature gradient, R/L_T. Data points are accumulated during the steady-state phase of turbulence for three different injected fluxes. The solid line denotes a linear fit to the data points. The simulation is based on a Tor Supra FWEH plasma. The figure is reprinted from Fig. 4 in Labit and Ottaviani (2007), 2007 © Cambridge University Press, reproduced with permission

transport analysis using experimental measurements. One of the early such simulations was carried out by Labit and Ottaviani (2007), where the authors used a 3D fluid electromagnetic code to simulate a Tore Supra FWEH plasma Hoang (2001). The ETG model is based on Braginskii's fluid equations for electrons including Landau damping closed with adiabatic ions. The global fluid simulation was carried out with fixed injected heat flux and allowed the profile freely respond to the injected flux. Figure 18 shows the normalized electron thermal diffusivity as a function of the normalized electron temperature gradient, R/L_T. A linear fit to the data points leads to a $(R_0/L_{T_e})_{\text{crit}}$ of about 12, which is close to $(R_0/L_{T_e})_{\text{crit}} = 10.5 \pm 2.1$ determined experimentally for this plasma Hoang (2001). However, the simulation-predicted a χ_e that is 45 times smaller than the experimental value, leading the authors to conclude that a fluid treatment of the ETG mode seems not able to reproduce the electron thermal transport in the experiment, and the limitation of a 200 times larger ρ_e^* ($\rho_e^* = \rho_e/a$ is the normalized electron gyroradius) in the simulation than that in the experiment was proposed as one potential explanation of the discrepancy. The difference in global and local simulations may also contribute to the discrepancy. Indeed, using local flux-tube simulations with experimental data yields better agreement with experimental electron thermal transport. Joiner (2006) applied the GS2 gyrokinetic code to an MAST ELMy H-mode plasma in a flux-tube simulation volume at flux surface of $\rho = 0.4$ and 0.8, where ρ is the normalized poloidal flux. As an ST, MAST tokamak has a low aspect ratio, highly shaped plasmas, and higher plasma β than conventional tokamaks (in this case, $\beta = 4.9\%$), which makes the simulation susceptible to numerical convergence issues. Extensive convergence tests have been carried out on simulation domain size and resolution. The authors show that all simulations for $\rho = 0.4$ yield a χ_e of a few m^2/s between 2.36–5.90 m^2/s (taken at the end of simulations) which is experimentally significant as $\chi_e \sim$ 3–8 m^2/s Lloyd (2004) from power balance analysis using the TRANSP transport analysis code Hawryluk (1981). However, simulations for $\rho = 0.8$ yield much lower χ_e than the experiment, showing ETG turbulence may not be responsible for all the electron thermal transport in the edge region in contrast to the core region around $\rho = 0.4$. We note that due to limited computational resources, these simulations are far from reproducing the experiment in terms of adequate resolution and mode coverage, and the comparison with the experiment can only be regarded as qualitative. A more quantitative agreement between experiment and gyrokinetic simulations was shown by Guttenfelder (2013), where electron-scale gyrokinetic simulations of a high-β NSTX H-mode plasma demonstrate a stiff electron thermal transport driven by the ETG mode and the agreement in Q_e is achieved with an increase in a/L_{T_e} within the experimental uncertainty. We note that the ETG mode was also demonstrated to make important contributions to electron thermal transport in NSTX/NSTX-U L-mode plasmas (Kaye 2019; Guttenfelder 2019), where the ETG mode was found to be able to well account for Q_e at mid-radius.

Next, we would like to review some state-of-art validation of multi-scale simulations, which are able to match electron and ion thermal transports simultaneously, substantially improving our understanding of ETG turbulence in driving electron thermal transport. We note that we focus on the physics aspect of multi-scale interaction in Sect. 2. Realizing that single-scale gyrokinetic simulations often fail to explain observed electron thermal transports in experiments (Howard 2013a, b; White 2013) and the importance of a realistic mass ratio in providing the correct multi-scale interaction (see the last section for discussions on the mass ratio issue), Howard et al. carried out massive multi-scale gyrokinetic simulations of Alcator C-MOD L-mode plasmas (Howard 2014, 2015, 2016, 2016). One of these plasmas is a standard low-power [1.2 MW of ion cyclotron resonance Heating (ICRH)] L-mode shot with a core density of about 1.4×10^{20} m^{-3}, a plasma current of 0.8 MA, and a toroidal magnetic field of 5.4 T. Ion-scale and multi-scale simulations were conducted with the GYRO code (Candy and Waltz 2003) with multi-scale simulations having a box size of $32 \times 32\rho_s$, 240 toroidal modes and 1320 radial grid points with resolution of $2\rho_e$ to capture $k_\theta\rho_s$ up to 48 (enough to cover linearly unstable modes). The simulations have all experimental inputs including realistic magnetic geometry [in the form of Miller local equilibrium (Miller 1998)] and kinetic profiles. E×B shear, important for suppressing ion-scale turbulence and potentially influencing ETG turbulence (Guttenfelder and Candy 2011), is also included together with the parallel flow gradient. Three gyrokinetic species are included in simulations with electrons, deuterium ions, and boron impurity, and collisions between electrons and ions are included. Electromagnetic effects are ignored due to the low-beta nature of these plasmas. As we discussed before, in these simulations, there is a distinct scale separation in the electron thermal transport spectrum in ion and electron scales, namely, two prominent peaks in the heat flux spectrum separately in the ion and electron scale. It is seen from these simulations that the ion-scale simulation predicts the ion heat flux well inside the experimental range with the baseline a/L_{T_e} (note that the baseline parameter is located at the center of the shaded square region), while the predicted Q_e is about three times lower than the experimental value (well outside the 1σ range). A 1σ increase in a/L_{T_e} (to the right edge of the shaded region) only barely increases Q_e. Thus, the ion-scale simulations cannot match Q_i and Q_i with the experiment. On the other hand, the multi-scale simulation with the baseline a/L_{T_e} predicts Q_i in line with the experiment (within the 1σ range), but it underpredicts Q_e by about a factor of 2. [The increase of Q_i due to multi-scale interaction is well documented (Maeyama 2015; Howard 2016) and discussed in Sect. 2.2.5.] Increasing a/L_{T_e} by 1σ experimental uncertainty barely changes Q_i, but increases Q_e significantly to the lower edge of the shaded region. This shows that the multi-scale simulation can, within the experimental uncertainty, explain the observed Q_i and Q_e simultaneously, demonstrating the importance of properly treating multi-scale interactions in predicting experimental heat losses. Further scans in a/L_{T_e} also reveal the importance of multi-scale interaction for explaining the T_e profile stiffness. Figure 19 shows Q_i and Q_e from a 4-point a/L_{T_e} scan from -1σ to 2σ with respect to the experimental value. It is clear in Fig. 19a that Q_i has a kind-of U-shaped response to the a/L_{T_e} scan, and there are significant enhancements in Q_i in multi-scale simulation versus ion-scale simulation at three higher a/L_{T_e} except for the lowest a/L_{T_e}, which has to do with the relatively strong ITG drive at the lowest a/L_{T_e} (consistent with the conclusion that a weak ITG drive leads to a stronger ETG turbulence back reaction). The electron profile stiffness can be seen in Fig. 19b, where a 2σ increase in a/L_{T_e} (25%) leads to the doubling of Q_e in multi-scale simulations. It should be noted that while ion-scale simulations show little change in Q_e with the

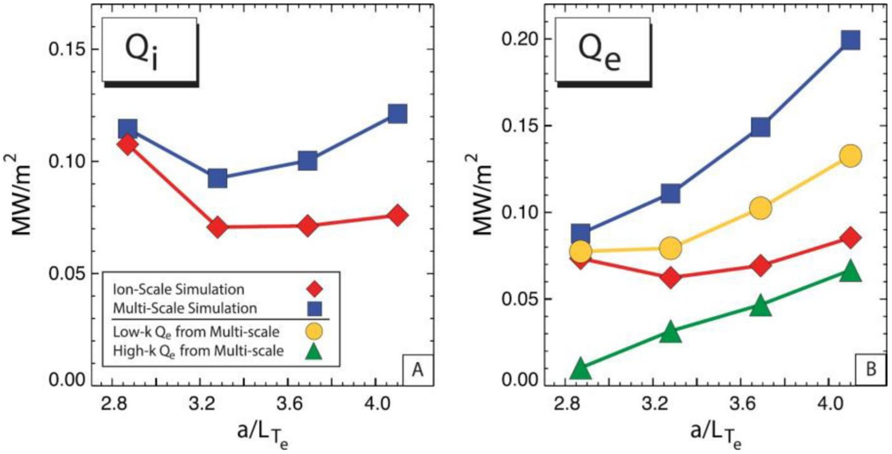

Fig. 19 Ion (A) and electron (B) heat fluxes as a function of a/L_{T_e} for ion-scale simulation (red diamond) and multi-scale simulation (blue square). The low-k contribution to Q_e (yellow circle) and high-k contribution to Q_e (green triangle) are also shown. a/L_{T_e} is scanned at -1σ, o, 1σ and 2σ difference from the experimental value. These local simulations were performed with the GYRO code for a low-power Alcator C-Mod L-Mode plasma with local parameters at $r/a = 0.6$. The figure is from Fig. 3 in Howard (2016). Reprinted from Howard (2016), with the permission of AIP Publishing

a/L_{T_e} scan, the increase in Q_e in the multi-scale simulations mainly comes from the high-k contribution in the lower a/L_{T_e} range (i.e., a/L_{T_e} from about 2.8 to3.3) and a larger contribution from low-k fluctuations is seen as a/L_{T_e} increases from about 3.3 to 4.2, showing that single scale alone (either high-k or low-k) would not be able to correctly predict the T_e profile stiffness. To expand the parametric space for validating multi-scale interactions, a multi-scale simulation was carried out for a high-power C-MOD L-mode plasma for which an ion-scale simulation was found to be adequate to explain both Q_i and Q_e. As seen in Fig. 20, the multi-scale simulation significantly overpredicts Q_i, while the predicted Q_e is within the experimental uncertainty. A multi-scale simulation with a 3% decreased a/L_{T_i} indicates that the ITG mode is stable, while Q_e is not significantly affected. Thus, the authors conclude that due to the extreme stiffness in ion thermal transport, a smaller decrease (less than 3%) would be able to match Q_i with the experiment. We note that validation of multi-scale interaction is an effort being carried out for other fusion devices as well and is not without complications. Holland (2017) show that outcomes of their multi-scale simulations of a well-established DIII-D ITER baseline discharge are very sensitive to experimental parameters within experimental uncertainties. Particularly, the equilibrium E×B shear can either suppress or enhance ion-scale turbulence and transport in multi-scale simulations with respect to ion-scale simulations. In fact, a complete suppression of ion-scale turbulence with experimental E×B shearing rate in the multi-scale simulation is observed with the corresponding ion-scale simulation showing comparable ion thermal transport as in the experiment (see Fig. 21). Thus, we can see that although there have been great improvements in understanding and simulating ETG turbulence and some successful comparisons with experiments, such agreement is still limited, and understanding the reason underlying the observed discrepancies, e.g., the parametric limitation for a particular ETG model,

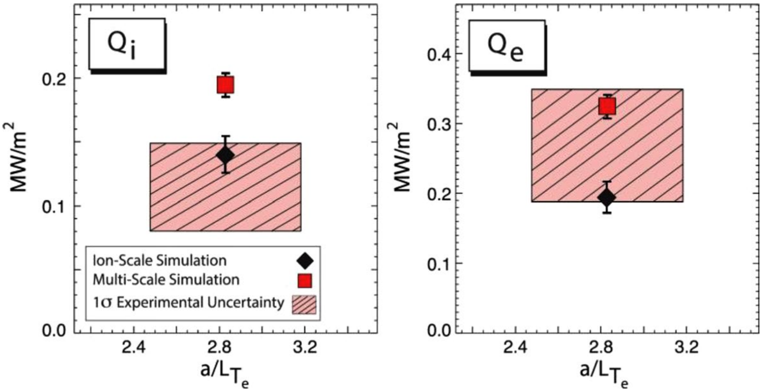

Fig. 20 Ion (left) and electron (right) heat fluxes for ion-scale simulation (black diamond) and multi-scale simulation (red square). The experiment heat flux is also shown (the square-shaded region with the half height representing 1σ experimental uncertainty in heat flux and the half width representing 1σ experimental uncertainty in a/L_{T_e}). These local simulations were performed with the GYRO code for a high-power Alcator C-Mod L-Mode plasma with local parameters at $r/a = 0.6$. The figure is from Fig. 9 in Howard (2016). Reprinted from Howard (2016), with the permission of AIP Publishing

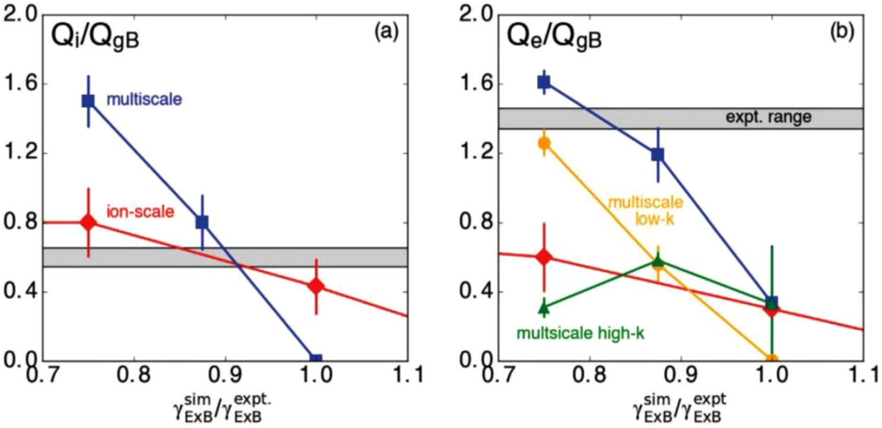

Fig. 21 Normalized ion (**a**) and electron (**b**) heat fluxes for ion-scale simulation (red diamond) and multi-scale simulation (blue square) as a function of the ratio between simulation E×B shearing rate and experimental E×B shearing rate. The experiment heat flux range is also shown as shaded regions. These local simulations were performed with the GYRO code for a DIII-D ITER baseline plasma with local parameters at $\rho_{\mathrm{tor}} = 0.65$, where $\rho_{texttor}$ is the square root of normalized toroidal flux. The figure is reprinted from Fig. 8 in Holland (2017), with the permission of International Atomic Energy Agency

is still incomplete. Gyrokinetic studies coupled with turbulence measurements may be able to improve our understanding of electron-scale turbulence and provide the next level of model validation. We will review advances in this line of approach in the next section.

3.2 Studying the ETG mode with electron-scale measurements

As we have discussed, electron-scale turbulence measurement in the electron scale would provide more strict constraints to the validation of ETG theoretical models and numerical codes in addition to comparing the predicted critical T_e gradient and/or electron thermal transport with experiments. Measuring electron-scale turbulence is quite challenging because of the small electron-gyroradius scale of the ETG mode. For example, if we take $T_e = 2$ keV and $B = 2$ T for a typical conventional tokamak, $\rho_e \approx 50\ \mu m$. If we would like to resolve an ETG wavenumber, say $k_\perp \rho_e = 0.2$, the corresponding $k_\perp \approx 37.6\ \mathrm{cm}^{-1}$ and $\lambda \approx 1.7$ mm, which requires a spatial resolution that is very challenging for any imaging-based diagnostic if not impossible. On the other hand, coherent scattering of electromagnetic waves by electron density fluctuations is probably the best choice for such a measurement due to the fact that the scattered wave power is proportional to the wavenumber spectral power of electron density fluctuations (one can think of the scattering process as a spatial Fourier analysis of electron density fluctuations in the scattering volume coupled with probe and scattered beam profiles). The wavenumber and corresponding frequency of electron density fluctuations measured by a scattering diagnostic are determined by the Bragg condition, namely $\vec{k}_t = \vec{k}_s - \vec{k}_p$ and $\omega_t = \omega_s - \omega_p$ where subscripts ‘t’, 's', and 'p' denote 'turbulence', 'scattered beam', and 'probe beam'. In other words, the measured turbulence wavenumber is determined by the angle between the scattered beam and the probe beam, and the corresponding frequency is determined by the frequency shift between the scattered beam and the probe beam. From the point view of spatial Fourier analysis, one can readily deduce that the wavenumber resolution of a scattering diagnostic is inversely related to the scattering volume, and from the Bragg condition, the upper range of the wavenumber coverage is physically limited by the largest scattering angle receivable by the receiving optics. We note that given the same scattering angle, low B_T STs have the advantage of measuring larger normalized wavenumbers (normalized to $1/\rho$) compared to the conventional tokamaks due to the larger ρ from the lower B_T. The lower range of the wavenumber coverage is limited by the probe beam divergence, so that the scattered beam and probe beam do not overlap. As a side note, there are scattering diagnostics that measure the collective scattering within the divergence of the probe beam, and such a scattering scheme is called far forward scattering (Evans 1982, 1983) which is suitable for measuring long-wavelength instabilities.

Two major types of coherent scattering schemes commonly considered for electron-scale turbulence measurement are forward scattering (Mazzucato 1978; Slusher and Surko 1980) and back scattering (Novik and Piliya 1994; Holzhauer 1998; Hirsch 2001; Gusakov 2006; Rhodes 2007; Hillesheim 2015). Back scattering relies on O-mode or X-mode cutoffs/resonances in the plasma to make localized measurement and to select measured wavenumbers [e.g., using enhanced scattering at upper hybrid resonance (Novik and Piliya 1994; Gusakov 2006), and Doppler back scattering based on cutoffs (Hillesheim 2015)] or to eliminate unwanted stray light (Rhodes 2007), because of which the scattering location depends on the plasma density profile and magnetic geometry. Unitizing cutoffs/resonances, the back scattering schemes can provide excellent spatial localization. Forward scattering, with a probe beam frequency much higher than major resonant and cut-off frequencies in the plasma, is largely independent of plasma profiles (despite some minor refraction probe and scattered beams may experience if the probe beam frequency is not high enough), and if the frequency is high enough, probe and scattered beams basically propagate quasi-optically and, to the lower order, in straight lines.

Forward scattering can be configured to have small scattering angles (e.g., using high-frequency sources like CO_2 laser) to minimize the size requirement of access windows, and on the other hand, this configuration leads to the overlap of scattered beams and the probe beam throughout the entire plasma, which is non-ideal for achieving good spatial resolutions. Forward scattering can also be achieved with large scattering angles (e.g., using lower frequency microwave and FIR) with a better spatial resolution due to less overlap of scattered beams and the probe beam, but, however, it requires a much larger access window to collect the scattered light. Magnetic geometry plays an important role in determining the scattering location and scattering volume for forward scattering due to the drift wave characteristic $k_{||} \ll k_\perp$, i.e., $\vec{k}_t \cdot \vec{B} \approx 0$, which $\vec{k}_t = \vec{k}_s - \vec{k}_p$ has to satisfy. This $\vec{k}_t \cdot \vec{B} \approx 0$ condition is particularly effective in improving forward scattering configuration when the probe beam is launched tangentially with respect to the magnetic field, leading to a significantly reduced scattering volume (and thus better spatial resolution) than that determined simply by the overlap between the scattered and probe beams (Mazzucato 2003). As a result, small angle forward scattering systems, previously thought as having only line-averaged measurements, would have a finite spatial resolution due to a tangential scattering configuration, e.g., the systems on EAST tokamak (Sun 2017) and HL-2A tokamak (Yao 2020). To understand this effect physically, let us take a look at a limiting case where the probe beam is exactly parallel to the equilibrium magnetic field, and it is easy to see that no turbulence wavenumber, $\vec{k}_t = \vec{k}_s - \vec{k}_p$ with $|\vec{k}_s| \approx |\vec{k}_p|$, can satisfy the drift wave condition $\vec{k} \cdot \vec{B} \approx 0$, since $\vec{k}_p = k_p\vec{B}/B$. In other words, the scattering volume for such a limiting case would be zero, although the overlap volume between a scattered beam and the probe beam remains finite. If the angle between $\vec{k}_p$ and $\vec{B}$ becomes finite, the scattering volume would become finite as well but much less than the simple overlap volume between the scattered and probe beams. Thus, the anisotropy of drift wave with respect to the equilibrium magnetic field would give a constraint on the scattering volume and can improve the spatial localization for the forward scattering scheme (Mazzucato 2003).

3.2.1 Recent turbulence diagnostics resolving electron scales

As we have discussed above, resolving electron-scale turbulence has to rely on the scattering of electromagnetic waves in one way or another, and two common schemes being used on fusion devices are back scattering and forward scattering. There are several recent high-k back scattering diagnostics installed on tokamaks, e.g., FT-2 (Gusakov 2006), DIII-D (Rhodes 2007) and MAST (Hillesheim 2015). The forward scattering scheme, given all the advantages, has fewer implementations due to the limitation in spatial resolution (small angle forward scattering) and the large space requirement for collecting scattered light (large angle forward scattering). The former has implementations on EAST (Sun 2017) and HL-2A (Yao 2020), and the typical examples of the latter are a 280 GHz microwave scattering system measuring high-k_r installed on NSTX (Smith 2008) and a 693 GHz Far Infrared (FIR) high-k_θ scattering system to be installed on NSTX-Upgrade (Barchfeld 2018). Since reviewing all electron-scale-turbulence-capable scattering diagnostics is beyond the scope of this paper, we will just introduce some of them as they have provided measurements of the electron-scale turbulence in tokamaks.

One coherent back scattering diagnostic, relying on enhanced scattering (ES) around upper hybrid resonance (UHR) surface (Novik and Piliya 1994), was installed on the FT-2 tokamak. For such a scattering scheme, the launched probe beam wavenumber is much smaller than the wavenumber it aims to measure, and it is close to the UHR location where the probe beam amplitude and wavenumber are significantly increased due to the UHR resonance, and thus enhanced back scattering at a fluctuation wavenumber, k_t, occurs when $2k_i(x_s) = -k_t$, where x_s denotes the scattering location and is a function of the probe beam frequency, ω_i. The total scattered power can be written as $p_s(\Omega) = P_i r_e^2 n_e (\omega/\omega_{pe})^4/(\pi^2 k_0^4) \int \rho(\vec{k}_t) S(\vec{k}_t, \Omega) \mathrm{d}\vec{k}_t$, where P_i is the probe beam power, $r_e = e^2/m_e c^2$ is the classical electron radius, $k_0 = \omega/c$ (ω is the probe beam frequency), $\rho(\vec{k}_t)$ is a weight-function that includes the scattering enhancement due to the UHR, and $S(\vec{k}_t,\Omega) = |n|^2_{\vec{k}_t,\Omega}$ is the usual fluctuation spectral density of the plasma density fluctuations. This expression is very similar to that of general coherent scattering but includes an extra term, i.e., the scattering enhancement function, $\rho(\vec{k}_t)$. It is found that in a 1D problem with the probe beam in the x direction, the ES spectrum, i.e., the density fluctuation spectrum weighted by the antenna diagram $(F(\vec{k}_t))$ and scattering enhancement function($S_{ES}(k_{t,x})$), $I(k_{t,x},\Omega) = \int |F|^2|n|^2_{\vec{k}_t,\Omega} S_{ES}(k_{t,x})\mathrm{d}k_{t,y}\mathrm{d}k_{t,z}$, can be reconstructed from the cross-correlation spectrum of the scattering signals from two probe beams with slightly different frequencies (scattered at two nearby UHR surfaces). Figure 22a shows a schematic of the diagnostic implemented on FT-2, where two probe beams of frequencies f_1, $f_2 = f_1 + \zeta$ (ζ is a small frequency shift) are injected into the plasma with the same antenna, and the scattered waves are collected by an adjacent antenna. Two stages of mixing are used to separate scattering signals from the two UHR surfaces, and a scan in ζ from – 400 to 400 MHz provides the cross-correlation function $\mathrm{CCF}(\zeta,\Omega)$ which is then Fourier transformed to obtain the ES spectrum $I(k_{t,r},\Omega) = \int \mathrm{CCF}(\zeta,\Omega)\exp(-ik_{t,r}\zeta\partial x_{UH}/\partial f\mathrm{d}\zeta)$. Here, $\Delta x_{UH} = \zeta\partial x_{UH}/\partial f$ and Δx_{UH} is the UHR spatial separation (here we use (r,θ) coordinate). To obtain $|n|^2_{k_{t,r},\Omega}$ from $I(k_{t,r},\Omega)$ (note that $I(k_{t,r},\Omega)$ is an integral of $|n|^2_{k_{t,r},\Omega}$, $I(k_{t,r},\Omega)$ is fitted to an expression of $|n|^2_{k_{t,r},k_{t,\theta},\Omega} = |n|^2_{k_{t,r},k_{t,\theta}}\exp(-(k_{t,\theta}-\Omega/V_\theta)^2(\Delta k_{t,\theta})^2)\sqrt{\pi}/\Delta k_{t,\theta}$ from the nonlinear broadening of the turbulence spectrum, where V_θ and $\Delta k_{t,\theta}$ are fitting parameters

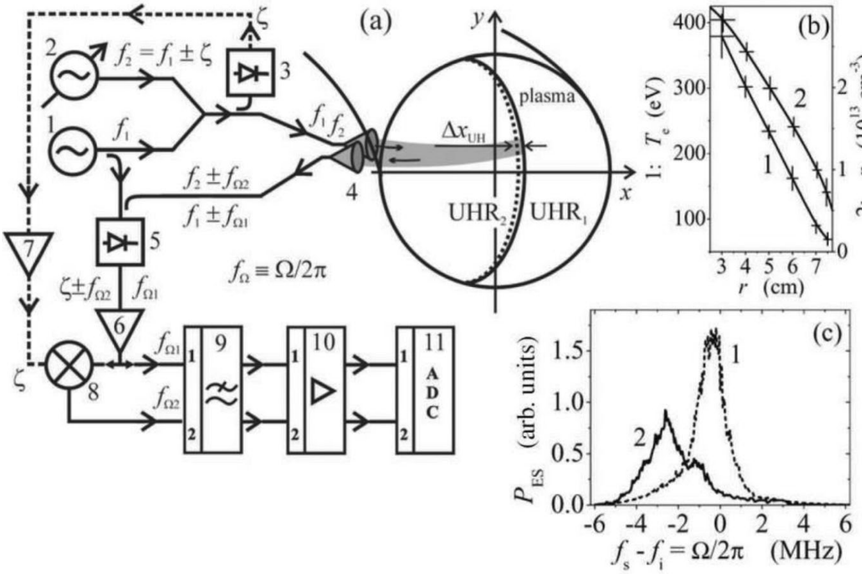

Fig. 22 **a** A schematic of the enhanced scattering (ES) system on FT-2 tokamak with asymmetric correlation scheme; **b** typical T_e (1) and n_e (2) profiles of a 32 kA FT-2 plasma; **c** ES frequency spectra for f_i = 61.9 GHz (1) and f_i = 65.8 GHz (2). The figure is reprinted from Fig. 1 in Gusakov (2006). © IOP Publishing. Reproduced with permission. All rights reserved

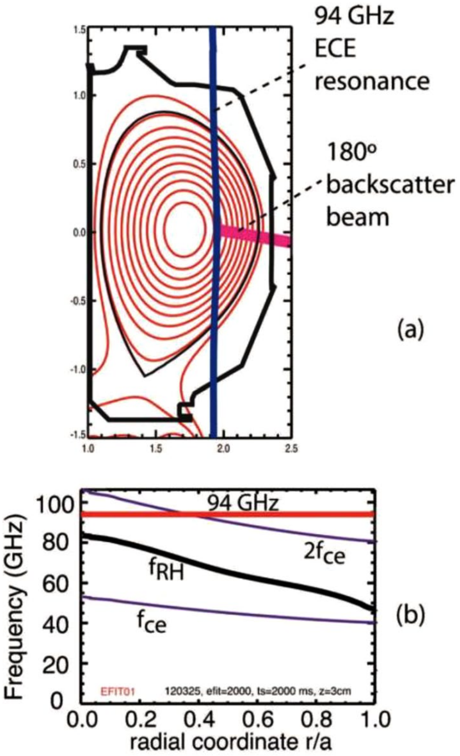

Fig. 23 **a** Scattering scheme with the 94 GHz 2nd harmonic ECR surface and magnetic flux surfaces for a typical DIII-D plasma; **b** radial profiles of cutoffs, the 2nd harmonic ECR, and the 94 GHz back scattering frequency. The figure is from Fig. 3 in Rhodes (2006). Reprinted from Rhodes (2006), with the permission of AIP Publishing

(Gusakov 2006). Note that f_i can be varied from 52 to 69 GHz, allowing radial scans of scattering location. With typical T_e and n_e profiles of a 32 kA FT-2 plasma (see Fig. 22b), ES frequency spectra with $f_i = 61.9$ GHz (curve 1) and $f_i = 65.8$ GHz (curve 2) are shown in Fig. 22c, where curve 1, observed in the plasma edge at 6 cm $< r <$7.9 cm, is more symmetric, and is of a larger amplitude with a smaller Doppler shift of 0.2−0.5 MHz, while curve 2, observed in the core region 4 cm$< r <$6 cm, has a large Doppler shift (1.5–3 MHz) in the electron diamagnetic direction with smaller amplitude.

A 94 GHz X-mode high-k back scattering system was installed on DIII-D tokamak (Rhodes 2006) to measure electron-scale turbulence (e.g., $k_\perp \sim 35$–40 cm^{-1} and $k_\perp \rho_s \sim 4$–10, which is in the ETG mode wavenumber region). Note that the precise range of measured fluctuation wavenumber is determined by realized plasma equilibrium, since the plasma refraction index would reduce the probe beam wavenumber and controls the lower range of measurable $k_\perp$. This back scattering system relies on the 2nd harmonic ECR to absorb the probe beam and any forwardly scattered light (see Fig. 23). Due to its almost radially injected scheme, the scattering system measures mostly radial wavenumbers with a small poloidal component, e.g., $k_r \approx 34.95-$ cm^{-1} and $k_\theta \approx \pm 0.2$ cm^{-1}. It is easy to see that the probe beam and scattered beams essentially overlap throughout the plasma, leading to a scattering volume from the plasma edge to the location of the ECR surface. A later hardware

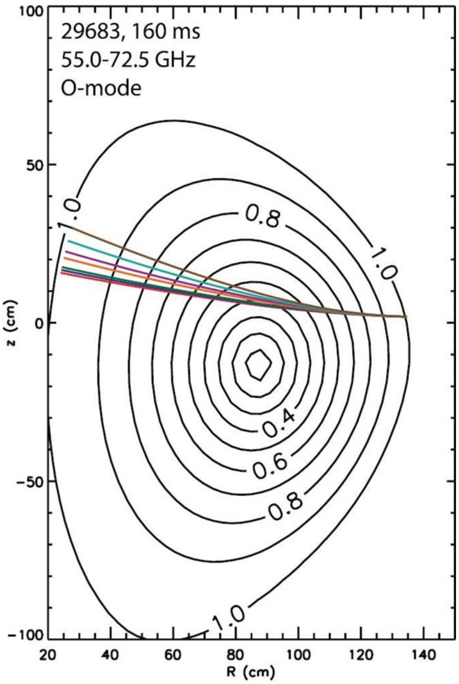

Fig. 24 Ray tracing of 55.0 to 72.5 GHz O-mode channels for high-k measurements is shown together with contours of magnetic flux surfaces with the square root of the normalized poloidal flux. The poloidal launch angle here is 1° and the toroidal launch angle is 2°. The figure is reprinted from Fig. 17 in Hillesheim (2015), with the permission of International Atomic Energy Agency

upgrade (Rhodes 2007a) allows some spatial resolution to the high-k measurement by adding a second receiving antenna at about 12° with respect to the 94 GHz probe beam measuring nearly the same perpendicular wavenumber as the original configuration above. With a vertical movement, this second receiving antenna can be aimed at $\rho \sim 1$, 0.6, and 0.35 with a radial resolution of ±10 cm.

A Doppler back scattering (DBS) system on MAST spherical tokamak was designed to make electron-scale turbulence measurements with $7 \lesssim k_\perp \rho_i \lesssim 11$ (Hillesheim 2015). A 2D steering mechanism was implemented to achieve wavenumber matching in the presence of a large variation in magnetic pitch angle in MAST (as for all STs). The high-k measurements are realized by launching V-band, O-mode probe beams (55–72.5 GHz) into the plasma with minor deflection due to refraction (see Fig. 24). In contrast to the typical DBS scheme where the probe beams get reflected at the cut-off surface, the probe beams here do not reach the cut-off surface, and minimum wavenumber, k_p, reached at $\sqrt{\psi} \approx 0.4$ is only a factor of 0.6–0.8 of the vacuum wavenumber. Thus, the scattering scheme is similar to the normal back scattering as the DIII-D backs scattering system discussed above, and the scattered light may come from anywhere along the probe beam path. However, with a large magnetic pitch angle variation along the probe beam path, the matching requirement for drift waves, $k_{||} \ll k_\perp$, may provide spatial localization to the back scattering, and this was actually confirmed with experimental observations (Hillesheim 2015) and a more recent modeling (Hall-Chen 2022).

A high-k microwave collective (large angle forward) scattering system (the high-k scattering system) (Smith 2008) (see Fig. 25a for the hardware arrangement and

Fig. 25b for a schematic of the scattering configuration) was installed on NSTX to study electron-scale turbulence. A probe microwave beam of 280 GHz is injected tangentially into the plasma. Due to this tangential scattering scheme, the scattering system measures mostly the local k_r component of plasma turbulence with a radial spatial resolution of ±2 cm (note that $a \sim 60$ cm), which allows the studies of the parametric dependence of electron-scale turbulence on local equilibrium quantities. Five individual receiving channels aiming at different scattering angles with heterodyne receivers allow the measurement of scattering power and frequency shift at most five different wavenumbers, from which one is able to reconstruct the wavenumber spectra of plasma turbulence, i.e., five data points along a line in the 2D plane of the k_r and k_θ wavenumber spectrum, and to determine the propagation direction of each wavenumber component, i.e., in the electron or ion drift direction. It is important to note that although the dominant spectral components of ETG turbulence, i.e., the modes with large k_θ and small k_r (see Ref. Guttenfelder and Candy (2011)), are not measured by the high-k scattering system, the assumption is that the measured spectral power at experimentally realized wavenumbers, i.e., large k_r and small k_θ, is positively correlated with that of the most dominant spectral component, and we found that nonlinear ETG simulations, like the ones in Guttenfelder and Candy (2011) and Ren (2012), support this assumption.

A new 693 GHz FIR scattering system measuring k_θ spectrum was designed and will be installed on NSTX-U (Barchfeld 2018). The 693 GHz FIR probe beam generated by a formic acid FIR laser with a >80 mW output power is to be launched with a remotely steerable mirror from Bay G of NSTX-U, and the scattered light,

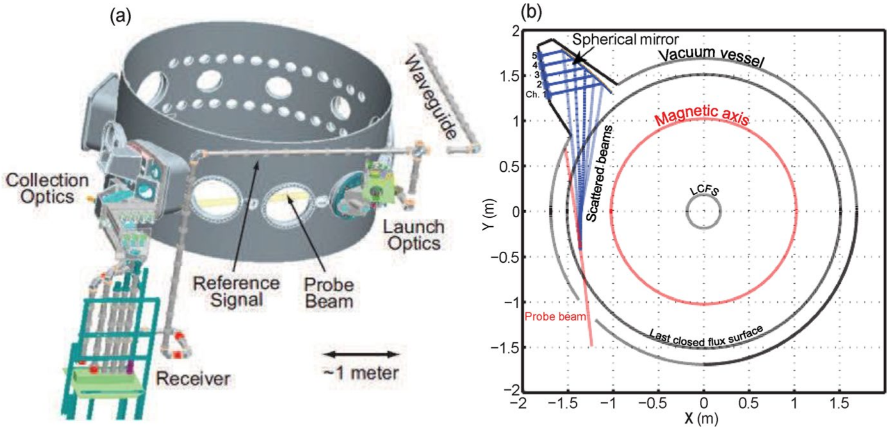

Fig. 25 **a** Arrangement of the NSTX collective scattering system; **b** schematic of the scattering configuration of the high-k scattering system for an NSTX L-mode plasma. The probe beam and scattered beam trajectories are calculated using a ray-tracing code. The scattered light is reflected and focused by a spherical mirror onto five collection windows. Figure 25a is adapted from Fig. 1 in Ref. (Smith 2008); Reprinted from Ref. (Smith 2008), with the permission of AIP Publishing. Fig. 25b is adapted from Fig. 1 in Ref. (Ren 2013) with the permission of International Atomic Energy Agency

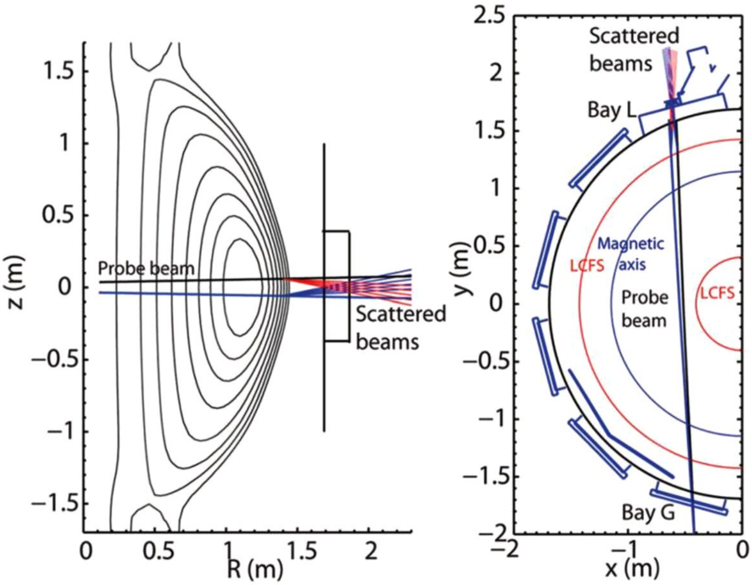

Fig. 26 (Left) side and (right) top view illustrations of the two poloidal scattering schemes (upward and downward scattering) on NSTX-U. The figure is from Fig. 1 in Ref. (Barchfeld 2018). Reprinted from Ref. (Barchfeld 2018), with the permission of AIP Publishing

after going through a rectangular vacuum window and high-density polyethylene (HDPE) lenses, is to be collected by a five-axis (X, Y, Z, poloidal, and toroidal) receiver carriage. A 4-channel element subharmonic mixer (SHM) array is to be used to detect scattered light. Compared with the high-k scattering system for NSTX, the NSTX-U high-k scattering system has a probe beam that is more perpendicular to flux surfaces (see the left panel of Fig. 26) and thus measures the spectral power of wavenumber vectors with $k_\theta > k_r$. The scattering scheme is designed to accommodate two scattering configurations, one with scattered beams going upward (scattered beams in blue in Fig. 26) and the other with scattered beams going downward (scattered beams in red in Fig. 26), allowing measurements of two different portions of the 2D (k_θ, k_r) wavenumber space with different k_θ/k_r ratios. The characteristic anisotropy of ETG turbulence streamers, i.e., peak spectral power with large k_θ and small k_r (Guttenfelder and Candy 2011), should be detectable by comparing the wavenumber spectra measured by the two scattering schemes. Note that a poloidal wavenumber >40 cm^{-1} is achievable with the present design.

3.2.2 Identifying ETG turbulence with electron-scale turbulence measurements

Here, we would like to present experimental evidence of the existence of ETG turbulence and its role in driving electron thermal transport in several tokamaks. Coupled with theories of the ETG mode and linear and nonlinear gyrokinetic simulations, the best evidence comes from electron-scale turbulence measurements. To

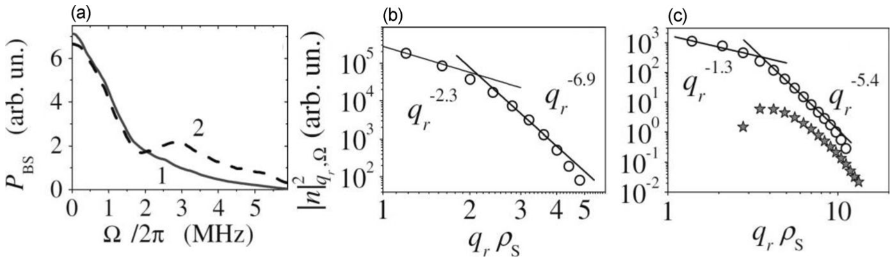

Fig. 27 **a** UHR ES homodyne spectra for discharges with $I_p = 22$ kA (solid line) at R=61.2 cm and I_p =32 kA (dashed line) at R=62.3 cm; **b** the radial wavenumber spectrum of density fluctuation at R=61.2 cm for the $I_p = 22$ kA discharge; **c** radial wavenumber spectra of density fluctuation R=62.3 cm for the $I_p = 32$ kA discharge from the lower frequency peak in (**a**) (open circle) and from the higher frequency spectral peak in (**a**) (filled star). Note that results were obtained in ohmic FT-2 plasmas with $R_0 = 55$ cm, $a = 8$ cm, and $B_T \approx 2.2$ T. Typical central parameters for ohmic hydrogen plasmas are: $T_e(0) \approx 500$ eV, $T_i(0) \approx 120$ eV, and $n_e(0) < 5 \times 10^{13}\, cm^{-3}$. The figure is adapted from Fig. 3a, d, and h in Ref. (Gusakov 2006). © IOP Publishing. Reproduced with permission. All rights reserved

compare experiments and simulations, an absolute comparison is usually preferred, e.g., the standard heat flux matching. However, since absolute calibration of scattering diagnostics is usually not available, it is impossible to compare absolute density fluctuation levels between scattering diagnostic measurements and predictions from numerical simulations. Practically, one often finds it much easier to compare relative changes in measured fluctuation level, as experimental parameters are varied, with corresponding predictions from analytical theories, linear and nonlinear gyrokinetic simulations, and with corresponding variations in experimentally determined transports. Particularly, an instability is best characterized by its parametric dependence, e.g., Eq.13 for the linear threshold of the ETG mode, and thus, experimental studies of parametric dependence of the measured turbulence would be quite revealing. Beyond the comparison of fluctuation levels, comparing turbulence wavenumber and/or frequency spectra with those from numerical simulations would provide even more convincing evidence of the existence of an instability. We note that this usually requires the development of a synthetic diagnostic for a particular turbulence diagnostic, a trend well undergoing for present and future turbulence and transport studies.

In experiments, any experimental control that can induce macroscopic changes in plasma equilibrium may be used to study the corresponding changes in the underlying electron-scale turbulence. However, without sophisticated experimental controls, many parameters could be varied simultaneously, which is not optimal for the study of parametric dependence. On the other hand, they still could provide useful information. One of the earliest observations of high-k ETG-driven instability was made on the FT-2 tokamak (Gusakov 2006). In a 22 kA hydrogen discharge of FT-2, a diagnostic injection of helium gas leads to a T_e profile flattening at the edge, i.e., $\eta_e = L_{n_e}/L_{T_e} < 0.8$ at $r > 6$ cm ($R > 61$ cm) which makes the ETG mode stable (see Eq. 13 that $\eta_e = L_{n_e}/L_{T_e} < 0.8$ is a sufficient condition for stabilizing the ETG mode). In Fig. 27a, the corresponding UHR ES homodyne frequency spectrum measured at R=61.2 cm is compared with that of a 32 kA discharge measured

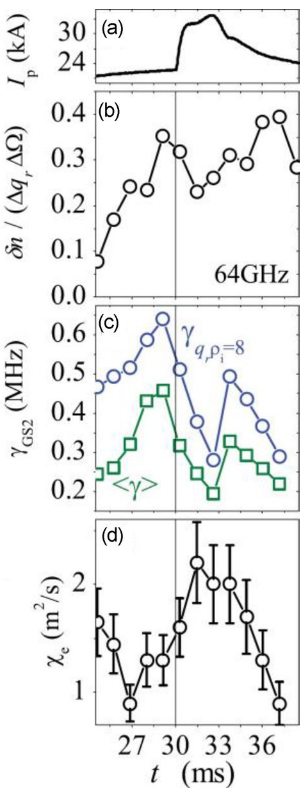

Fig. 28 Temporal evolution of **a** Plasma current, **b** density fluctuation integrated over the HF spectral branch, **c** linear growth, γ, for $q_r\rho_i = 8$ (open circle) and averaged linear growth, $<\gamma>$, over $0.1 < q_r\rho_i < 10$ (open square) from GS2 calculation, and **d** electron thermal diffusivity from the experiment. Note that measurements were taken in an ohmic FT-2 plasma with dynamic current ramp-up (CRU). The figure is adapted from Fig. 2h–k in Ref. (Gurchenko and Gusakov 2010). © IOP Publishing. Reproduced with permission. All rights reserved

at R=62.3 cm where $\eta_e = L_{n_e}/L_{T_e} > 0.8$ (necessary for the ETG mode to be unstable). It is noticeable that the ES frequency spectrum for the $I_p = 22$ kA discharge is monotonic and has one spectral peak around zero frequency with a 1.2 MHz half width at half amplitude, while the ES frequency spectrum for the $I_p = 32$ kA discharge has two spectral peaks with the lower frequency one similar to that of the $I_p = 22$ kA discharge and the other higher frequency one having a spectral peak at about 3 MHz. The generation of a second peak in the ES frequency spectrum indicates that two different drift waves are present in the $I_p = 32$ kA discharge with a higher η_e than the $I_p = 2$ kA discharge, indicating that the ETG mode may be unstable due to the higher η_e and responsible for the observed second spectral peak. The cross-correlation inversion method introduced for the FT-2 UHR ES diagnostic was used to obtain q_r (we use q_r instead of k_r following Fig. 27b and c) spectra for both discharges, where the q_r spectra derived from low-frequency (LF) peaks in Fig. 27a can be fitted with two power laws for both discharges with larger exponents for the $I_p = 22$ kA discharge. We note that forming power laws in the wavenumber spectrum is usually the result of some sort of energy cascade in the wavenumber space. It is also obvious in Fig. 27b and c that the q_r spectra for the $I_p = 32$ kA discharge extend to higher wavenumbers than the $I_p = 22$ kA discharge and have a lower-power spectral branch derived from the high-frequency (HF) spectral peak shown in Fig. 27a, presumably due to the existence of a different drift wave. This

HF spectrum is not monotonic in q_r and has a spectral peak at about $q_r\rho_s = 4.2$, potentially consistent with recent FT-2 simulations where the maximum ETG linear growth is achieved with finite q_r's (Janhunen 2021). This combined with the fact that the existence of this HF mode is correlated with larger η_e (> 0.8) gives a strong indication that this HF spectral peak is due to the ETG mode. Current-ramp-up (CRU) experiments on FT-2 provide another piece of evidence of the ETG mode, as shown in Fig. 28 (Gurchenko and Gusakov 2010), where the plasma current is quickly ramped up from 22 to 32 kA (see Fig. 28a). This current ramp-up leads to plasma profile changes (not limited to the T_e profile), modifying the resulting turbulence. The integrated density fluctuation over the HF branch (presumably due to the ETG mode) is seen to decrease in response to the current ramp-up (see Fig. 28 (b)), in correlation with a decrease in the ETG linear growth rate calculated with the GS2 code (see Fig. 28c). Figure 28b and c shows that the integrated density fluctuation level correlates with the calculated ETG mode linear growth rates during the whole time period, supporting the existence of the ETG mode in the plasma. However, the correlation with the experimentally determined χ_e is not obvious (see Fig. 28b and d), questioning the relevance of the observed turbulence to driving electron thermal transport in this plasma.

We note that the experiments mentioned above are not well targeted at electron-scale turbulence. Particularly, the experimental methods used to modify the T_e gradient may induce additional equilibrium changes. Next, we would like to review some more targeted experiments for studying electron-scale turbulence and electron thermal transport through electron heating.

Response of electron-scale turbulence to electron heating: Effects of electron heating are of twofold. One is to modify the T_e gradient, since the T_e gradient drives the ETG mode, and the other is to increase electron heat flux, so that the responsible

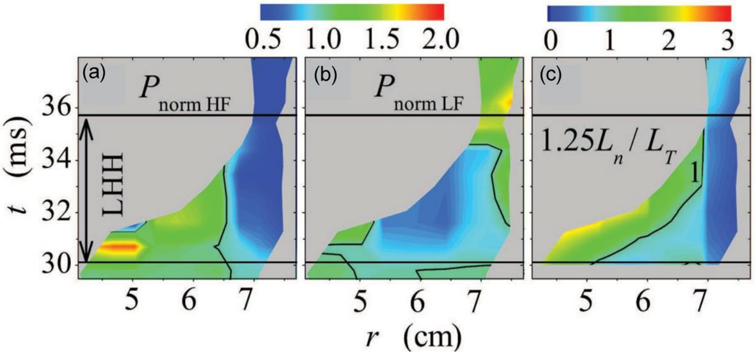

Fig. 29 Normalized integrated power of the HF (**a**) and LF (**b**) spectral components in the UHR ES power frequency spectrum (normalized to their respective value at t=29 ms) as a function of time and minor radius. The normalized η_e, $1.25L_n/L_T$, **c** as a function of time and minor radius. Note that $1.25L_n/L_T < 1$ is a sufficient condition for the ETG mode to be stable. The duration of the lower hybrid heating (LHH) is in between the two horizontal solid lines in each panel. The LHH experiments were carried out in ohmic FT-2 plasmas with $R_0 = 55$ cm, $a = 7.9$ cm, $B_T \approx 2.2$ T, and $I_p = 32$ kA. The figure is adapted from Fig. 2e, f, and g in Ref. (Gurchenko and Gusakov 2010). © IOP Publishing. Reproduced with permission. All rights reserved

turbulence has to react to the additional electron heating. Electromagnetic waves are usually used in electron heating experiments, e.g., ECRH for the T_e gradient modification in many conventional tokamaks, since they have less complicated effects on plasmas (Ryter 2001a, 2001, 2001b; Jacchia 2002; Ryter 2005, 2006; Gentle 2006; Rhodes 2007a, b; DeBoo 2010, 2012; Schmitz 2012; Smith 2015). On the other hand, neutral beam injection (NBI) heating usually not only heats plasma but also does fueling and acceleration of plasmas, etc. We note that significant modification of the T_e gradient by adding electron heating may not be feasible if the T_e profile is stiff. However, the response of electron-scale turbulence to the additional electron heat flux should be noticeable if electron-scale turbulence is responsible for driving electron thermal transport.

The lower hybrid heating (LHH) experiments on FT-2 provide an example of how electron-scale turbulence reacts to electron heating (Gurchenko 2007). Note that the LHH on FT-2 heats both electrons and ions. Figure 29a and b shows the spatial and temporal evolution of the normalized integrated (over frequency, Ω) power

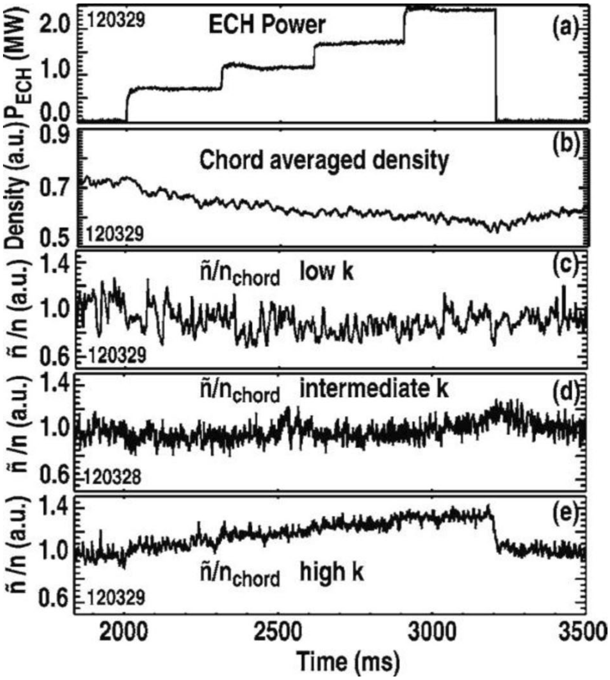

Fig. 30 Response of normalized plasma density fluctuation level, $\tilde{n}/n_{\mathrm{chord}}$ ($\tilde{n}$ being the RMS of the density fluctuation and n_{chord} being the chord-averaged electron density), to the stepping-up of ECH or ECRH power. **a** ECH power; **b** the chord-averaged electron density; **c** $\tilde{n}/n_{\mathrm{chord}}$ from the low-k FIR scattering at about 1 cm^{-1}; **d** $\tilde{n}/n_{\mathrm{chord}}$ from the intermediate-k FIR scattering at about 8 cm^{-1}. **c** $\tilde{n}/n_{\mathrm{chord}}$ from the high-k millimeter-wave scattering at about 35 cm^{-1}. Note that these ECRH experiments were carried out in DIII-D lower single-null ohmic L-mode plasmas with a toroidal field of 1.9 T, a plasma current of 700 kA, and a line-averaged density of 1.5×10^{19} cm^{-3}. The figure is from Fig. 8 in Ref. (Rhodes 2007a). Reprinted from Ref. (Rhodes 2007a), with the permission of AIP Publishing

of the HF spectral component, $P_{\mathrm{norm,HF}}$, (Fig. 29a) and the LF spectral component, $P_{\mathrm{norm,LF}}$, (Fig. 29b) in the UHR ES frequency spectrum (normalized to their respective value at t=29 ms), and 180 kW of lower hybrid wave was launched into a 32 kA ohmic plasma at $t \approx 30$ ms and was terminated at $t \approx 36$ ms. Figure 29a shows that after LHH is turned on, $P_{\mathrm{norm,HF}}$ is significantly increased at $r \lesssim 6.5$ cm, starting in the core and moving toward the plasma edge, while $P_{\mathrm{norm,LF}}$ is actually reduced in most of the measured radial region. At the same time, the normalized η_e, $1.25L_n/L_T$, (normalized to the critical η_e of 0.8 seen in Eq. 13) starts to increase in the plasma core after the LHH is turned on, and higher values of $1.25L_n/L_T$ continue to propagate outward, consistent with the core electron heating of LHH. The $1.25L_n/L_T > 1$ region (presumably the unstable region for the ETG mode) also expands from the core to the edge, consistent with the behavior of $P_{\mathrm{norm,HF}}$, which indicates that the HF spectral component observed in the ES frequency spectrum may be due to the ETG mode. Although there is a positive correlation between larger electron heat flux and enhanced electron-scale turbulence, causality has not been established, and coupling with nonlinear numerical simulations is needed for further assessments.

The response of electron-scale (high-k), intermediate-k, and low-k turbulence to ECRH has been studied on DIII-D tokamak (Rhodes 2007a, b). The electron-scale ($k_\perp$ ~35–30 cm^{-1} and 4–10 $1/\rho_i$) turbulence was measured with the 94 GHz back scattering system (see Sect. 3.2.1 for more about this high-k diagnostic). Note that the $k_\perp$ measured by this high-k diagnostic is mostly k_r with a small component of k_θ. The intermediate-k ($k_\perp$ ~8–20 cm^{-1} and 1–3 $1/\rho_i$) and low-k ($k_\perp$ ~0–2 cm^{-1} and 0–0.6 $1/\rho_i$) turbulence was measured with an FIR scattering system (Rhodes 2006). In one of the studies (Rhodes 2007a), ~ 0.7 MW of 110 GHz ECRH was initiated at 2000 ms and stepped up every 300 ms to reach a maximum input power of 2.4 MW (see Fig. 30a) into DIII-D lower single-null ohmic L-mode plasmas with a toroidal field of 1.9 T, a plasma current of 700 kA, and a line-averaged density of 1.5×10^{19} cm^{-3}. The ECRH energy deposition is around $r/a = 0.6 \pm 0.1$. T_e is found to increase everywhere in the plasma with the same step-up fashion as the ECRH injection, while T_i is largely unaffected. n_e is, on average, lowered by 10–20% due to ECRH (see Fig. 30b), and, profile-wise, is reduced everywhere in the plasma except at the edge. It is clear that the normalized low-k and intermediate-k density fluctuation level, $\tilde{n}/n_{chord}$ (with $\tilde{n}$ being the RMS of the density fluctuation and n_{chord} being the chord-averaged electron density), remains largely unchanged during the ECRH stepping-up (see Fig. 30c and d), while the high-k density fluctuation level increases as the ECRH power increases, achieving a 40% enhancement with the maximum ECRH power (see Fig. 30e). This demonstrates a strong correlation between the increase in electron thermal transport with enhanced high-k fluctuations, showing that high-k fluctuations may be responsible for the electron thermal transport. The reason why the low-k and intermediate-k fluctuations remain largely unchanged may be due to a significantly increased E×B shearing rate with ECRH. It is noted that although ECRH does not provide direct momentum injection, it changes profiles resulting in modifications of intrinsic momentum drive that lead to a change in the rotation profile and thus the ExB shear (Rhodes 2007a). We note that the low-k and intermediate-k measurements in Fig. 30 are chord-averaged through the whole plasma, while the high-k measurement is from the plasma edge to

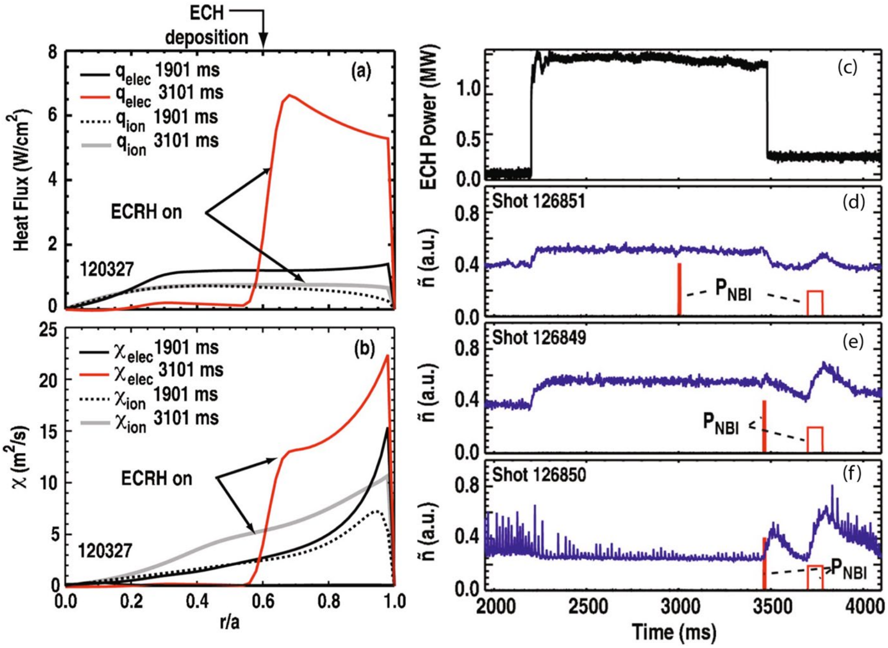

Fig. 31 Radial profiles of electron and ion heat fluxes **a** and thermal diffusivities, **b** in the ohmic phase and ECH/ECRH phase with ECH/ECRH power deposition at $r/a = 0.6$. Temporal evolutions of **c** power injection of ECH/ECRH and the RMS density fluctuation level of high-k turbulence at $\rho \sim 1$ (**d**), 0.6 (**e**), and 0.35 (**f**). Note that these ECRH experiments were carried out in DIII-D lower single-null ohmic L-mode plasmas with a toroidal field of 1.9 T, a plasma current of 700 kA, and a line-averaged density of 1.5×10^{19} cm^{-3}. Panels a and b are adapted from Fig. 5 and panels c-f are adapted from Fig. 11 in Ref. (Rhodes 2007a). Reprinted from Ref. (Rhodes 2007a), with the permission of AIP Publishing

the 94 GHz 2nd ECR surface, i.e., at $r/a = 0.3$. A comparison of heat flux and thermal diffusivity profiles in the ohmic phase and ECRH phase is shown in Fig. 31a and b. A significant increase (decrease) in electron heat flux and thermal diffusivity at radii larger (smaller) than the ECH deposition location in the ECRH phase than in the ohmic phase can be easily seen, while ion heat flux and thermal diffusivity are less affected. To investigate the radial dependence of the high-k turbulence response to ECRH, radially resolved high-k measurements (see Fig. 31d–f) were made in a similar ECRH plasma as in Fig. 30 with the upgraded high-k back scattering system discussed in the last section. The high-k density fluctuation level is seen to increase at larger radii, i.e., $r/a \sim 1$ and 0.6 (see Fig. 31d and e; note that the measurement region is about ±10 cm), in response to the ECRH increase shown in Fig. 31c, while the high-k density fluctuation level at a smaller radius, $r/a \sim 0.35$, is actually reduced with ECRH. We note that this radial response of high-k turbulence to ECRH is consistent with the radial variation of experimentally determined electron and thermal diffusivity in response to ECRH shown in Fig. 31a and b. The measured R/L_{T_e} and the critical $(R/L_{T_e})_{ETG}$ [calculated with Eq. 13 (Jenko 2001)] for the ETG mode between the ohmic and ECRH phases are compared in Fig. 32. It is seen that

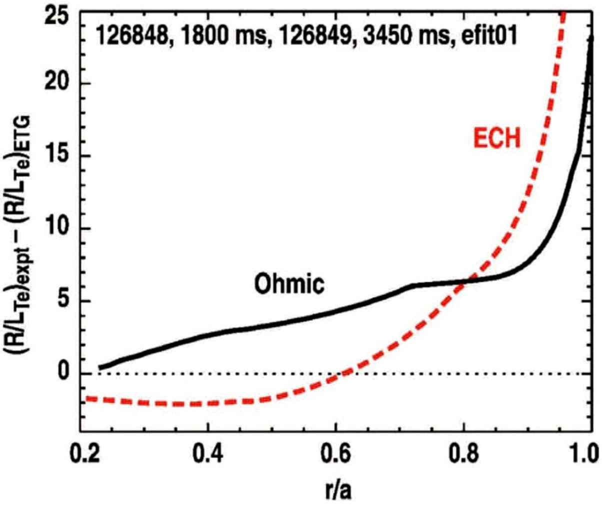

Fig. 32 Difference between the measured R/L_{T_e} and the ETG mode critical $(R/L_{T_e})_{ETG}$ (calculated using Eq. 13) for both ohmic phase (black solid line) and ECRH/ECH phase (red dashed line). The horizontal dashed line denotes zero difference, where the ETG mode should be at marginality. Note that these ECRH experiments were carried out in DIII-D lower single-null ohmic L-mode plasmas with a toroidal field of 1.9 T, a plasma current of 700 kA, and a line-averaged density of 1.5×10^{19} cm^{-3}. The figure is from Fig. 17 in Ref. (Rhodes 2007a). Reprinted from Ref. (Rhodes 2007a), with the permission of AIP Publishing

in the ohmic phase, the ETG mode is everywhere unstable in the plasma, since the experimental R/L_{T_e} is larger than the critical, while in the ECRH phase, the ETG mode becomes stable at $r/a \lesssim 0.6$, less unstable at $0.6 \lesssim r/a \lesssim 0.8$, and more unstable at $r/a \gtrsim 0.8$. The high-k turbulence measurement at $\rho \sim 1$ is consistent with the local linear analysis at $\rho \sim 1$ where increased high-k fluctuation in the ECRH phase is in agreement with a more unstable ETG mode. Agreement at $r/a \sim 0.35$ is worse, since the ETG mode is seen stable in the ECRH phase, but the high-k turbulence is not totally suppressed, although the overall trend is the same. On the other hand, the experimental observation at $r/a \sim 0.6$ is not consistent with the local linear analysis, since a higher high-k fluctuation level is seen at $r/a \sim 0.6$, while the ETG mode is predicted to be more stable at this location. Thus, the local linear analysis can only explain a part of the experimental observation. However, the observed enhancement in high-k turbulence in responding to the increased electron heating strongly suggests an important role of the ETG mode in driving electron thermal transport. We note that similar observations of high-k turbulence response to ECRH are also reported for lower-ECRH-power discharges in Rhodes (2007b) and Wang (2011).

The ETG mode could be of particular importance to NSTX and NSTX-U, since the large E×B shear and strong plasma shaping tend to almost completely suppress low-k turbulence, e.g., in NSTX NBI-heated H-mode plasmas. In fact, the ion thermal transport can be of the neoclassical level throughout the core region (Ren 2017). On the other hand, ETG linear growth rates are usually much larger than the E×B shearing rate and thus can survive the E×B shearing stabilization (except for the case where the ETG mode is very close to marginal stability (Smith 2009); see more discussion on this later in this section). As a result, the ETG mode is a natural candidate for driving electron thermal transport in NSTX/NSTX-U plasmas. Compared with the MT mode, the ETG mode is most likely the dominant mode in low-β and low-collisionality plasmas and could be more important for NSTX-U due to the 3–6 times lower collisionality achievable on NSTX-U (Menard et al. 2011), and furthermore, nonlinear multi-scale gyrokinetic simulations show that MT turbulence could be suppressed by ETG turbulence due to the shearing of radially fine MT current sheet by ETG streamers (Maeyama 2017a). On the other hand, future STs would have even higher β [e.g., toroidal $\beta > 10\%$ with an aspect ratio of 1.6 (Menard 2016)], a feature putting them apart from the conventional-tokamak-based power plant designs. Thus, MTM favored by high β could be important in these future high-β ST plasmas. Indeed, a recent investigation of micro-instability of a conceptual equilibrium for a high β burning ST reactor shows that the dominant instabilities at mid-radius based on designed profiles are KBM and MTM, and the ETG mode is found to be stable (Patel 2021). However, the absence of the ETG mode in this scenario may not be due to the high β, but due to the combination of designed T_e and n_e gradients, T_e/T_i ratio, and geometric factors. In fact, the parametric study of the ETG mode critical T_e gradient by Jenko (2001) shows a slightly destabilization effect of finite β (see Sect. 2.1.2; note that Eq. 13 has no β dependence, since the dependence on β is too weak). Furthermore, the ETG mode is predicted to be unstable in even higher-β FRC plasmas ($\beta \sim 1$ for FRCs) (Farengo 1989), and nonlinear electromagnetic ETG simulations have also shown that the electron thermal transport driven by ETG turbulence is dominantly electrostatic in finite-β ST plasmas (Guttenfelder and Candy 2011; Ren 2012). Thus, the importance of MTM in high-β plasmas seen in Ref. (Patel 2021) is likely due to β-induced destabilization of MTM other than β-induced stabilization of the ETG mode, although a threshold of β for MTM to overtake the ETG mode is probably case-dependent. As for extrapolating to future STs, it is also important to determine the ρ_e^* scaling of electron thermal transport driven by ETG turbulence. It is already well established that global ITG turbulence simulations can successfully recover the local flux-tube transport level in the $\rho^* \rightarrow 0$ limit where $\rho^* = \rho_i/a$ is the normalized ion gyroradius (note that the gyro-Bohm scaling (Kadomtsev 1975) applies in the $\rho^* \rightarrow 0$ limit) and that the local flux-tube transport level is the upper limit in $\rho *$ scans (Lin 2002; Candy 2004). Although these results were obtained for ITG turbulence, they should be applicable to ETG turbulence, since a long-wavelength cutoff naturally exists for ETG turbulence (Jenko 2002; Told 2012) and ETG turbulence has a much smaller characteristic scale than ITG turbulence. In fact, the ETG-turbulence-driven electron thermal transport is shown to satisfy the gyro-Bohm scaling when ρ_e^* is sufficiently small as seen in Lin (2005), Hatch (2017), and Kotschenreuther (2017), while with larger ρ_e^*, the ETG-turbulence-driven electron thermal transport scaling is found to be not gyro-Bohm (Bottino 2007). This favorable scaling with small-enough ρ_e^* is certainly welcome news for future STs usually characterized by a larger size and/or a stronger magnetic field than present STs, and, however, we must caution that the ETG mode is not expected to be the sole operating instability in future STs. On the other hand, the deviation from the gyro-Bohm scaling with finite system size

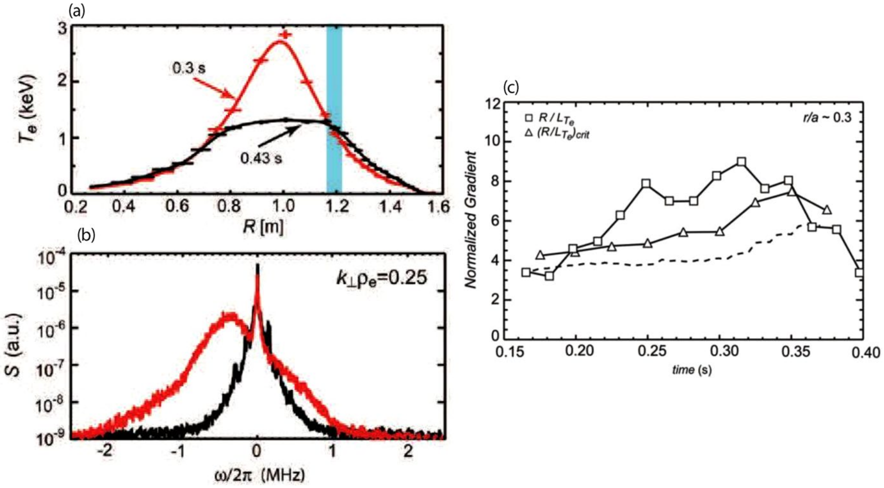

Fig. 33 Temperature profiles (**a**) and spectral density of fluctuations (**b**) at 0.3 s (red, with RF heating) and 0.43 s (black, without RF heating). The blue rectangle indicates the location of the measurement region of the high-k scattering system where L_{T_e} is 15 cm and 50 cm, respectively. Negative frequencies (bottom) correspond to wave propagation in the electron diamagnetic direction. **c** Temporal evolution of experimentally measured normalized T_e gradient, R/L_{T_e} (squares) and GS2-calculated normalized critical T_e gradient, $(R/L_{T_e})_{crit}$ (triangles) for the ETG mode at $r/a \sim 0.3$. $(R/L_{T_e})_{crit}$ using Eq. 13 (Jenko 2001) is shown as the dashed line. This is an NSTX RF-heated helium plasma with a minor radius of 0.65 m, a major radius of 0.85 m, an elongation of 2, a toroidal magnetic field of 0.55 T, a plasma current of 700 kA, and an RF-heating power of 1.2 MW. Panels a and b are adapted from Fig. 10 and panel c is adapted from Fig. 21 in Ref. (Mazzucato 2009), with the permission of International Atomic Energy Agency

is found to be controlled by the temperature gradient profile width, ω, and a better finite size scaling should be expressed in terms of $\rho^*_{\mathrm{eff}} = \rho_i/\omega$ (McMillan 2010; Villard 2010). In Refs. (Lin 2002; Candy 2004; Lin 2005; Hatch 2017; Kotschenreuther 2017), since only ρ^* or ρ^*_e is varied with ω/a kept constant and the transport scales similarly with both ρ^* andρ^*_{eff}. However, if ρ^* is varied with fixed ρ^*_{eff}, ρ^* variations alone do not significantly change the transport level (McMillan 2010). Thus, if the T_e gradient profile scales with a (i.e., $\omega/a \sim$ constant) when scaling to future STs, the local flux-tube predictions of ETG-turbulence-driven electron thermal transport (i.e., using the gyro-Bohm scaling) would be sufficient. On the other hand, the existence of transport barriers may break the $\omega/a \sim$ constant scaling. In this context, the transport deviation from the gyro-Bohm limit due to global effects would persist for smaller ρ^*_e, and global simulations would be needed for predicting the ETG-turbulence-driven electron thermal transport. Furthermore, to self-consistently simulate the generation of transport barriers (and how their width scales with system size), global simulations may also be needed.

The first experimental evidence of the ETG mode on NSTX was observed in NSTX RF-heated helium L-mode plasmas using the high-k scattering system (Mazzucato 2008, 2009). We note that L-mode plasmas were chosen, since their T_e profile is usually not stiff (the stiffness here denotes the ability of auxiliary heating to vary the normalized T_e gradient). The RF-heating system on NSTX, which provides core electron heating, was used to change the local electron temperature gradient ($r/a \sim 0.3$), as shown in Fig. 33a, where the T_e profile with RF heating ($t = 0.3$ s) is seen to have a significantly larger gradient (~ a factor of three increase) in the measurement region of the high-k scattering system (denoted by a blue rectangle) than the T_e profile without RF heating at $t = 0.43$ s. Furthermore, T_e in the high-k measurement region is essentially unchanged with or without RF heating, meaning that the same normalized wavenumber ($k_\perp \rho_e = 0.25$) is being measured with or without RF heating, which ensures that comparing the scattering spectral power using just one high-k detecting channel is meaningful. Figure 33b shows the frequency spectra of $k_\perp \rho_e = 0.25$ with and without RF heating measured by the high-k scattering system. We note that the off-center spectral peak (i.e., $f \approx -350$ kHz at $t = 0.3$ s with RF heating) is due to the scattering signal, while the central spectral peak at $\omega/2\pi = 0$ is due to spurious radiation, e.g., microwave power reflected by the NSTX vacuum vessel that is not Doppler-shifted as the scattering signal due to Bragg scattering with plasma turbulence. Having some Doppler shift (due to a combination of plasma toroidal rotation and turbulence propagation in the plasma frame) from Bragg scattering greatly helps distinguish the real scattering spectral peak from that of the unwanted spurious radiation. It is clear from Fig. 33b that there is a significant increase in the scattered power with RF heating (the off-center spectral peak $f \approx -350$ kHz) and there is almost none without it (note that the spectral peak of spurious radiations is symmetric around $\omega/2\pi = 0$), showing that the measured turbulence has a positive correlation with the local electron temperature gradient. In addition,

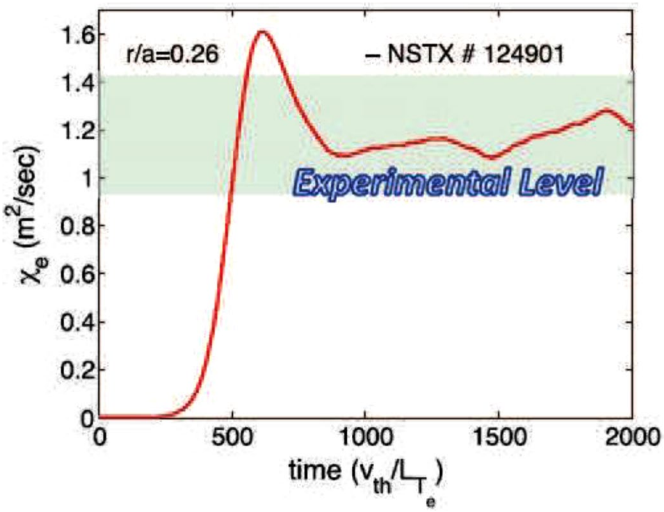

Fig. 34 Time history of χ_e at $r/a = 0.26$ from a global ETG simulation of an RF-heated helium L-mode plasma (with an injected RF power of 2 MW) similar to the case in Fig. 33 and comparison with experimental χ_e range (denoted by the shaded rectangular region) from power balance analysis. The figure is from Fig. 17 in Ref. (Wang 2015). Reprinted from Ref. (Wang 2015), with the permission of AIP Publishing

the scattering signal spectrum peaks at a negative frequency which denotes the electron diamagnetic drift direction, consistent with that of the ETG mode. Thus, we consider these as strong experimental evidence of the presence of the ETG mode in these RF-heated plasmas. Linear stability analysis carried out with the GS2 code (Kotschenreuther 1995) shows that the ETG mode is indeed linearly unstable at $t = 0.3$ s with $R/L_{T_e} > (R/L_{T_e})_{\mathrm{crit}}$ ($(R/L_{T_e})_{\mathrm{crit}}$ from GS2 calculations), while the ETG mode becomes stable at $t > 0.35$ s and remains so for $t = 0.43$ s (see Fig. 33c). Thus, these electron-scale turbulence measurements coupled with linear gyrokinetic stability analysis strongly support the existence of ETG turbulence in these RF-heated L-mode plasmas.

The role of ETG turbulence in driving electron thermal transport in a similar RF-heated L-mode plasma as that shown in Fig. 33 was investigated using the global GTS code (Wang 2010) which calculates electrostatic turbulence in realistic tokamak configurations. Adiabatic ions are used in the global ETG simulation, and the coupling between ETG and low-k turbulence is neglected to keep the computational cost at an acceptable level. Figure 34 shows the temporal evolution of the GTS-predicted χ_e, where χ_e, after an initial overshoot, nonlinearly saturates to a level in agreement with the experimental range inferred from power balance analysis (Wang 2015). This agreement strongly suggests that ETG turbulence could play an important role in driving electron thermal transport in these RF-heated L-mode plasmas. As we have discussed in Sect. 2.2.2, this simulation revealed a direct energy channeling from ETG turbulence to e-GAM and low-frequency zonal flows which provides the nonlinear ETG mode saturation. It is well known that the linear ETG mode has a weak direct dependence on electron collisionality due to its large real frequency. However, given this strong coupling with e-GAM and low-frequency zonal flows, the collisional damping of zonal flows and e-GAMs could lead to a dependence of ETG-turbulence-driven electron thermal transport on electron collisionality, which is in analogy to the well-known paradigm of the zonal flow regulating ITG turbulence and may lead to scaling of energy confinement time that is proportional to $1/\nu_e^*$ as discussed in Kim (2003). This mechanism is subject to further investigation using global nonlinear ETG GTS simulations with scans in electron collision frequency. We note that long-time ETG simulations by Colyer (2017) have shown a strong collisionality dependence of electron thermal transport in the late-time quasi-stationary low-transport phase featured by robust zonal flows, and the collisional damping of zonal flows was found to be responsible for determining the final saturation level of ETG turbulence. This result potentially could be consistent with the ST confinement scaling (Kaye 2007a; Valovič 2011). However, we must caution that it is unclear in Ref. (Colyer 2017) whether the predicted electron thermal transport in the late-time low-transport phase is able to match the experimental electron heat flux at the simulated radial location.

We note that varying T_e gradient through the targeted electron heating method has provided the most convincing evidence of the ETG mode and its important role in driving electron thermal transport in tokamaks, which is due to the fact that T_e gradient is the free energy to drive the ETG mode. In addition to driving force, we are also interested in the stability characteristics of the ETG mode, i.e., parameters controlling the ETG mode stability, since after all, we would like to control the ETG

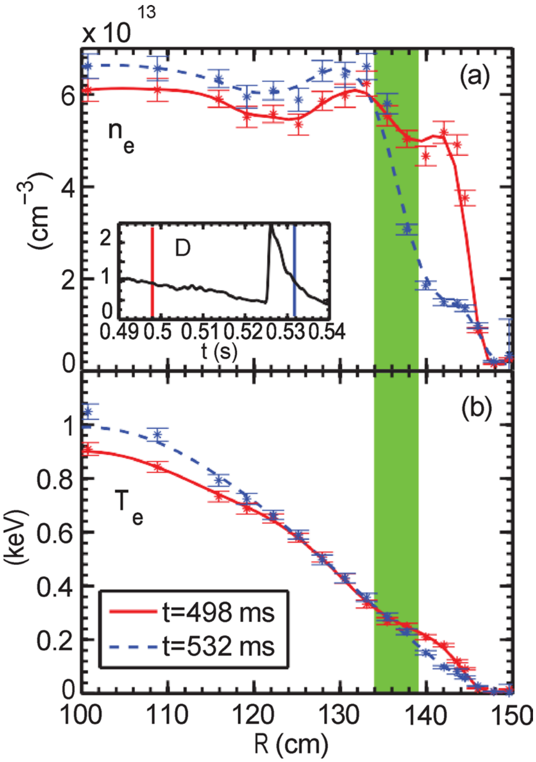

Fig. 35 **a** Radial profiles of electron density at $t = 498$ and 532 ms which are before and after an ELM event (see the inserted D_α signal, where the two vertical lines denote the two Thompson time points); **b** radial profiles of electron temperature at $t = 498$ and 532 ms. The shaded regions denote the measuring region of the high-k system. Large change in L_{n_e} after the ELM at $t = 532$ ms is evident. Note that the observation was made in a deuterium H-mode plasma with 900 kA plasma current and 4.5 kG toroidal field. The figure is from Fig. 1 in Ref. (Ren 2011). Reprinted with permission from Ref. (Ren 2011). Copyright (2011) by the American Physical Society

mode to reduce electron thermal transport and to improve energy confinement. The linear stability of the ETG mode has been extensively studied and we have provided a review in Sect. 2. Particularly useful results are the analytical forms of the ETG mode linear critical threshold, $(R_0/L_{T_e})_{crit}$, e.g., Eqs. 13 and 15, where stability effects of z_{eff}, T_e/T_i, R/L_{n_e} and $\hat{s}/q$ are evident. In addition, these parameters most likely not only play a role linearly but also nonlinearly. We will review some experimental parametric studies of electron-scale turbulence in the following to further explore the role of electron-scale turbulence, particularly ETG turbulence, in driving electron thermal transport.

Density gradient dependence: We note that density gradient dependence of the ETG mode has been predicted by ETG mode theories (through the parameter η_e, thus the well-known name of η_e mode, (Lee 1987; Horton 1988; Jenko 2001)) and gyrokinetic simulations (Jenko 2001). In particular, the analytic form of the linear critical temperature gradient for the ETG mode as in Eq. 13 is quite revealing. Here, we want to emphasize that the density gradient term $(0.8R_0/L_{n_e})$, if large enough, could determine the critical temperature gradient alone and result in the stabilization of the ETG mode. Confinement improvements have been observed to be associated with peaked density profile resulting from pellet injection in tokamaks and stellarators (Greenwald 1984; Bozhenkov 2020; Beidler 2021), and the improvements were attributed to density gradient (Bozhenkov 2020; Beidler 2021), perpendicular

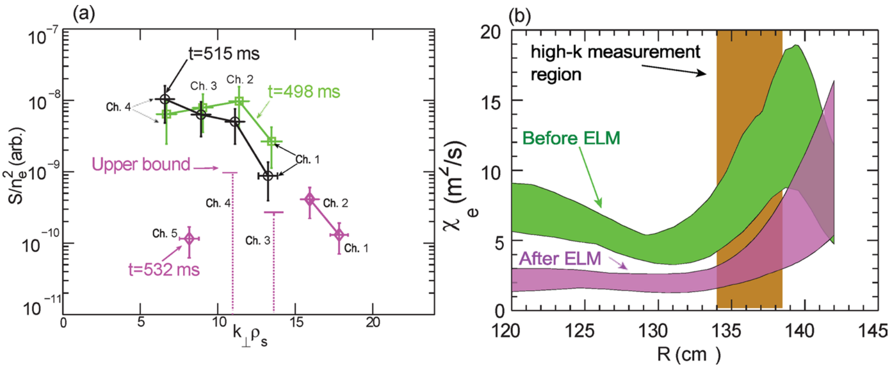

Fig. 36 **a** The $k_\perp$ spectra at three MPTS time points t = 498, 515 and 532 ms with the last time point after the ELM event (S is the spectral density). The absolute upper bounds for the density fluctuation spectral power are denoted by horizontal solid lines on the tops of vertical dashed lines. **b** The electron thermal diffusivity as a function of R before the ELM at t = 498 (green) and after the ELM at t = 532 (magenta) with the shaded region denoting the high-k measurement regions. The uncertainty in calculated χ_e is mainly due to uncertainties in ohmic heating and measured kinetic profiles. Note that the observation was made in the deuterium H-mode plasma with 900 kA plasma current and 4.5 kG toroidal field, as shown in Fig. 35. Panel a is adapted from Fig. 5 and panel b is adapted from Fig. 7 in Ref. (Ren 2012). Reprinted from Ref. (Ren 2012), with the permission of AIP Publishing

flow shearing, and/or reversed magnetic shear (Balet 1990; Maget 1999; Romanelli 2004). The first direct experimental demonstration of density gradient stabilization of electron-scale turbulence on NSTX was presented in Ref. (Ren 2011). Quantitative agreement with linear numerical simulations has been made with experimental observations, which supports the conclusion that the observed density fluctuations are driven by the ETG mode. Particularly, it is found that the smaller wavenumber modes, $k_\perp\rho_s \lesssim 10$, are strongly stabilized by the electron density gradient and that a factor of two reduction in plasma effective thermal diffusivity was observed along with the stabilization. This finding of density gradient stabilization of ETG turbulence supports the importance of density profile control in controlling ETG turbulence and in improving electron energy confinement, a potential experimental knob for future device optimization.

The observation of density gradient stabilization of electron-scale turbulence was made around a large ELM event (Zohm 1996) (see the inserted D_α signal in Fig. 35a) in an NSTX deuterium H-mode plasma with 900 kA plasma current and 4.5 kG toroidal field which leads to a factor of 5 increase in the normalized electron density gradient in the high-k measurement region with much-less variations in the other equilibrium quantities (Ren 2011). Figure 35a shows the steepening of the density profile in the high-k measurement region (from about R = 134 to 139 cm) at t=532 ms (after the ELM event) in comparison with that at t=498 ms (before an ELM event) measured by Multiple Point Thomson Scattering (MPTS) (LeBlanc 2003). Only a small change in the T_e profile before and after the ELM event is seen in Fig. 35b, an interesting feature of this ELM event, and a/L_{T_e} actually increased in the high-k measurement region after the ELM event (Ren 2011). No large amplitude global MHD activity is seen before, during, or right after the ELM event.

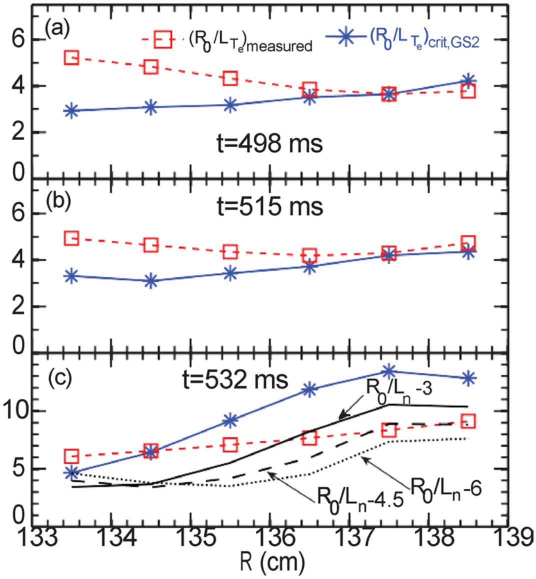

Fig. 37 The critical T_e gradients calculated by GS2, $(R_0/L_{T_e})_{crit,GS2}$, (asterisks) in comparison with the measured temperature gradient, $(R_0/L_{T_e})_{measured}$, (open squares) in the high-k measurement region: **a** at $t = 498$ ms; **b** $t = 515$ ms; **c** $t = 532$ ms. Additional lines in (**c**) denote $(R_0/L_{T_e})_{crit,GS2}$ calculated with $(R_0/L_{n_e} - 3)$ (solid line), $(R_0/L_{n_e} - 4.5)$ (dashed line) and $(R_0/L_{n_e} - 6)$ (dotted line). Here, $(R_0/L_{n_e} - x)$ means that the normalized density gradient used in stability calculations is reduced by x units from the experimental value where $x = 3$, 4.5, or 6. Note that the GS2 linear stability analysis is based on the deuterium H-mode plasma with 900 kA plasma current and 4.5 kG toroidal field as shown in Fig. 35. The figure is from Fig. 9 in Ref. (Ren 2012). Reprinted from Ref. (Ren 2012), with the permission of AIP Publishing

A positive correlation between electron-scale turbulence and electron thermal transport was observed before and after the ELM event, as shown in Fig. 36. Fluctuation spectral power is seen reduced after the ELM ($t = 532$ ms) at $k_\perp \rho_s \lesssim 15$ compared with those at $t = 498$, 515 (before the ELM event) (spectra chosen at three exact MPTS time points), and the more-than-an-order-of-magnitude reduction is seen at small wavenumbers, $k_\perp \rho_s \lesssim 10$. This stabilization of electron-scale turbulence is found to be accompanied by a factor of about two reduction in electron thermal diffusivity, χ_e [calculated using power balance analysis using the TRANSP code (Hawryluk 1981)] in the high-k measurement region, as shown in Fig. 36b. This positive correlation between the measured electron-scale turbulence and experimental electron thermal transport indicates that the reduction in the relatively smaller wavenumber modes, $k_\perp \rho_s < 10$, may be responsible for the improvement in electron thermal transport. In contrast to electron thermal transport, ion thermal transport remains on the neoclassical level before and after the ELM event. Note that additional mechanisms beyond ETG turbulence are necessary to account for the observed electron thermal transport after the ELM event as discussed below (see the discussion with regard to Fig. 38b), despite the more-than-an-order-of-magnitude

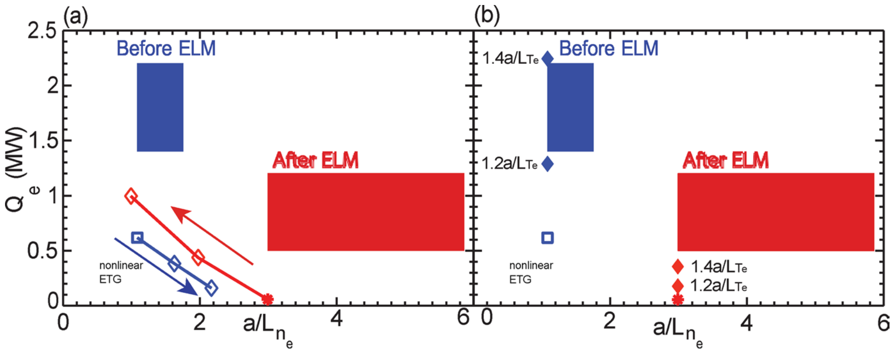

Fig. 38 **a** Experimental electron heat flux from TRANSP analysis (solid rectangles) and calculated Q_e from nonlinear GYRO simulations (asterisk and open square) before the ELM ($t = 498$ ms) and after the ELM ($t = 532$ ms). Parametric scans (open diamonds) in density gradient based on "Before ELM" and "After ELM" parameters are also shown. **b** The same as (**a**), except that parametric scans are in a/L_{T_e}. The experimental electron heat flux from power balance analysis is represented by the solid blocks whose height denotes the experimental uncertainty and whose width denotes the range of density gradient for the radial region of $R = 133.5$ to 135.5 cm, the inner half of the high-k measurement region which nonlinear simulations were carried out for. The reduction in Q_e after the ELM is mostly due to the decrease in electron and ion coupling, and larger radiation loss and dW_e/dt (W_e is the electron thermal energy) also contributed. Note that these nonlinear GYRO simulations are based on the deuterium H-mode plasma with 900 kA plasma current and 4.5 kG toroidal field, as shown in Fig. 35. The figure is from Fig. 11 in Ref. (Ren 2012). Reprinted from Ref. (Ren 2012), with the permission of AIP Publishing

reduction in the measured electron-scale turbulence spectral power at $k_\perp \rho_s \lesssim 10$ after the ELM event.

The GS2 code using local Miller equilibria (Miller 1998) was used to address the density gradient effect on the ETG mode linear stability before and after the ELM events. In particular, the critical ETG calculated using the GS2 code, $(R_0/L_{T_e})_{crit,GS2}$, and the measured normalized T_e gradient, $(R_0/L_{T_e})_{measured}$, in the high-k measurement region are plotted in Fig. 37 at three exact MPTS time points. Figure 37a and b shows that $(R_0/L_{T_e})_{measured}$ is larger than $(R_0/L_{T_e})_{\mathrm{crit,GS2}}$ before the ELM, i.e., $t = 498$ ms and 515 ms, in the majority of the high-k measurement region. On the other hand, $(R_0/L_{T_e})_{\mathrm{crit,GS2}}$ becomes much larger than $(R_0/L_{T_e})_{\mathrm{measured}}$ in most of the high-k measurement region at $t = 532$ ms, after the ELM (see Fig. 37c), showing that the ETG mode is linearly stabilized in most of the high-k measurement region. This linear stabilization of the ETG mode in the high-k measurement region is likely the origin of the observed large reduction of fluctuation spectral power for $k_\perp \rho_s < 10$ at $t = 532$ ms seen in Fig. 36a. Further linear stability analysis by reducing R_0/L_{n_e} with 3, 4.5, and 6 units demonstrates the stabilization effect of density gradient on the ETG mode that with R_0/L_{n_e} lowered by 3 units significantly lowered critical T_e gradients are seen in the high-k measurement region (see Fig. 37c). Although further reductions in R_0/L_{n_e}, i.e., $(R_0/L_{n_e} - 4.5)$ and $(R_0/L_{n_e} - 6)$, lead to a further reduction in the critical R_0/L_{T_e} at $R > 135.5$ cm, only small changes in the critical R_0/L_{T_e} are seen at $R \lesssim 135$ cm, which is consistent with the first term in the "max" function on the RHS of Eq. 13

dominating the critical R_0/L_{T_e} as the second density gradient term becomes sufficiently small.

Q_e predicted by local nonlinear gyrokinetic ETG simulations using the GYRO code (Candy and Waltz 2003) (with the same local Miller equilibria as used for the linear stability analysis above) is compared with experimental Q_e in Fig. 38a, which shows that after the ELM event, experimental Q_e is reduced by about 1 MW and both the density gradient and its range increased significantly (Ren 2012). The nonlinear simulations based on "Before ELM" and "After ELM" parameters show a significant reduction in the predicted Q_e after the ELM, which is qualitatively consistent with the experimental observation. Nonlinear simulation scans with varied density gradients, i.e., factors of 1.5 and 2 increase in density gradient based on the "Before ELM" parameters and factors of 1/3 and 2/3 reduction based on the "After ELM" parameters, confirm our expectation that the increase in density gradient is responsible for the reduced experimental Q_e after ELM seen in Fig 38a, e.g., a factor of 3 reduction in density gradient can result in an order of magnitude increase in Q_e seen in the scan based on the "After ELM" parameters.

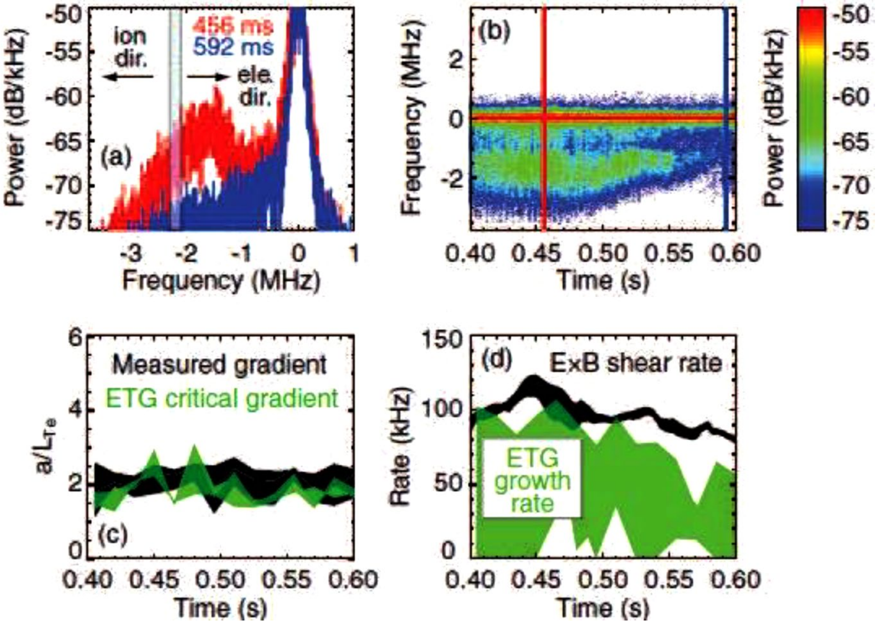

Fig. 39 Fluctuation measurements and linear gyrokinetic calculations for an NSTX NBI-heated H-mode plasma ($B_T = 4.5$ kG and $I_p = 700$ kA) in the high-k measurement region ($R = 133 \pm 2$ cm and $r/a = 0.5 - 0.6$); **a**, **b** fluctuation measurements with $k_\perp \rho_e \approx 0.27 - 0.3$. The gray rectangle marks the Doppler shift from toroidal rotation; **c** measured electron temperature gradient and ETG critical gradient from GS2 calculations; **d** ETG linear growth rate and $E \times B$ shearing rate. The bands illustrate variations in the high-k measurement region. The figure is from Fig. 4 in Ref. (Smith 2009). Reprinted with permission from Ref. (Smith 2009). Copyright (2009) by the American Physical Society

The under-prediction of Q_e against experimental values by nonlinear ETG simulations with nominal experimental parameters (see Fig. 38a) was investigated with a/L_{T_e} scans. The simulations with a 20% and a 40% increase in a/L_{T_e} show that before the ELM, increasing a/L_{T_e} by 20% leads to a more-than-doubled predicted Q_e, while with a 40% increase in a/L_{T_e}, the predicted Q_e is already at the upper bound of the experimental value (see Fig. 38b). However, after the ELM, with a/L_{T_e} increased by 40%, the predicted Q_e still cannot match the experimental values. Thus, an additional mechanism may be needed to account for this discrepancy. Note that after the ELM event, ion-scale TEM was shown to be the most unstable mode (Ren 2012), which is consistent with the well-known density gradient destabilization of TEM (Romanelli 2004), and the maximum linear growth rate of this TEM actually exceeds the $E \times B$ shearing rate. However, a recent global nonlinear ion-scale GTS simulation shows that this TEM is not able to generate the experimental level of electron thermal transport (Wang 2015). The reason behind this discrepancy is still not fully understood.

More recently, the mechanism of density gradient stabilization of ETG turbulence is further confirmed with another set of NSTX H-mode plasmas (Ruiz 2015), where the density gradient enhancement is induced by a plasma current ramp-down. Electron-scale turbulence reduction is observed in correlation with the increase in density gradient, while the T_e gradient remains larger than the linear critical T_e gradient. This indicates that density gradient can also nonlinearly stabilize ETG turbulence, in addition to the linear stabilization effects reported in Ren (2011). This conclusion is supported by local nonlinear ETG GYRO simulations using experimental equilibria (Ruiz 2015). We note that this nonlinear stabilization of ETG turbulence is also consistent with nonlinear simulations with density gradient scans shown in Fig. 38a.

E × B shear dependence: $E \times B$ stabilization of the ETG mode is not expected due to its much higher linear growth rates than that of ion-scale modes and the relatively low E×B shear in conventional tokamaks. However, the E×B shearing rate could be much larger in STs, and indeed, the ETG mode stabilization by $E \times B$ shear was observed with the high-k scattering system in NSTX H-mode plasmas (Smith 2009), where the suppression of the ETG mode close to marginality by E×B shear due to lowered linear growth rate was identified. In Fig. 39, the temporal evolution of electron-scale turbulence is compared with those of maximum linear growth rate (from GS2 calculations) and the Hahm–Burrell E×B shearing rate (Hahm and Burrell 1995) [from TRANSP analysis (Hawryluk 1981)] for an NSTX NBI-heated H-mode plasma. Figure 39b clearly shows that scattering power from plasma turbulence (the off-center peak in the spectrogram) decreases significantly from about $t = 0.45$ s to 0.6 s, and such a reduction can be seen more clearly in Fig. 39a where the frequency spectra at $t = 456$ and 592 ms are shown (these two time points are denoted in Fig. 39b with vertical solid lines with corresponding colors). Furthermore, frequency spectral peaks in Fig. 39a fall on the RHS of the Doppler shift due to plasma E×B drift, i.e., in the electron diamagnetic drift direction. This means that the turbulence propagates in the electron diamagnetic direction in the plasma frame, consistent with ETG turbulence. The comparison between the normalized measured

T_e gradient and GS2-calculated ETG critical T_e gradient in Fig. 39c shows that ETG turbulence is very close to marginal stability through the whole time period shown. The temporal evolutions of the $E \times B$ shearing rate and the maximum ETG growth rate in Fig. 39d show that as the difference between the two gets larger, the measured turbulent spectral power is significantly reduced (see Fig. 39a and b). It is obvious from Fig. 39a, b, and d that the scattering signal power is much smaller at $t = 592$ ms when the maximum ETG linear growth rate is significantly smaller than the $E \times B$ shearing rate. Note this late-time increase in the difference between the $E \times B$ shearing rate and the maximum ETG growth rate is mainly due to the decrease in the maximum ETG growth rate (the $E \times B$ shearing rate also decreases but at a lower rate). The authors pointed out that the decrease in the maximum ETG growth rate from t=500 to 600 ms seen in Fig. 39d is consistent with a simultaneous decrease in $\hat{s}$ in the high-k measurement region. This result indicates that $E \times B$ shear could be an experimental tool to control ETG turbulence in future fusion machines, provided that the T_e gradient is close to the linear stability threshold of the ETG mode. We note that the E×B shear suppression of ETG turbulence may be more general than the result above. Since the shearing effect is more physically determined by the ratio between the E×B shearing rate and the turbulence nonlinear decorrelation rate (Hahm and Burrell 1995), the transport-driving radially extended ETG streamers (Dorland 2000; Jenko 2000) are expected to have a nonlinear decorrelation rate than the ETG maximum linear growth rate and thus are more susceptible to E×B shear. In fact, nonlinear gyrokinetic simulations of E×B shear effects on ST plasmas have shown that transport due to ETG turbulence can be reduced by E×B shear and ETG streamers are tilted with the presence of E×B shear (Guttenfelder and Candy 2011).

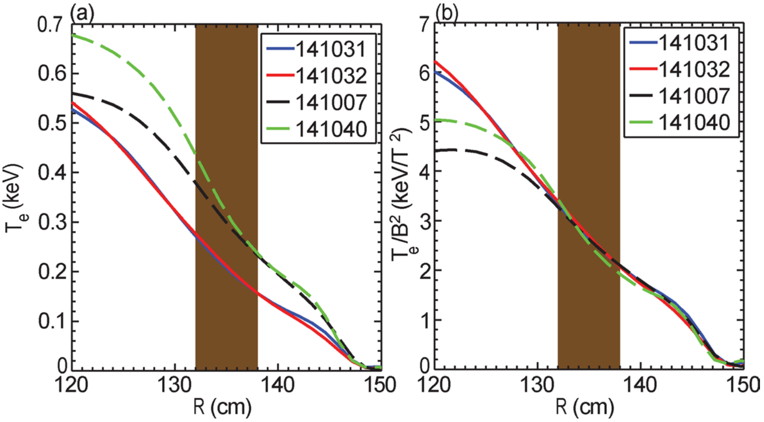

Fig. 40 **a** T_e profiles measured by MPTS at times of interest for the 4 shots used in the analysis ($t = 367$ ms for the low-collisionality shots 141007 and 141040; $t = 332$ ms for the high collisionality shots 141031 and 141032); **b** normalized T_e/B^2 profiles for the 4 shots. The shaded regions in the figures denote the high-k measurement region. Note that the collisionality scan was carried out in NSTX H-mode plasmas by varying B_T and I_p simultaneously with constant B_T/I_p and keeping density approximately constant. The low-collisionality shots (shots 141007 and 141040) have $B_T = 4.5$ kG and $I_p = 900$ kA, and the high collisionality shots (shots 141031 and 141032) have $B_T = 3.5$ kG and $I_p = 700$ kA. The figure is from Fig. 14 in Ref. (Ren 2012). Reprinted from Ref. (Ren 2012), with the permission of AIP Publishing

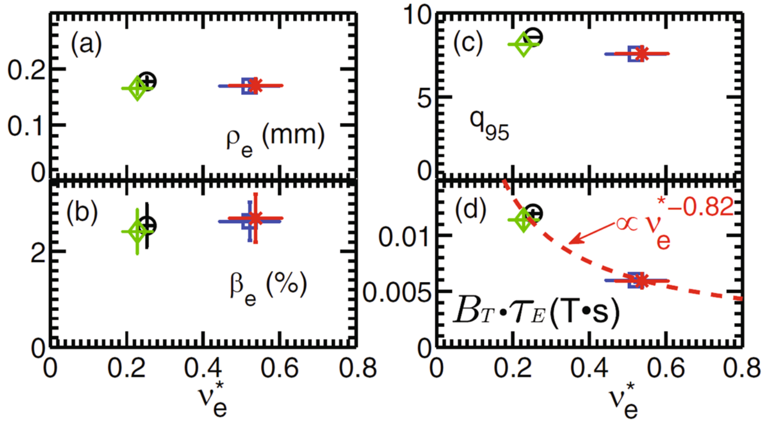

Fig. 41 **a** Local electron gyroradius, ρ_e, **b** local electron beta, β_e, **c** q_{95}, **d** normalized energy confinement time, $B_T\tau_E$, all as a function of electron collisionality, ν_e^* for shots 141031 (blue square), 141032 (red asterisks), 141007 (black circle), and 141040 (green diamond). The local values shown in **a** and **b** are the mean values in the high-k measurement region. The vertical and horizontal error bars denote the variation of corresponding quantities in the high-k measurement region (applicable to ρ_e, β_e, and ν_e^*). The red dashed line in (**d**) denotes the best power law fit for the normalized confinement time versus collisionality, which gives $\nu_e^{*-0.82}$. Note that the collisionality scan was carried out in NSTX H-mode plasmas by varying B_T and I_p simultaneously with constant B_T/I_p and keeping density approximately constant. The low-collisionality shots (shots 141007 and 141040) have $B_T = 4.5$ kG and $I_p = 900$ kA, and the high collisionality shots (shots 141031 and 141032) have $B_T = 3.5$ kG and $I_p = 700$ kA. The figure is from Fig. 15 in Ref. (Ren 2012). Reprinted from Ref. (Ren 2012), with the permission of AIP Publishing

The effects of E×B shear effect on electron-scale turbulence have also been studied in NSTX NBI-heated L-mode plasmas (Ren 2013) and in CRU experiments on FT-2 (Gurchenko 2010), where the normal cascade from unstable ion-scale turbulence to electron scale is likely to determine the observed electron-scale turbulence and the observed variation in electron-scale turbulence against E×B shear should be dominantly determined by the E×B shear stabilization of ion-scale turbulence, i.e., the ITG mode in Ren (2013) and TEM in Gurchenko (2010).

Collisionality dependence: Due to the observed strong collisionality (ν_e^*) dependence of normalized energy confinement time observed in STs (Kaye 2007a; Valovič 2011), it is also of great interest to study the collisionality dependence of ETG turbulence. Note that $\nu_e^* = \nu^{e/i}/(\epsilon\omega_{be})$, where $\nu^{e/i}$ is the electron-ion collision frequency and ω_{be} is the trapped electron bouncing frequency. The ETG mode stability is known not affected by electron collisionality as long as $\omega \gg \nu^{e/i}$. However, the situation is more complicated nonlinearly. An analytical analysis in Kim (2003) shows that collisional damping of ETG-mode-driven zonal flow could lead to stronger ETG turbulence/transport as collisionality increases, which is consistent with the experimental scaling. This is partially supported by the strong coupling with the zonal flow and e-GAMs was observed in global ETG simulations of NSTX plasma (Wang 2015) as discussed above, although the collisional damping of zonal flow and e-GAMs has not been established in the GTS simulation. In addition, the dependence of ETG turbulence on collisionality has been observed in PIC gyrokinetic simulations (Parker 2006). The strongest numerical evidence of this scenario

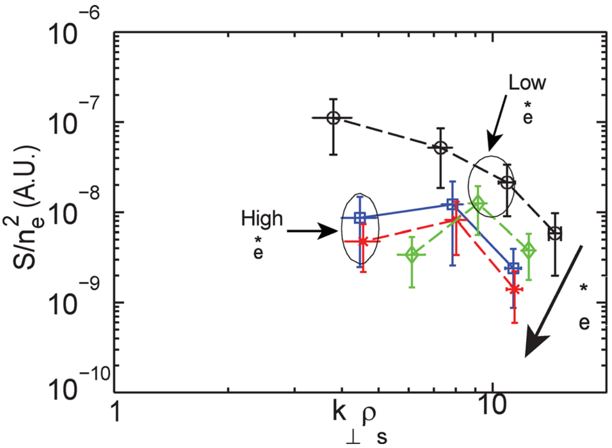

Fig. 42 The $k_\perp$ spectra in arbitrary unit (normalized to n_e^2 and S is the spectral density calculated using the total scattered power in the spectra of each channel) for shots 141031 (blue square), 141032 (red asterisks), 141007 (black circle), and 141040 (green diamond). The first 2 shots are of high collisionality and the latter 2 shots are of low collisionality. The direction of increase of collisionality is denoted by a black arrow. Note that the collisionality scan was carried out in NSTX H-mode plasmas by varying B_T and I_p simultaneously with constant B_T/I_p and keeping density approximately constant. The low collisionality shots (shots 141007 and 141040) have $B_T = 4.5$ kG and $I_p = 900$ kA, and the high collisionality shots (shots 141031 and 141032) have $B_T = 3.5$ kG and $I_p = 700$ kA. The figure is from Fig. 16 in Ref. (Ren 2012). Reprinted from Ref. (Ren 2012), with the permission of AIP Publishing

came from GS2 simulations of an MAST H-mode plasma (Colyer 2017), where a long-time evolution of zonal flows has shown a strong collisionality dependence, and electron thermal transport proportional to electron collisionality due to the collisional damping of zonal flows has been observed. Here, we provide a review of an experimental study of this dependence from a collisionality scan carried out using low β NSTX NBI-heated H-mode plasmas with ρ_e, β_e, and q_{95} kept approximately constant (Ren 2012). The MT modes are stable in these low β plasmas, as confirmed by linear gyrokinetic analysis.

The collisionality scan was carried out by varying B_T and I_p simultaneously with constant B_T/I_p and keeping density approximately constant, following an established experimental procedure in NSTX (Kaye 2007a) with the low-collisionality shots having $B_T = 4.5$ kG and $I_p = 900$ kA and the high collisionality shots having $B_T = 3.5$ kG and $I_p = 700$ kA. By keeping T_e/B^2 locally constant, where B is the total local magnetic field strength, local ρ_e and β_e remain approximately constant in the collisionality scan. T_e profiles at $t = 367$ ms for the two low-collisionality shots (141007 and 141040) and at $t = 332$ ms for the two high collisionality shots (141031 and 141032) are shown in Fig. 40a, where the collisionality variation almost exclusively comes from changes in T_e (see the higher T_e in the high-k measurement region of the low-collisionality shots). Figure 40b shows the normalized T_e/B^2 profiles with a good overlap among the profiles in the high-k measurement region, where the B profiles are from LRDFIT equilibrium reconstructions constrained by MSE measurements (Menard 2006; Levinton 2007). The collisionality scan achieved a factor of about 2.5 variation in collisionality (see Fig. 41). Figure 41a–c shows that ρ_e, β_e, and q_{95} were kept relatively constant with less than 15% variation in the collisionality scan. As shown in Fig. 41d, the normalized confinement time, $B_T\tau_E$, decreases as collisionality increases, and a power law fitting with the form of $\nu_e^{*\alpha}$ yields $\alpha = -0.82$, which appears to be consistent with the previous result of $\alpha = -0.92$ (Kaye 2007a), although an uncertainty analysis (not reported in Ren (2012)) is still needed to assess this consistency.

However, the measured ETG turbulence wavenumber spectra show quite complicated dependence on electron collisionality. Figure 42 shows that an anti-correlation between the measured turbulence spectral power and collisionality exists for $k_\perp\rho_s > 9$. On the other hand, the collisionality dependence of the turbulence spectra at $k_\perp\rho_s < 9$ is quite different with one low-collisionality shot (green diamond) having smaller spectral power than the high collisionality shots in this wavenumber range. This spectral difference between the two nominally similar low-collisionality shots, 141007 and 141040, might be due to a combination of differences in the linear growth rate spectral shape and E×B shear between the shots (see Ren (2012) for more details). After this E×B shear stabilization of lower wavenumber fluctuations is taken into account, the measured electron-scale turbulence spectral power appears to increase as collisionality decreases, obviously inconsistent with the observed confinement dependence on electron collisionality. However, a complete understanding of this discrepancy has not yet been achieved. Although the change in the electron–ion collision frequency is much larger than the changes in any other equilibrium quantities in the scan, smaller changes in other parameters could still contribute to the observed change in turbulence, e.g., q and a/L_{n_e} [a strong density gradient stabilization of ETG turbulence was actually found (see Fig. 22 in Ren (2012))]. Furthermore, large profile variations in equilibrium quantities actually may make the contribution from ion-scale turbulence possible (see Fig. 23 in Ren (2012)). When both ion-scale and

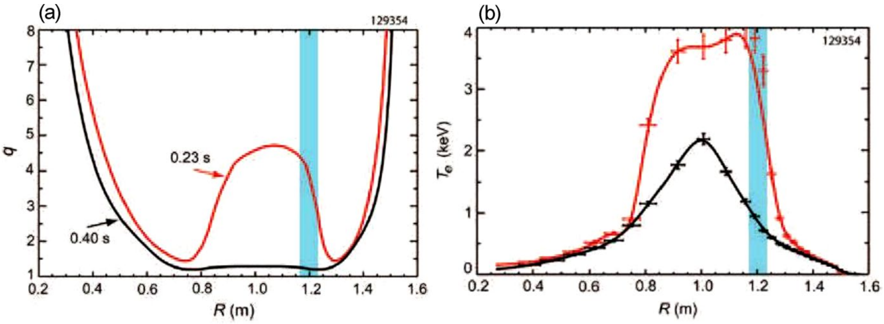

Fig. 43 **a** q Profiles on the equatorial plane with reversed magnetic shear (red) and after the collapse of reversed magnetic shear (black); **b** T_e profiles at the time of reversed shear (red) and after the collapse of reversed magnetic shear (black). The blue rectangle indicates the high-k measurement region. We note that 3 MW of RF heating is turned on at about t=150 ms in this RF-heated NSTX L-mode plasma. Panel a is adapted from Fig. 17 and panel b is adapted from Fig. 18 in Ref. (Mazzucato 2009), with the permission of International Atomic Energy Agency

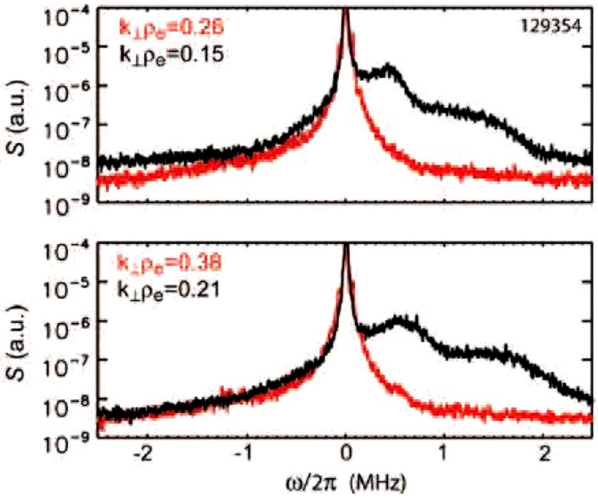

Fig. 44 Electron-scale turbulence wavenumber spectra with reversed shear (t = 0.23 s, red) and after the collapse of reversed shear (t = 0.4 s, black). Measurements were made in an RF-heated NSTX L-mode plasma. The figure is reprinted from Fig. 20 in Ref. (Mazzucato 2009), with the permission of International Atomic Energy Agency

electron-scale instabilities contribute to electron thermal transport, very likely for the cases we are considering there, multi-scale simulations would be needed to address electron-scale fluctuations nonlinearly driven by ion-scale turbulence (Jenko 2004; Maeyama 2015; Howard 2016), which would be measured by the high-k scattering system. Finally, we would like to point out that from what we have observed above, it is unlikely that ETG, ITG, TEM, or MT modes alone would be able to explain the same dependence of confinement scaling on electron collisionality observed in different plasma regimes, and most likely, it is the interplay between these modes (i.e., multi-scale) and also global effect (i.e., profile variation) (Wang 2007; Idomura 2016) which are responsible for the observed confinement scaling.

Magnetic shear dependence: q profile (and magnetic shear) is known to affect tokamak plasma stability and confinement, e.g., forming Internal Transport Barrier (ITB) due to reversed magnetic shear (Kessel 1994; Shirai 1998; Stallard 1999; Akers 2003; ITER Physics Expert Group on Confinement et al. 1999; Connor 2004; Ernst et al. 2004) and improving confinement in a hybrid scenario characterized by a broad region of low magnetic shear (Gormezano 2007), and the ETG mode stability has a strong dependence on $\hat{s}/q$ (seen Eq. 13 (Jenko 2001)). Thus, studying how ETG turbulence depends on q profile and $\hat{s}$ is of great interest. One such study was performed on NSTX where the q profile was varied by changing the current diffusion rate during the early phase of a plasma discharge by adding extra RF heating to heat electrons (thus lowering resistivity) when the plasma current is still diffusing from the edge toward the center, which could lead to the formation of a strong reversed magnetic shear region in the plasma center. This reversed magnetic shear

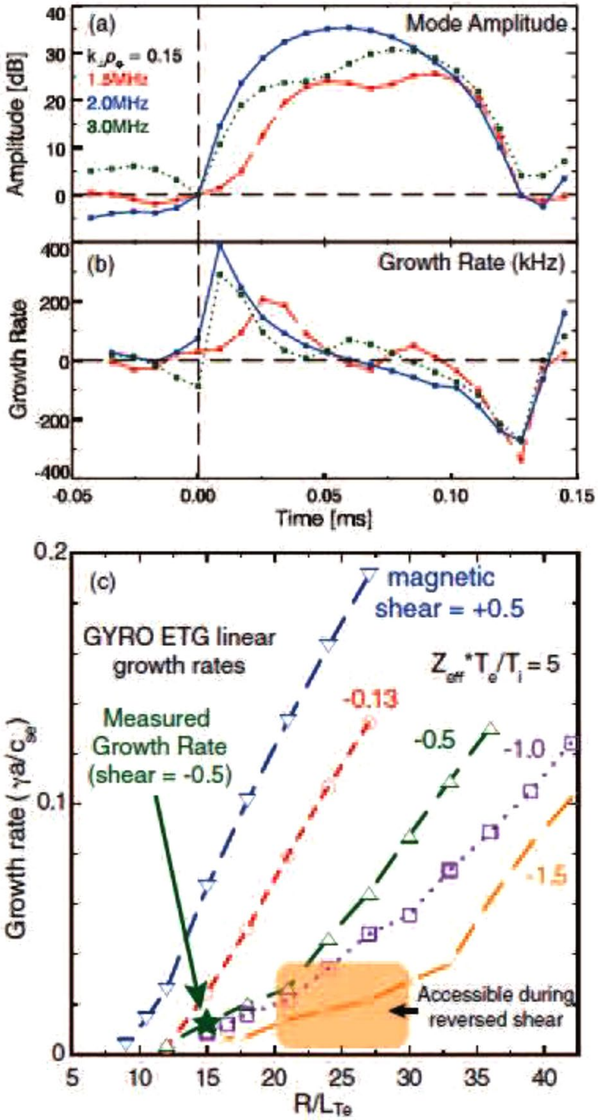

Fig. 45 Time resolved mode amplitude of an ETG burst at three frequencies (**a**) and growth rate corresponding to mode amplitudes (**b**) from analyzing the scattering signal from the high-k scattering system with high time resolution; **c** GYRO computed growth rates, showing sensitivities to variations in magnetic shear and R/L_{T_e}. Experimental data are from NSTX L-mode plasmas with NBI+RF heating and with RF heating only. The star indicates the measured growth rate at $\hat{s} = -0.5$. The figure is from Fig. 2 in Ref. (Yuh 2011). Reprinted with permission from Ref. (Yuh 2011). Copyright (2011) by the American Physical Society

phase is usually self-destructing as plasma stored energy continues to grow, eventually triggering a β-limit-induced MHD instability that drives a fast redistribution of

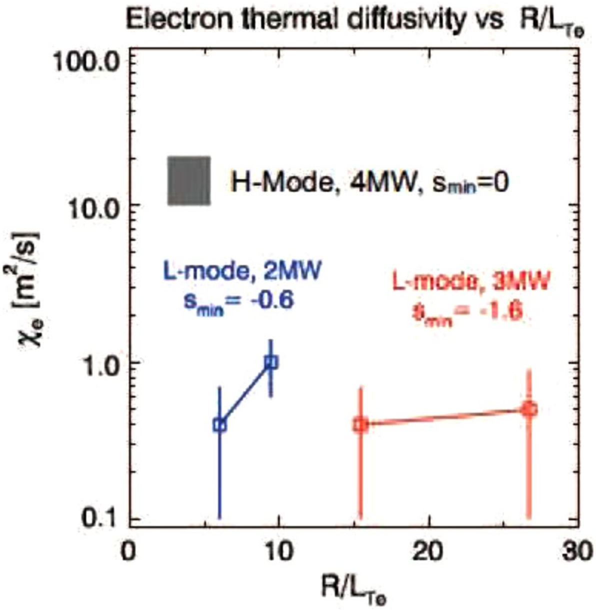

Fig. 46 Electron thermal diffusivities from power balance analysis using the TRANSP code as functions of R/L_{T_e} for two electron ITBs and one typical NSTX H-mode plasma. These electron ITBs show low observed high-k activity at $\rho = r/a = 0.3$ ($R = 120$ cm). The figure is from Fig. 3 in Ref. (Yuh 2011). Reprinted with permission from Ref. (Yuh 2011). Copyright (2011) by the American Physical Society

the plasma current and the flattening of q profile (see Fig. 43a for q profiles with and without reversed magnetic shear). A steep T_e gradient region is developed near the location of minimum q (see Fig. 43b) coupled with significantly reduced χ_e (see Fig. 46 and associated discussions), showing the formation of an electron-ITB (eITB). Figure 44 clearly shows that the electron-scale turbulence is suppressed in the ITB region with reversed magnetic shear (i.e., no obvious off-center frequency spectral peak) and that the electron-scale turbulence appears (shown as frequency spectral peaks at $\omega/2\pi > 0$) after the collapse of reversed magnetic shear. After taking into account a > 80 km s^{-1} plasma co-rotation, the propagation direction of the observed turbulence is in the electron diamagnetic drift direction, consistent with that of the ETG mode. Furthermore, $E \times B$ shear was found to be negligible in the ITB region in RF-heated-only ITB plasmas, where electron-scale turbulence was found suppressed (Yuh 2009), demonstrating that the suppression of electron-scale turbulence can be achieved by reversed magnetic shear alone. These observations strongly suggest that the reversed-magnetic-shear suppression of electron-scale turbulence is responsible for the eITB formation.

The identification of the observed electron-scale turbulence as ETG turbulence is supported by comparisons with results from gyrokinetic simulations (Yuh 2011). With high-temporal-resolution analyses of scattering signals from the high-k scattering system, the amplitude of an electron-scale turbulence burst was temporarily resolved at three different frequencies (see Fig. 45a). The measured turbulence growth rates (derived from Fig. 45a) (see Fig. 45b) were found to occur on the electron sound speed scale (the sound speed

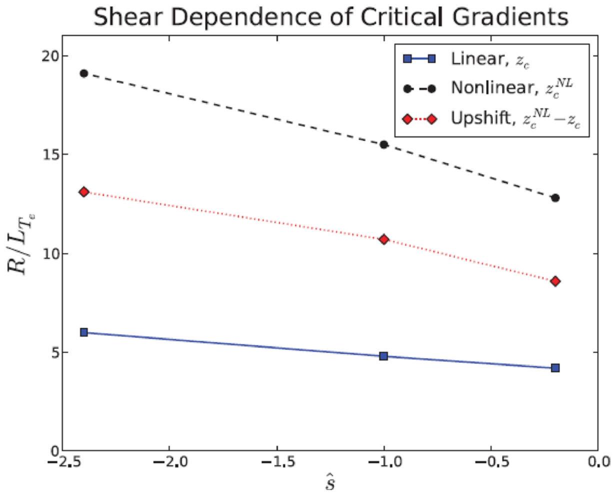

Fig. 47 Critical gradients as a function of magnetic shear, $\tau = 1.8$, where $\tau = Z_{\text{eff}} \frac{T_e}{T_i}$. ETG becomes linearly unstable at gradients above z_c (solid with square). Above z_c^{NL} (dashed with circles), turbulent thermal diffusivities exceed 1 m^2/s. The dotted line with diamonds represents the nonlinear upshift of the critical gradient, $\Delta Z = z_c^{NL} - z_c$. For comparison, the original cyclone ITG test case found an upshift in the critical gradient for transport that extended R/L_{T_i} by 2, from $z_c = 4$ to $z_c^{NL} = 6$ at $\hat{s} = 0.78$ (Dimits 2000). These flux-tube simulations were based on an NSTX eITB L-mode plasma (shot 129354) and simulation parameters were chosen to be roughly consistent with plasma conditions at $r/a \approx 0.4$, the foot of the eITB. The figure is from Fig. 6 in Ref. (Peterson 2012). Reprinted from Ref. (Peterson 2012), with the permission of AIP Publishing

with electron mass), corresponding to a peak growth rate of 400 kHz. We note that the electron sound speed defined in Yuh (2011) should be equivalent to the electron thermal speed. Denoted by a star in Fig. 45c, this peak growth rate is consistent with the linear ETG mode growth rate from a stability calculation with the GYRO code using the same values of R/L_{T_e} and magnetic shear, strongly suggesting that the observed electron-scale turbulence is ETG turbulence.

The suppression of ETG turbulence in eITBs is correlated with significant reductions in χ_e (see Fig. 46). Compared with a typical NSTX H-mode plasma, a more-than-an-order-of-magnitude reduction in χ_e is seen in the two eITB cases with $\hat{s} = -0.6$ and -1.6. Furthermore, the $\hat{s} = -1.6$ case shows that χ_e has a weak dependence on R/L_{T_e} above ETG linear stability, while the $\hat{s} = -0.6$ case shows that χ_e increases modestly with R/L_{T_e}. It is noted that an increase in ETG bursts accompanies the increase in χ_e with R/L_{T_e}, consistent with the ETG-driven electron thermal transport.

With the GYRO code, both local and global nonlinear gyrokinetic simulations of these reversed shear plasmas were carried out as reported in Peterson (2012) and Peterson (2011). A strongly upshifted nonlinear critical gradient for thermal transport that depends on magnetic shear was identified with local simulations (see Fig. 47). For all magnetic shear used, it is shown that the upshift in the nonlinear critical gradient (z_c^{NL}) from the linear one (z_c) becomes stronger as the $\hat{s}$ becomes more negative, e.g., from 9 at $\hat{s} = -0.2$ to 13 at $\hat{s} = -2.4$. It is speculated that this observed upshift in the critical T_e gradient for ETG turbulence is due to zonal flows, like the Dimits shift seen for ITG turbulence (Peterson 2011). We think that the occurrence of this upshift in the critical T_e gradient is consistent with the preferential generation of zonal flows with weak/negative magnetic shear seen in the studies of zonal flow dependence on magnetic shear shown in Sect. 2.2.3 (e.g., see Idomura (2005) and Li (2005)). Global simulations indicate that strongly negative magnetic shear may suppress ETG turbulence which is consistent with the formation of eITB. The global simulations also show that ETG turbulence cannot propagate past the barrier into the plasma interior, while the ETG-turbulence-driven thermal flux is large enough to be experimentally relevant at the outer edge of the barrier. We note that suppression of ETG turbulence with negative magnetic shear has also been shown in global gyrokinetic simulations with less realistic tokamak geometry (Idomura 2000a, 2005), which is also consistent the formation of eITB. However, we note that these global simulations do not include the consistent evolution of MHD equilibrium (e.g., q-profile) and plasma temperature and density profiles, and thus, do not directly model the process of self-organized formation of eITB.

Validation of the local gyrokinetic model of the ETG mode through spectral comparison: As we have pointed out, there are different levels of validation and electron-scale turbulence measurements are expected to provide extra constraints to the validation. Indeed, the studies presented above have demonstrated the correlation between electron-scale turbulence and experimental/predicted electron thermal transport and agreements of parametric dependence of measured turbulence with that of the ETG mode. These comparisons often use total measured fluctuation levels requiring an integration over frequency and/or wavenumber, or the spectral power of one particular wavenumber or the peak spectral power of the measured frequency/wavenumber spectra. However, spectral characteristics, e.g., spectral shape, of the measured turbulence spectra are either lost due to integration or simply ignored in these comparisons. We note that comparing spectral characteristics with numerical simulations has a high demand on turbulence diagnostics, particularly the localization of measurements which is essential to such comparisons with local gyrokinetic simulation predictions. A line-integrated measurement over a large portion of plasma volume would be very difficult to simulate with gyrokinetic codes, particularly for the ETG mode if not impossible with the present computational power. Given this constraint on diagnostics, two diagnostics presented in Sect. 3.2.1 are obviously outstanding, one being the UHR ES scattering system on FT-2 tokamak and the other being the high-k scattering system on NSTX. Indeed, both of them have provided the latest validation of ETG turbulence in terms of comparing predicted spectra with those from experiments (Ruiz 2019; Janhunen 2021). Here, we review some results from Ruiz (2019) which is a great example of how gyrokinetic simulations coupled with a synthetic diagnostic can greatly improve the understanding of diagnostic measurements and the physics underlying electron thermal transport. In addition, it lays out a validation workflow with measured turbulence spectra included as a validation metric, which significantly raises the fidelity of validated models and numerical codes.

A synthetic diagnostic for the high-k scattering system on NSTX was developed to facilitate such a comparison (Ruiz 2019). The synthetic diagnostic takes simulated turbulence data and computes the scattering signal seen by each scattering channel using the principle of coherent scattering. In the time domain and physical space, the synthetic time-space density fluctuation for a particular scattering channel measuring the wavenumber $\vec{k}_+$ ($\vec{k}_+$ is the scattering wavenumber that satisfies the Bragg condition, $\vec{k}_+ = \vec{k}_s - \vec{k}_p$), $\delta n_u(\vec{k}_+, t)$, can be written as

$$\delta n_u(\vec{k}_+, t) = \int_{V_s} d^3\vec{r'}\delta n^{GYRO}(\vec{r'}, t)U(\vec{r'})e^{-i\vec{k}_+\cdot\vec{r'}}, \tag{19}$$

where $(\vec{r'}, t)$ denotes the spatial–temporal dependence, $\delta n^{GYRO}(\vec{r'}, t)$ represents the density fluctuation from a nonlinear GYRO simulation, and $U(\vec{r'})$ is an effective real space filter of fluctuations delimiting the scattering volume, normally taken as Gaussian to be consistent with the Gaussian profile of the probe beam. Note that given the $e^{-i\vec{k}_+\cdot\vec{r'}}$ term in the integrand, the integration over the scattering volume in Eq. 19 is essentially a spatial Fourier transform of $n^{GYRO}(\vec{r'}, t)U(\vec{r'})$ where $U(\vec{r'})$, from the point of view of wavenumber space, determines the wavenumber resolution of $\delta n_u(\vec{k}_+, t)$. The integration in Eq. 19 is three-dimensional over the whole scattering volume. However, using a 2D approximation, the integration is carried out in a 2D toroidal slice, assuming a good toroidal localization of the high-k scattering system (Ruiz 2019) (see Ruiz (2020) for more details). A temporal Fourier analysis of $\delta n_u(\vec{k}_+, t)$ gives the frequency spectral power density $S(\vec{k}_+, f)$ for each scattering channel, and integrating over frequency results in the wavenumber spectral power density $S(\vec{k}_+)$. Simulation-wise, it is found that the conventional simulation box size [e.g., $4.5\rho_s \times 4\rho_s$ (radial size×poloidal size)], for the ETG mode, cannot accommodate the size of the probe/scattered beams, and thus, “big-box” (e.g., $20\rho_s \times 20.6\rho_s$) simulations were also carried out for the sole purpose of comparing with the high-k scattering system. Note that these “big-box” simulations still do not completely resolve ion-scale dynamics spatially and temporally (thus cannot be considered as multi-scale as those presented in Maeyama (2015) and Howard (2014)), and are essentially the same as electron-scale simulations with conventional simulation box size in terms of numerical convergence and the ETG mode physics. Since a “big-box” simulation costs a lot more computational power, most parametric scans were carried out with electron-scale simulations with small box sizes, and “big-box” simulations were carried out with the guidance of these parametric scans. The target NSTX plasmas were those reported in Ruiz (2015), where nonlinear stabilization of ETG turbulence is identified as a result of the steepening in the electron density profile due to a current ramp-down. Heat flux matching of experimental values within experimental uncertainties is achieved with nonlinear gyrokinetic simulations using the GYRO code by varying a variety of parameters within experimental uncertainties. Particularly, before the current ramp-down (the strong ETG drive case), heat flux matching is achieved with a combination of 1σ (25%) increase in ∇T_e, 10% decrease in q, and 20% increase in $\hat{s}$ or a combination of 1σ (50%) decrease in ∇n_e, 10% decrease in q, and 20% increase in $\hat{s}$, demonstrating the sensitivity of experimental results on q and $\hat{s}$; After the current ramp-down (the weak ETG drive case), heat flux matching is achieved with a combination of 1σ (20%) increase in ∇T_e, and 1σ (30%) decrease in ∇n_e. A detailed analysis shows that comparisons between synthetic frequency spectra with those from high-k scattering measurements do not provide reliable validation metrics in discriminating different simulations due to the overwhelming dependence of the location of frequency spectral peaks of scattering signal spectra on the Doppler shift and the overwhelming dependence of the spectral width of frequency spectral peaks on the high-k scattering system wavenumber resolution and the Doppler shift. However, a comparison between synthetic wavenumber spectra and those from the high-k scattering system proves to be a much better validation metric (see Fig. 48). Figure 48a and b shows that with the nominal (base) parameter (Fig. 48a) or a combination of 1σ (25%) increase in ∇T_e and 1σ (50%) decrease in ∇n_e (Fig. 48b), gyrokinetic simulations cannot match either the electron heat flux or the $k_\perp$ spectral shape. On the other hand, Fig. 48c and d shows that as the electron heat flux is matched with different parameter variations, different degrees of $k_\perp$ spectral shape matching are realized with the best spectral shape matching shown in Fig. 48d with a combination of 1σ (50%) decrease in ∇n_e, 10% decrease in q, and 20% increase in $\hat{s}$. Furthermore, there could be cases where matching is reasonable

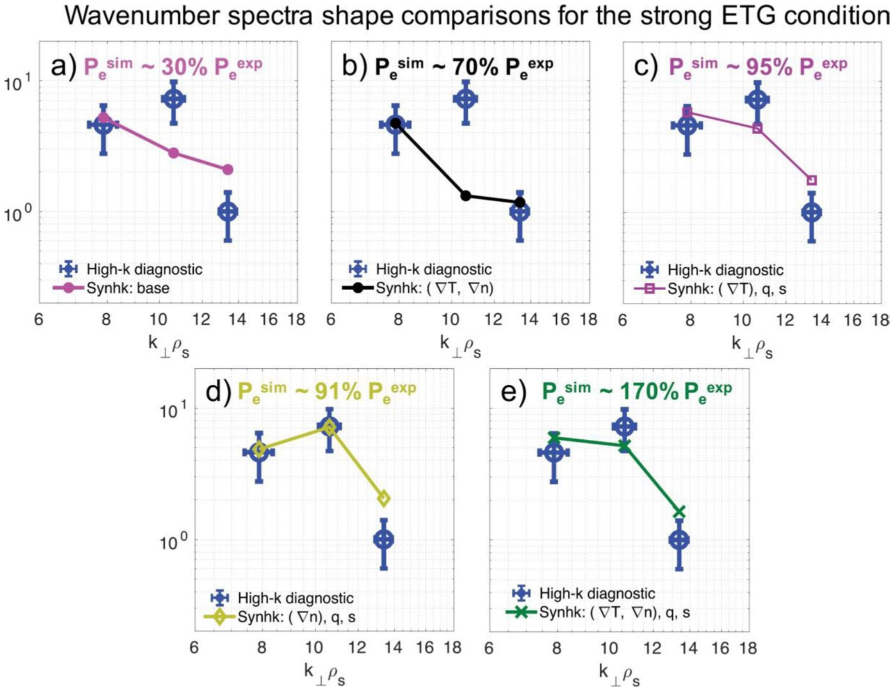

Fig. 48 Comparisons of spectral shape between the experiment and those from five “big-box” electron-scale simulations for the strong ETG drive case: **a** for the simulation with base parameters; **b** for the simulation with 1σ scaled ∇T_e (+25%) and ∇n_e (– 50%); **c** for the simulation with 1σ scaled ∇T_e (+25%) and scaled q (– 10%) and $\hat{s}$ (+20%); **d** for the simulation with 1σ scaled ∇n_e (-50%), and scaled q (– 10%) and $\hat{s}$ (+20%); **e** for the simulation with 1σ scaled ∇T_e (+25%) and ∇n_e (– 50%), and scaled q (– 10%) and $\hat{s}$ (+20%). Experimental measures were made in an NSTX NBI-heated H-mode plasma with $B_T = 5.5$ kG and I_p of about 1 MA. The figure is reprinted from Fig. 12 in Ref. (Ruiz 2019). © IOP Publishing. Reproduced with permission. All rights reserved

for the $k_\perp$ spectral shape but not for electron heat flux (see Fig. 48e). However, just comparing $k_\perp$ spectral shape does not take into account the absolute spectral density available from simulations, e.g., the cases shown in Fig. 48c and d with good matches of both electron heat flux and spectral shape having a factor of 2–3 in difference in absolute spectral density. Thus, another metric involving absolute spectral density is needed. Since the high-k scattering system is not absolutely calibrated, the ratio between spectral densities at two different time points is chosen to serve as another validation metric. An obvious choice is the ratio between the spectral density of the strong ETG drive cases and that of the only heat flux-matched "big-box" simulation for the weak ETG drive. Particularly, due to large variations in this ratio (up to two orders of magnitude in parametric scans), the logarithmic value of this ratio is used to evaluate the validation metric. Following Refs. Ricci (2011) and Holland (2016), the validation metrics are defined using quantities, $\mathbf{d_X}$ and $\mathbf{R_X}$:

$$\mathbf{d_X} = \sqrt{\frac{(\mathbf{X}^{exp} - \mathbf{X}^{sim})^2}{\delta(\mathbf{X}^{exp})^2 + \delta(\mathbf{X}^{sim})^2}}, \tag{20}$$

$$\mathbf{R_X} = \frac{1 + \tanh((\mathbf{d_X} - \mathbf{d_0})/\lambda)}{2}, \tag{21}$$

where $d_0 = 1.5$ and $\lambda = 0.5$ are used as in Refs. Ricci (2011) and Holland (2016), $\mathbf{X}$ represents observables, i.e., the electron heat flux ($\mathbf{P_e}$), the $k_\perp$ spectral shape [$\mathbf{S}(\mathbf{k_i})$ with $\mathbf{k_i}$ representing the wavenumber of each diagnostic channel ($\mathbf{i}$=1, 2, 3)], and the spectral density ratio ($\log_{10}(\langle \mathbf{S}(\mathbf{k_i})\rangle^{strongETG} / \langle \mathbf{S}(\mathbf{k_i})\rangle^{weakETG}$) with $\langle \mathbf{S}(\mathbf{k_i})\rangle = \sum_i S(k_i)/3$). Note that a value of 0 in $\mathbf{R_X}$ denotes perfect agreement, while a value of 1 means complete disagreement. Since the high-k scattering system is not absolutely calibrated, the measured spectral density of each scattering channel is scaled with the same free parameter C to calculate $\mathbf{d_S}(\mathbf{k_i})$, and C and $\mathbf{d}_{\mathbf{shape}_{C,min}}$ are determined by minimizing the least-squares distance, $\mathbf{d_{shape}} = \sqrt{\sum_i \mathbf{d}^2_{\mathbf{shape(i)}}}$. Applying the above validation metrics to "big-box" electron-scale simulations coupled with a composite metric using $\mathbf{R_X}$ from each validation metric, it is determined that simulations presented in Fig. 48c and d offer the best overall agreement between the experiment. Comparisons of synthetic $k_\perp$ spectra of both the strong ETG drive case and the weak ETG drive case with those from the high-k scattering system are shown in Fig. 49, where a good agreement between the experiment can be seen. These results strongly suggest that ETG turbulence is responsible for the observed electron thermal transport in both the strong and weak ETG drive cases. Thus, we can see that being able to match both turbulence measurement and observed electron heat flux demonstrates the high fidelity of the numerical code used and the underlying physics model.

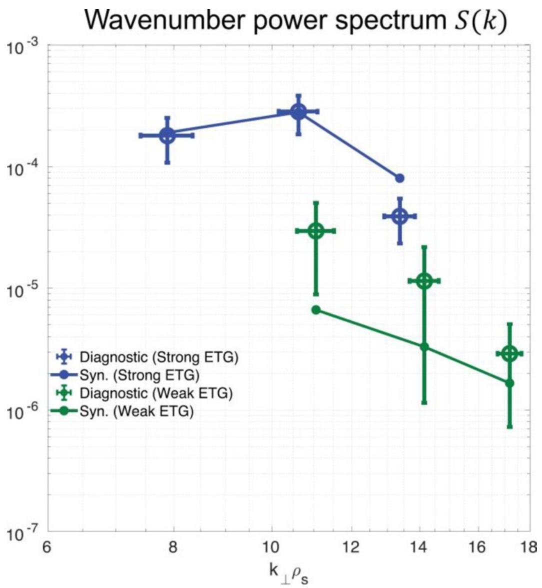

Fig. 49 Comparisons of synthetic $k_\perp$ spectra of both the strong ETG drive case and the weak ETG drive case with those from high-k scattering system. The synthetic $k_\perp$ spectrum for the strong ETG drive case is from Fig. 48d where simulated electron heat flux is matched to 91% of the experimental value, and the synthetic $k_\perp$ spectrum for the weak ETG drive case is from the only heat flux-matched "big-box" electron-scale simulation for the case. The experimental $k_\perp$ spectrum for the strong ETG drive case is scaled with a constant to minimize the least-squares distance between experimental and simulated spectra. The same constant is applied to the experimental $k_\perp$ spectrum for the weak ETG drive case to preserve the relative fluctuation level between the two ETG drive cases. Experimental measures were made in an NSTX NBI-heated H-mode plasma with $B_T = 5.5$ kG and I_p of about 1 MA. The figure is reprinted from Fig. 14 in Ref. (Ruiz 2019). © IOP Publishing. Reproduced with permission. All rights reserved

4 The ETG mode in the H-mode pedestal region

Due to the importance of the H-mode pedestal region in determining the overall energy confinement (ITER Physics Expert Group on Confinement et al. 1999; Doyle 2007), studying the roles of the ETG mode in driving electron transport is of great interest, particularly given the experiment-relevant electron thermal transport driven by the ETG mode demonstrated in the plasma core region in prior sections. We note that although the ETG theories we reviewed in Sect. 2 are still largely applicable to the pedestal region, the ETG mode in the pedestal region has been shown to have distinct features in contrast to its core counterpart (Told 2008, 2012; Jenko 2009; Kotschenreuther 2019; Parisi 2020) due to the distinct parametric regime of the H-mode pedestal. In particular, in contrast to the core region (of either L- or H-mode), the edge region in H-mode plasmas is featured by much lower temperatures (thus much higher collisionality), very steep gradient, e.g., more than an order magnitude larger in temperature/density gradient, extreme plasma shaping (e.g., large global magnetic shear), and strong up–down asymmetry. Furthermore, due to the extremeness in the pedestal parametric regime, numerical simulations, particularly nonlinear simulations, require significant computational resources compared with simulations based on core parameters (Parisi 2020), and only more recently, nonlinear gyrokinetic simulations of ETG turbulence in the pedestal steep-gradient region have been carried out (Jenko 2009; Told 2012; Hatch 2015, 2016, 2017; Kotschenreuther 2017, 2019; Guttenfelder 2021). We note that due to the same reason, multi-scale simulations (like those based on core parameters we reviewed in Sect. 2.2.5 (Maeyama 2015, 2017b; Howard 2014, 2015, 2016; Holland 2017)) in the pedestal region have yet been accomplished to elucidate the effects of cross-scale interaction on edge plasma transport. Thus, we feel that devoting a separate section to this important topic is appropriate. Here, we start with discussions of the effects of steep gradients on the linear stability of the edge ETG mode and the resulting distinct features by applying theories reviewed in Sect. 2 and new insights into the toroidal ETG mode in the steep-gradient regime (Parisi 2020). We will then discuss the contribution of ETG turbulence to electron transport by reviewing edge nonlinear gyrokinetic simulations (Jenko 2009; Told 2012; Hatch 2015, 2016, 2017; Kotschenreuther 2017, 2019; Guttenfelder 2021). Finally, we will present some experimental evidence of ETG turbulence in the H-mode pedestal region.

4.1 The ETG mode linear characteristics in the H-mode pedestal region

The most obvious difference in equilibrium profiles in the pedestal region is the large normalized gradients compared to those of the typical core region. For example, $a/L_{T_e} \approx 30$ and $a/L_{n_e} \approx 25$ at $\rho = 0.97$ (ρ is the square root of normalized toroidal flux) in an ASDEX Upgrade H-mode plasma (Hatch 2015) and $a/L_{T_e} \approx 60$ and $a/L_{n_e} \approx 50$ at $\Psi_N = 0.97$ (Ψ_N is the normalized poloidal flux) in a DIII-D H-mode plasma (Guttenfelder 2021), in contrast to typical core parameters of a/L_{T_e} and $a/L_{n_e} \sim 1$–5. We note that the only core scenario that could have somewhat closer a/L_{T_e} is e-ITBs with steep T_e gradient, and, however, a/L_{n_e} is usually still much smaller, e.g., $a/L_{T_e} \sim 13$–20 with $a/L_{n_e} \sim 1$ in NSTX reversed shear L-mode plasmas (Yuh 2009, 2011; Peterson 2012, 2011) (and see Sect. 3.2.2 for more discussion on ETG turbulence in e-ITBs), and $a/L_{T_e} \sim 14$ with $a/L_{n_e} \sim 7$ in JT-60U reversed shear plasmas (Fujita 1997). In comparison, smaller a/L_{T_e} are also found in other ITBs, e.g., $a/L_{T_e} = 4.1$ with $a/L_{n_e} = 3.4$ in the ITB in DIII-D high β_p (poloidal β) plasmas (Jian 2019; Ding 2019), and $a/L_{T_e} \sim 6$ in the e-ITB in ASDEX Upgrade reversed shear plasmas with counter electron cyclotron current drive (Wolf 2001). As we have shown in Sect. 2, with a large normalized density gradient the ETG mode stability boundary is determined by η_e as seen in Fig. 3 (i.e., $\eta_e > 2/3$ without FLR heat flux and $\eta_e > 1$ with FLR heat flux for instability) and Eq. 13 (i.e., $\eta_e > 0.8$ for instability). We note that this is different from NSTX e-ITB cases discussed in Sect. 3.2.2 (Yuh 2009, 2011; Peterson 2012, 2011) where the ETG mode stability boundary is determined by normalized T_e gradient set by negative magnetic shear (i.e., $R/L_{T_e} > 12 \pm 2$ for instability with magnetic shear from −2.4 to -1). Thus, an η_e threshold, $\eta_{e,\mathrm{crit}}$, has to be satisfied in the pedestal region due to a typically large normalized density gradient in order for the ETG mode to be unstable, implying a correspondingly large normalized temperature gradient. Indeed, $\eta_{e,\mathrm{crit}} = 1.2$, 1.5 for the ETG mode has been found through linear gyrokinetic stability analysis (Jenko 2009;

Hatch 2015; Guttenfelder 2021), and $\eta_e \sim 1$–2 has often been seen in the steep-gradient part of the H-mode pedestal region. We note that $\eta_{e,crit}$ for the ETG mode has been validated with experiment and linear gyrokinetic simulations with core-relevant parameters (see Ren (2011) and Ren (2012) and also Sect. 3.2.2). Bearing the importance of $\eta_{e,\mathrm{crit}}$ in mind, we can discuss the effects of a large normalized density gradient on the ETG mode linear growth rate spectrum. From Eqs. 24 and 25 in Horton (1988), we can see that the maximum linear growth rate occurs at the wavenumber, $k_m = \{[1 - 2\epsilon_n(1 + 2\Gamma\tau)]/[\tau(1 + \eta_e) + 2\Gamma\tau\epsilon_n]\}^{1/2}/\rho_{ei}$, and the maximum linear growth rate $\gamma_m \simeq k_m(2\epsilon_n\tau)^{1/2}(\eta_e + 1 - \Gamma)^{1/2}(v_{ei}/L_n)$, where $\epsilon_n = L_n/R$, $\tau = T_e/T_i$, ρ_{ei} is electron gyroradius with ion temperature, and (v_{ei} is the electron thermal velocity with ion temperature. It can be seen that as normalized density gradient increases (i.e., decreased ϵ_n) with fixed η_e (to ensure η_e is above ETG stability boundary in η_e), k_m increases but remains less than $1/(\rho_{ei})$. Since $\gamma_m \propto k_m/\sqrt{L_n}$, γ_m also increases with an increased density gradient. Thus, with a fixed η_e, a larger normalized density gradient would increase the maximum linear growth rate and push the maximum linear growth rate toward higher wavenumbers. This trend can be clearly seen in pedestal linear gyrokinetic simulations (Told 2008, 2012; Parisi 2020; Guttenfelder 2021). Another effect of a large normalized density gradient is that ion response is increasingly non-adiabatic and may need to be treated kinetically (Singh 2013). The argument is that since electron diamagnetic frequency, $\omega_{*e} = k_y v_{th,e}\rho_e/L_n$, would increase with increased density gradient (smaller L_n), the perpendicular wave phase velocity, $\omega/k_\perp \sim v_{\mathrm{th},e}\rho_e/L_n$ with $\omega \sim \omega_{*e}$ could approach ion thermal velocity with typical edge L_n values, particularly for impurity ions which have much lower thermal velocity than main ions, and wave–particle resonance needs to take into account. Non-adiabatic ion responses have been derived with drift kinetic equation assuming unmagnetized ions, resulting in an ETG-driven inward particle pinch that, argued by the authors, could be relevant to the formation of the H-mode density pedestal (Singh 2013).

The steep electron temperature profile is another prominent feature of the H-mode pedestal region, and we emphasize that it is the large T_e gradient that makes the ETG mode relevant in the pedestal region by keeping η_e above $\eta_{e,\mathrm{crit}}$. Important ETG mode features resulting from large T_e gradient are: the ETG mode extends into ion scale, i.e., $k_y\rho_i < 1$; the most unstable mode for a particular k_y may require a finite radial wavenumber, k_x, i.e., $\theta_0 = k_x/(\hat{s}k_y) \neq 0$ (Told 2008, 2012; Parisi 2020) and the mode structure peaks away from the outer mid-plane of the tokamak geometry; the ETG mode could be driven far from the outer mid-plane even with $k_x = 0$ (Parisi 2020). The peaking location of the linear ETG mode found in the pedestal region renders early linear analytical theories for the electrostatic ETG mode (applicable for typical core parameters) insufficient due to the assumption that the mode structure peaks around the outer mid-plane (Horton 1988; Dong 2002, 2003) (although the basic destabilizing mechanism still applies). Addressing this issue, Parisi et al. Parisi (2020) present an analytical theory for a new type of toroidal ETG mode ["toroidal" means driven by the usual coupling between T_e gradient and magnetic gradient and curvature drifts as discussed in (Horton 1988)] characterized by ion-scale binormal wavenumbers ($k_y\rho_i < 1$) and large radial wavenumbers (beyond the ρ_i scale) at the mode structure peaking location that is away from the outer mid-plane (Parisi 2020) and explain how the large normalized T_e gradient leads to the particular features of this kind of toroidal ETG mode.

To explain their findings, we first start with the toroidal ETG mode using field-aligned coordinates (x, y, θ), where $x = q_c/(r_c B_a)(\Psi(r) - \Psi(r_c))$ is the local flux-surface label defined around a flux surface labeled by r_c (r is the flux surface label, $q_c = q(r_c)$, and B_a is the toroidal magnetic field strength evaluated at the outer mid-plane location of the flux surface labeled by r_c), $y = 1/B_a(\partial\Psi/\partial r)|_{r_c}\alpha$ is the binormal coordinate and field line label [$\alpha = \zeta - q\theta + \nu(r, \theta)$, where $\nu(r, \theta)$ is a function of 2π period in θ (for its definition, see Eq. 10 in Parisi (2020))], and θ is the poloidal angle used as parallel coordinate ($\theta = 0$ corresponding to the outer mid-plane). A single (k_x, k_y) Fourier mode can be generically written as $g(k_x, k_y, \theta)$ in this field-aligned coordinate system. Following the mode from $\theta = 0$ in real space, the local radial wavenumber at θ can be written as $K_x(\theta) = k_x - k_y(\hat{s}\theta - (r/q)\partial\nu/\partial r)$, although except for the $k_y(\hat{s}\theta$ term other terms in this expression are not important for our discussion below. Note that $K_x(\theta)$ increases with θ without bound due to the continuous twist of magnetic field lines by magnetic shear, and eventually its contribution to $k_\perp$ would dominate. For the toroidal ETG mode to be unstable, the driving frequency, $\omega_{*e}\eta_e$, must be of the same order as the magnetic drift frequency, $\vec{V}_{Me} \cdot \vec{k}_\perp \sim k_\perp v_{th,e}^2/\Omega_e R_0$, where $\vec{V}_{Me} = \frac{\vec{b}}{\Omega_e} \times [(v_{||}^2 + v_\perp^2/2)\nabla lnB + v_{||}^2(4\pi)/(B^2)(\partial p_0/\partial r)\nabla r]$ is the magnetic drift velocity ($\vec{b}$ is the unit vector of the magnetic field, Ω_e is the electron gyro-frequency, $v_{||}$ is the electron parallel velocity with respect to $\vec{b}$, $v_\perp$ is the perpendicular velocity, $p_0 = \sum_s p_{0s}$ is the total pressure, and $p_{0s} = n_{0s}T_{0s}$ is the lowest order pressure for a particular species s). Note that $\omega_{*e}\eta_e$ is the result of energy release from destabilizing temperature gradient and $\vec{V}_{Me} \cdot \vec{k}_\perp$ is the result of stabilizing perpendicular compression. Thus, we have $\omega_{*e}\eta_e/\vec{V}_{Me} \cdot \vec{k}_\perp \sim (k_y/L_{T_e})/(k_\perp/R_0) \sim 1$. When $\hat{s}\theta$ is large enough, $K_x(\theta) \approx -k_y\hat{s}\theta$, and thus, $k_\perp \approx |K_x| = k_y|\hat{s}\theta|$. As a result, $\omega_{*e}\eta_e/\vec{V}_{Me} \cdot \vec{k}_\perp \sim (R_0/L_{T_e})/|\hat{s}\theta| \sim 1$, meaning that since $R_0/L_{T_e} >> 1$, this type of toroidal ETG mode is being driven at a large ballooning angle, i.e., $\hat{s}\theta >> 1$, where the coupling between T_e gradient and magnetic drift is strongest. On the other hand, for the mode not to be severely FLR damped, it requires that $k_\perp\rho_e \approx K_x\rho_e \approx k_y\rho_e|\hat{s}\theta| \sim 1$, giving $|\hat{s}\theta| \sim 1/(k_y\rho_e)$. Combining the two relations both involving $|\hat{s}\theta|$, we have $k_y\rho_e \sim L_{T_e}/R_0 << 1$ with large normalized T_e gradient. With steep pedestal T_e profiles having $R_0/L_{T_e} \gtrsim \rho_i/\rho_e$, we see that for this off-mid-plane-driven toroidal ETG mode, $k_y\rho_i \lesssim 1$, demonstrating that the ETG mode can be unstable even with k_y in the ion scale. Linear gyrokinetic simulations in the steep T_e gradient region in the H-mode pedestal support this conclusion (Told 2008, 2012; Parisi 2020; Guttenfelder 2021) (see Fig. 50). In particular, the upper panel of Fig. 50 shows that unstable toroidal ETG mode extends down to $k_y\rho_s$ of about 0.2 (i.e., $k_y\rho_e \approx 0.0033$ with deuterium) and the lower panel of Fig. 50 shows that the toroidal ETG mode extends down to $k_y\rho_i$ of about 0.15 (i.e., $k_y\rho_e \approx 0.002$ with deuterium), which are comparable with $L_{T_e}/R \sim 100$ (upper panel) and $L_{T_e}/R_0 = 130$ (lower panel) according to $k_y\rho_e \sim L_{T_e}/R_0 << 1$. A similar argument can be applied to the slab ETG mode by balancing $\omega_{*e}\eta_e$ with the electron transit frequency, $k_{||}v_{th,e}$ (Parisi 2020), which shows that large normalized T_e

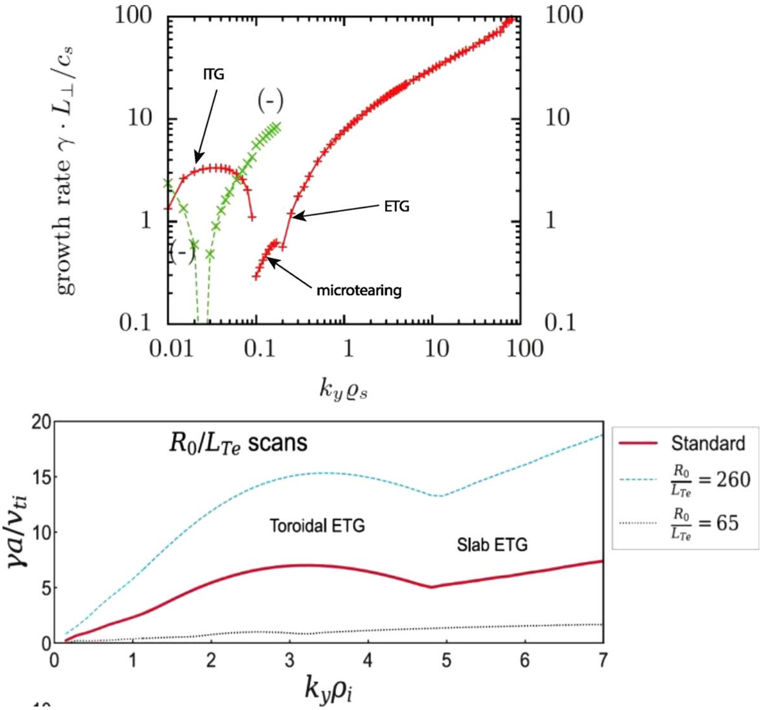

Fig. 50 Upper panel: k_y spectra of real frequency (green cross) and linear growth rate (red plus) for the most unstable mode (among a range of k_x) from ion to electron scales calculated for an ASDEX Upgrade H-mode plasma at $\rho_{\text{tor}} = 0.98$ (ρ_{tor} is the square root of normalized toroidal flux). (–) denotes negative frequency (electron diamagnetic direction). Real frequencies of ETG modes are not shown due to insufficient accuracy in determining it due to the limited number of scans in k_x for each k_y. ITG-like modes exist in the $k_y\rho_s$ range of ~ 0.01 to 0.08 and microtearing modes exist from $k_y\rho_s \sim 0.10$ to 0.18. ETG modes extend from $k_y\rho_s \sim 100$ down to 0.2. The upper panel is adapted from Fig. 16 in Ref. (Told 2008). Reprinted from Ref. (Told 2008), with the permission of AIP Publishing. Lower panel: k_y spectra of linear growth rate with $k_x = 0$ for three R_0/L_{T_e} values for a JET H-mode plasma at $r/a = 0.9743$. Note that toroidal ETG modes range from $k_y\rho_i \sim 5$ down to 0.15 and slab ETG modes are most unstable in $k_y\rho_i >$ 5. Standard case is with $R_0/L_{T_e} = 130$, $R_0/L_{T_i} = 34$, $R_0/L_n = 31$. Strong dependence of linear growth rates on R_0/L_{T_e} is evident. The lower panel is adapted from Fig. 7 in Ref. (Parisi 2020), with the permission of International Atomic Energy Agency

gradients, $R_0/L_{T_e} >> 1$, also shift the slab ETG mode to smaller k_y. The lower panel of Fig. 50 also shows that the toroidal ETG mode is most unstable in $k_y\rho_i < 5$, while the slab ETG mode becomes the dominant one in $k_y\rho_i > 5$, and both modes are strongly driven by ETG.

The off-mid-plane peaking feature of the mode structure of the ETG mode in the H-mode pedestal region can be seen in Fig. 51, where Fig. 51a shows k_y spectra of linear growth rate with $\theta_0 = 0$ and 0.5 for the same JET H-mode plasma at $r/a = 0.9743$ and mode structures for $k_y\rho_i = 2.4$ and 51.4 for the two θ_0s are shown in Fig. 51(b) ($\theta_0 = 0$) and (c) ($\theta_0 = 0.5$) (Parisi 2020). Note that the $\theta_0 = 0$ case in Fig. 51a is the same case as shown in the lower panel of Fig. 50 but in a wider

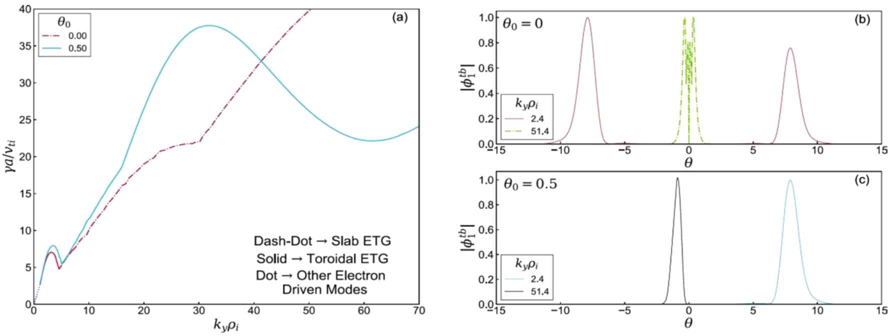

Fig. 51 **a** k_y spectra of linear growth rate for two θ_0s. **b** Mode structure for $k_y\rho_i = 2.4$ (red solid line) and 51.4 (green dashed line) with $\theta_0 = 0$. **c** Mode structure for $k_y\rho_i = 2.4$ (cyan solid line) and 51.4 (black solid line) with $\theta_0 = 0.5$. These simulation results are for a JET H-mode plasma at $r/a = 0.9743$. The figure is reprinted from Fig. 4 in Ref. (Parisi 2020), with the permission of International Atomic Energy Agency

k_y range. With the same as seen in the lower panel of Fig. 50, there is the transition from the toroidal ETG mode to the slab ETG mode from $k_y\rho_i < 5$ to larger k_y, while for the $\theta_0 = 0.5$ case, the toroidal ETG mode remains the most unstable mode throughout the whole k_y range (note that k_x is related to k_y through $\theta_0 = k_x/(\hat{s}k_y)$). Clear off-mid-plane peaking mode structure for a toroidal ETG mode at $k_y\rho_i = 2.4$ with $\theta_0 = 0$ is seen in Fig. 51b, while a slab ETG mode at $k_y\rho_i = 51.4$ has mode structure centered around the outer mid-plane (note that $\theta = 0$ corresponds to the outer mid-plane). The observation that the mode structure of the toroidal ETG mode at $k_y\rho_i = 2.4$ peaks far from $\theta = 0$ is consistent with the required large θ driven location of the toroidal ETG mode from the constraint that $(R_0/L_{T_e})/|\hat{s}\theta| \sim 1$ when $R_0/L_{T_e} >> 1$. With a finite $\theta_0 = 0.5$, off-mid-plane peaking in the mode structure can be seen in Fig. 51c, where the θ peaking location of the toroidal ETG mode at $k_y\rho_i = 2.4$ is not affected, while the most unstable mode at $k_\theta\rho_i = 51.4$ is now a toroidal ETG mode peaking at a small negative θ (note that the slab ETG mode dominates at $k_\theta\rho_i = 51.4$ for the $\theta_0 = 0$ case). The transition from the toroidal ETG mode to the slab ETG mode with $\theta_0 = 0$ seen in Figs. 50b and 51a is due to the fact that as $k_y\rho_i$ increases, the toroidal ETG mode becomes increasingly FLR damped as $k_\perp\rho_e \approx |K_x\rho_e| = k_y\rho_e|\hat{s}\theta|$ becomes significantly larger than 1 and that FLR damping for the slab ETG mode is much weaker, since its eigenfunction centers around $\theta = 0$ within a small θ range (see Fig. 51b). Seeing $k_\perp\rho_e \approx k_y\rho_e|\hat{s}\theta|$, one may think that it is possible to have toroidal ETG modes with higher $k_y\rho_e$ being driven at smaller θ to reduce the FLR damping of these higher-k toroidal ETG modes. However, there is a limit on how small the θ can be, since modes can only be driven unstable in the bad curvature region in θ where as we have discussed above, the corresponding $\omega_{*e}\eta_e/\vec{V}_{Me} \cdot \vec{k}_\perp$ in the region cannot be too large. With $\theta_0 = 0$, $\omega_{*e}\eta_e/\omega_{Ke}$ is either too large or negative (good curvature region) with a range of θ around $\theta = 0$ (meaning that no unstable toroidal ETG mode in this θ range). On the other hand, a finite θ_0 can significantly change the θ location of potentially unstable regions, making bad curvature regions available at much smaller θ compared with the $\theta_0 = 0$ case, i.e., close to $\theta = 0$, where FLR damping is weaker for higher-k toroidal ETG mode. Thus, the appearance of bad curvature regions with small $\omega_{*e}\eta_e/\omega_{Ke}$ in small θ region with reduced FLR damping as a result of finite θ_0 makes it possible for the toroidal ETG mode to be the most unstable mode for a large $k_\theta \rho_s$ with a finite θ_0, which is not achievable with $\theta_0 = 0$, and this explains the existence of the toroidal ETG mode at $k_\theta \rho_i = 51.4$ seen in Fig. 51c. More details on finite θ_0 effects on the ETG mode structure can be found in Parisi (2020) (e.g., see discussions on Fig. 19 in the reference).

As we have mentioned, the usual $\eta_{e,\mathrm{crit}}$ for the ETG mode (Horton 1988; Jenko 2001) still applies in the H-mode pedestal region. However, it is only a necessary but not a sufficient condition for the off-mid-plane toroidal ETG mode to be unstable. An additional threshold in R_0/L_{T_e} is found to be in effect and is determined by the $\omega_{*e}\eta_e/\omega_{Ke}$ profile (Parisi 2020). It is shown that for unstable toroidal ETG modes, bad curvature regions in θ have to exist with $C < \omega_{*e}\eta_e/\omega_{Ke} < A$ with $C > 0$ [found using a local linear ETG model (Horton 1988; Jenko 2001)], and such bad curvature regions with $\theta_0 = 0$ have a minimum $|\theta|$ which is found to be only weakly dependent on R_0/L_{T_e}. Since $\omega_{*e}\eta_e/\omega_{Ke} \approx (R_0/L_{T_e})/(\hat{s}|\theta|)$ in bad curvature regions with $\theta_0 = 0$, with $\hat{s}$ fixed the minimum R_0/L_{T_e} to satisfy $\omega_{*e}\eta_e/\omega_{Ke} > c$ in bad curvature region has to be large enough, so that $(R_0/L_{T_e})_{\mathrm{min}}/(\hat{s}\theta_{\mathrm{min}}) = C$, and thus the critical (R_0/L_{T_e}), $(R_0/L_{T_e})_{\mathrm{crit}} = C\hat{s}\theta_{\mathrm{min}}$. Applying similar logic to finite θ_0 case and noting that new bad curvature region appears close to $\theta = 0$ with an opposite sign against θ_0, $(R_0/L_{T_e})_{\mathrm{crit}} = C\hat{s}(|\theta_{\mathrm{min}}| + |\theta_0|)$. Thus, it is found that both θ_{min} and θ_0 have the effect of increasing $(R_0/L_{T_e})_{\mathrm{crit}}$.

The usual mixing length approximation $\gamma/k_\perp^2$ is used by Parisi (2020) to provide a rough estimate of the transport diffusion coefficient due to the toroidal and slab ETG modes. Figure 52a plots the normalized $\gamma/k_\perp^2$ versus $k_y\rho_i$ and θ_0, where large values of $\gamma/k_\perp^2$ can be seen across a wide range of $k_y\rho_i$ and θ_0, i.e., $5 \lesssim k_y\rho_i \lesssim 100$ and $|\theta_0| \lesssim 1.5$. While the slab ETG mode remains most unstable for $\theta_0 = 0$ and $k_y\rho_i \gtrsim 5$, the large values of $\gamma/k_\perp^2$ with $\theta_0 \neq 0$ are due to the toroidal ETG mode. The maximum of normalized $\gamma/k_\perp^2$ over θ_0 for each $k_y\rho_i$ is shown in Fig. 52b, where it can be clearly seen that the fastest growing modes in $1 \lesssim k_y \lesssim 100$ show comparable estimated mixing-length diffusion coefficient, indicating that a wide range of $k_y\rho_i$ modes may be important for driving transport. Since the mixing-length estimate can only provide a rough assessment of the transport level driven by a particular mode, nonlinear simulations are required to determine the most responsible modes for transport, which we will address next.

4.2 ETG turbulence in the H-mode pedestal region

Having presented linear characteristics of the ETG mode in the H-mode pedestal region, we would like to review the role of ETG turbulence in driving plasma transport at the plasma edge studied through nonlinear gyrokinetic simulations and experimental measurements. Nonlinear gyrokinetic simulations have already demonstrated that ETG turbulence can play an important role in driving experimentally relevant electron thermal transport in the H-mode pedestal region (Jenko 2009; Told 2012; Hatch 2015, 2016, 2017; Kotschenreuther 2017, 2019; Guttenfelder 2021), where nonlinear characteristics of the ETG mode in the H-mode pedestal region are found to be significantly different from its counterpart in the plasma core. Here, we will first review nonlinear characteristics of ETG turbulence found with nonlinear gyrokinetic simulations in the H-mode pedestal region and then will move on to the role of ETG turbulence in driving plasma transport in the pedestal region, followed by relevant experimental evidence of ETG turbulence in the tokamak plasma edge (Canik 2011; Hillesheim 2016; Ren 2019a).

The hallmark of ETG turbulence in the H-mode edge is having isotropic eddies in the plane perpendicular to the magnetic field (Told 2012; Hatch 2015; Guttenfelder 2021), which is in contrast to the typical core ETG turbulence featured by radially elongated eddies (streamers) (Dorland 2000; Jenko 2000). This feature of the edge ETG turbulence can be clearly seen in Fig. 53 from Told (2012), where Fig. 53a shows that ETG turbulence eddies (in the quantity of electrostatic potential fluctuations) from a local gyrokinetic tokamak edge simulation are isotropic in the perpendicular plane to the magnetic field at the outer mid-plane as plotted in contours with physical spatial coordinates. Figure 53b shows similar radial profiles of turbulence radial and binormal correlation lengths ($\sim$ 4–6 ρ_e), demonstrating the isotropic feature of ETG turbulence in the H-mode pedestal

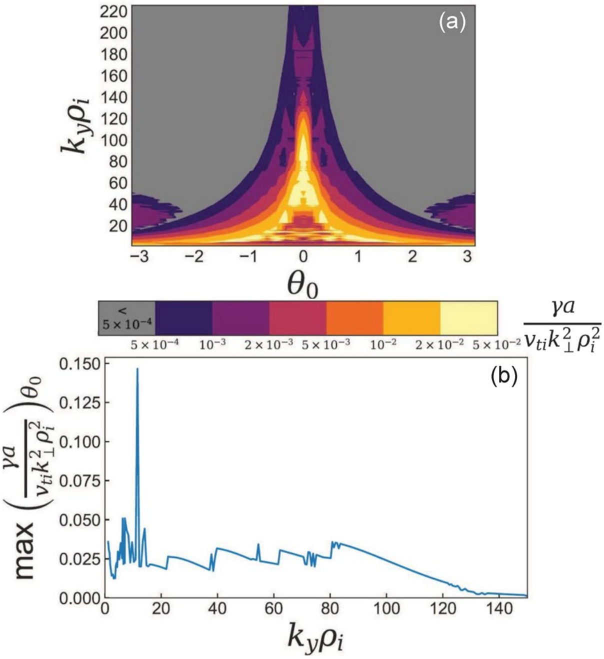

Fig. 52 **a** Normalized $\gamma/k_\perp^2$ (normalized to$\rho_i^2 v_{ti}/(a)$) as a function of $k_y\rho_i$ and θ_0 in contour plot; **b** the maximum value of normalized $\gamma/k_\perp^2$ over θ_0 for each $k_y\rho_i$. Panel a is adapted from Fig. 20b and panel b is adapted from Fig. 20d in Ref. (Parisi 2020), with the permission of International Atomic Energy Agency

region. Recall that the appearance of streamers is controlled by parameters of α and $\hat{s}$ (see Fig. 6) (Jenko 2000), where cases with high transport level have ETG streamers and are associated with large $\hat{s}$ and small α, while there are no streamers in cases with low-transport level and are characterized by small (and negative) $\hat{s}$ and large values of α. In the H-mode pedestal region, α is large due to large density and temperature gradients, and the $\hat{s}$ is usually large, as well. However, as pointed out in Told (2012), given that the typically large global $\hat{s}$ in the pedestal region is dominated by the large local magnetic shear near the X-point, the local magnetic shear around the outer mid-plane is actually small and even negative (see Fig. 54). As a result of large α and small (or negative) $\hat{s}$, ETG turbulence in the H-mode pedestal region likely falls in the low transport level regime shown in Fig. 6 and should not have ETG streamers. Usually, the regime of reversed/negative/weak magnetic shear is associated with large zonal flows that regulate ETG turbulence and, thus, break up streamers (Li 2005; Idomura 2005) (also see discussions in Sect. 2.2.3), which seems to be in agreement with pedestal ETG simulations (Told 2012; Hatch 2015; Guttenfelder 2021). However, zonal flows in these pedestal simulations are relatively weak and are not playing an important role in regulating the ETG turbulence. Thus, other saturation mechanisms are needed for ETG turbulence in the pedestal region, which remains an open question.

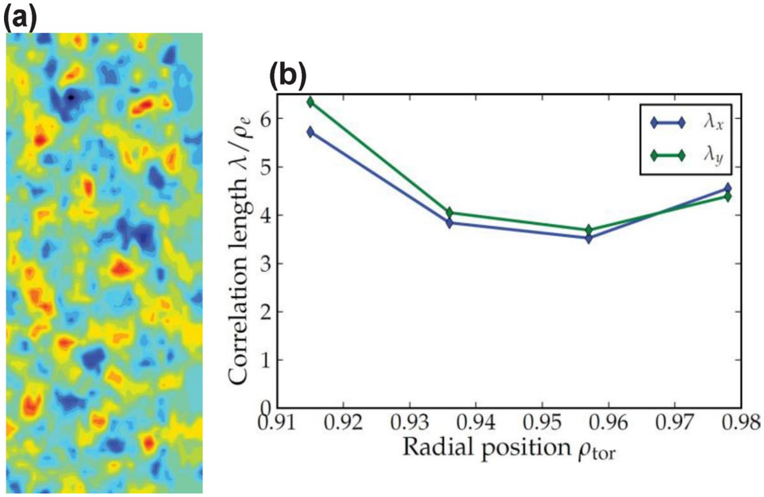

Fig. 53 **a** A contour plot of electrostatic potential fluctuations in the perpendicular plane to the magnetic field at the outer mid-plane from a local nonlinear gyrokinetic simulation of ETG turbulence at $\rho = 0.957$ of an ASDEX-U Type-I ELMy H-mode plasma (shot 20431) using the GENE gyrokinetic code (Jenko 2000). The axes are in physical scale, and the radial size of the box is 1.1 ρ_s (~1.8 mm); **b** radial profiles of the radial and binormal turbulence correlation lengths in ρ_e unit, demonstrating the statistical isotropy in the perpendicular plane. Note that the radial coordinate, ρ_{tor}, is the same as ρ, the square root of normalized toroidal flux. Panel a is adapted from Fig. 70 and panel b is adapted from Fig. 71 in Ref. (Told 2012), with permission of the author

Although it is common that the fastest growing mode in the H-mode pedestal region has a finite radial wavenumber (i.e., k_x or θ_0) (and peaks off outer mid-plane) as reviewed in the last section (Told 2008, 2012; Parisi 2020), nonlinear gyrokinetic simulations show that the generated electron heat flux is surprisingly localized around the outer mid-plane (Jenko 2009; Told 2012) (e.g., see Fig. 55). Examining the 2D wavenumber spectrum of electron heat flux driven by ETG turbulence, Jenko et al. (Jenko 2009) found that the spectrum peaks at $k_x = 0$ and $k_y\rho_s \sim 50$ (see Fig. 56) despite the fact that linear growth rate spectrum has peaks at finite k_x locations.

Having reviewed some characteristics of ETG turbulence in the H-mode pedestal region, the next question is whether ETG turbulence is able to generate experimentally relevant electron thermal transport. Given the small gyroradius of electrons compared with equilibrium scale lengths in almost all scenarios, ETG turbulence well satisfies the gyrokinetic ordering, and the thermal transport driven by ETG turbulence should obey the gyro-Bohm scaling with small ρ_e^*, i.e., $\chi_e = \alpha\chi_{e,gB}$ where the electron gyro-Bohm unit can be written as $\chi_{e,gB} = (\rho_e/a)\rho_e v_{the}$ or $\chi_{e,gB} = (\rho_e/L_T)\rho_e v_{the}$ (L_T is the temperature gradient). Note that since α is a function of local dimensionless equilibrium quantities, the system size dependence of χ_e, in this expression, only comes from ρ_e/L_T or ρ_e/a (we will use ρ_e/L_T for the $\chi_{e,gB}$ definition for the rest discussions). Thus, the electron thermal flux $Q_e = n_e\chi_e\nabla T_e \approx \alpha\chi_{e,gB}T_e/L_T$. Since $\chi_{e,gB} \sim T_e^{3/2}$, $Q_e \sim T_e^{5/2}$, assuming constant α and L_T. Due to this strong T_e dependence of Q_e, ETG turbulence was not considered to be important in driving experimentally relevant thermal transport in the pedestal region since T_e becomes quite small there (Callen 2010). However, this argument depends on the assumption of α and L_T being constant, which is not necessarily true

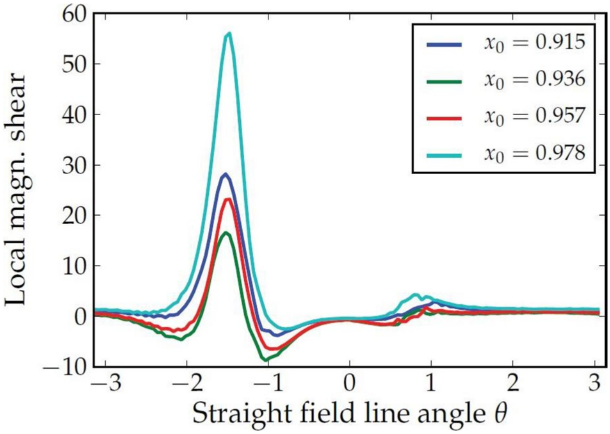

Fig. 54 Local magnetic shear along magnetic field lines (as a function of the straight field line angle θ) at four radial locations near the separatrix. Local magnetic shear is seen at the bottom of the plasma ($\theta \sim -\pi/2$) around the X-point, while small and negative magnetic shear is seen around the outer mid-plane ($\theta \sim 0$). The figure is reprinted from Fig. 72 in Ref. (Told 2012), with permission of the author

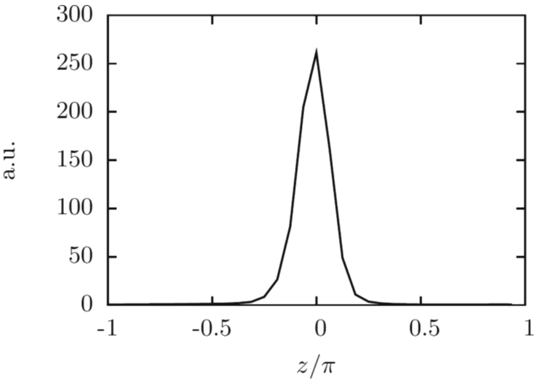

Fig. 55 Parallel profile of the electrostatic ETG-driven electron heat flux. z is the parallel coordinate with zero being at the outer mid-plane. The result is from a local nonlinear simulation at $\rho_{\mathrm{pol}} = 0.98$ and t=1.82 s of an ASDEX-U Type-I ELMy H-mode plasma (shot 20431) using the GENE code. The figure is from Fig. 5 in Ref. (Jenko 2009). Reprinted from Ref. (Jenko 2009), with the permission of AIP Publishing

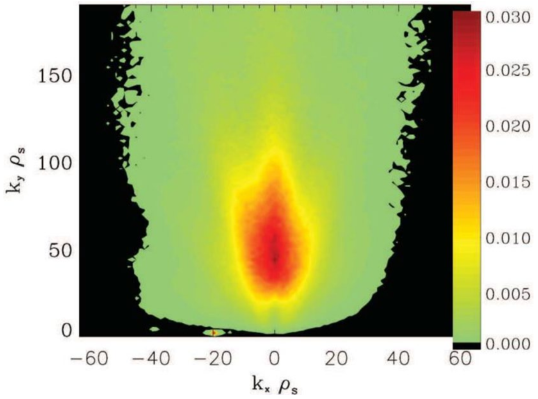

Fig. 56 2D wavenumber spectrum of electrostatic electron heat flux driven by the ETG turbulence. The result is from a local nonlinear simulation at $\rho_{\mathrm{pol}} = 0.98$ and t=1.82 s of an ASDEX-U Type-I ELMy H-mode plasma (shot 20431) using the GENE code. The figure is from Fig. 6 in Ref. (Jenko 2009). Reprinted from Ref. (Jenko 2009), with the permission of AIP Publishing

in the plasma edge as T_e gradient could vary significantly in the pedestal region. Indeed, L_T can become quite small (see examples in the last section), while α can also vary [e.g., α depends sensitively on η_e, see Ref. (Told 2012)]. As a result, $Q_e \sim \alpha T_e^{5/2}/L_T$ is not necessarily small in the pedestal region as having been demonstrated by nonlinear gyrokinetic simulations (Jenko 2009; Told 2012; Hatch 2015, 2016, 2017; Kotschenreuther 2017, 2019; Guttenfelder 2021). By carrying out local nonlinear ETG gyrokinetic simulation at a flux surface location of $\rho_{pol} = 0.98$ for ASDEX-U shot 20431, Jenko (2009) showed an electron heat diffusivity of 0.83 m^2/s from ETG turbulence, which is in good agreement with the experimental value of $\chi_e \sim 0.4$ m^2/s from an ASDEX-U shot close to the L–H transition (Coster et al. 2008) and a nonlinear critical threshold coincides with the linear one, $\eta_{e,crit} \approx 2$ from a T_e gradient scan, showing that ETG turbulence could be a main contributor to the electron thermal transport in the H-mode pedestal region. More recent numerical studies have confirmed the important role of ETG turbulence in driving electron thermal transport in the present-day tokamaks (Hatch 2015, 2016, 2017; Kotschenreuther 2017; Guttenfelder 2021). In particular, it was found that ETG is usually dominant in the region with large η_e (as having been shown η_e is the control parameter when density gradient is large as it is usually the case in the pedestal) and is usually close to a nonlinear critical gradient for the ETG turbulence. For example, as demonstrated in Hatch (2015), a modest change in gradients (a 20% increase in a/L_{T_e} and a 20% in a/L_{n_e}) can lead to an order of magnitude increase in electron thermal transport (see Fig. 57), showing that it is η_e that determines the nonlinear threshold for ETG turbulence rather than a/L_{T_e} alone. This is not surprising as we have mentioned in the last section that the linear stability boundary is determined by η_e when a/L_{n_e} becomes large enough. As a result of $\eta_{e,crit}$, a large T_e gradient would require a large n_e gradient in the H-mode pedestal, and thus, both thermal and particle transport barriers would be formed. The contribution of ETG turbulence in the pedestal region is not uniform and at locations where η_e is smaller but a/L_{T_e} remains large, MTM could become dominate (Hatch 2016), although the contribution from ETG turbulence remains substantial (see Fig. 58). On the other hand, nonlinear

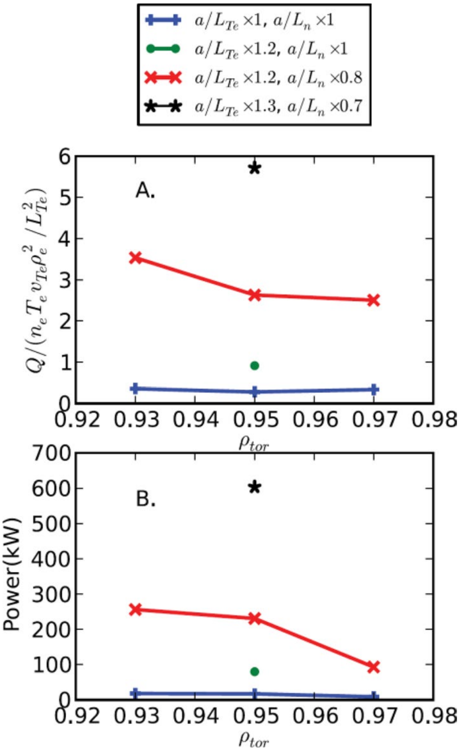

Fig. 57 Radial electron heat flux profiles from nonlinear local ETG gyrokinetic simulations with adiabatic ions using the GENE code for an ASDEX-U H-mode plasma during an inter-ELM phase featured by steep temperature gradients but comparable density gradients in much the pedestal region: **A** heat flux normalized to the electron gyro-Bohm unit; **B** heat flux in kW. Results from nominal a/L_{T_e} and a/L_{n_e} are shown as blue plus signs and other scans in gradients are self-explanatory in the legend. It is clearly seen that with a 30% change in gradients, Q_e reaches 600 kW. Given that the 1–3 MW power can be attributed to all transport processes and all uncertainties with the electron power flow, 600 kW of electron heat flux by ETG turbulence could account for a significant fraction of the electron heat flux in the pedestal region. The figure is reprinted from Fig. 9 in Ref. (Hatch 2015), with the permission of International Atomic Energy Agency

simulations considering ρ^* dependence (Hatch 2017; Kotschenreuther 2017) show that the contribution from ETG turbulence obeying the gyro-Bohm scaling would become less important in future devices (with smaller ρ^*) due to an unfavorable ρ^* scaling of ITG turbulence as it becomes less E×B -shear-suppressed with smaller ρ^*.

Electron-scale turbulence in the H-mode pedestal region has also been studied experimentally (Canik 2011; Hillesheim 2016; Ren 2019a) using diagnostic techniques that have been discussed in Sect. 3.2.1, providing experimental evidence of the existence of ETG turbulence and its role in driving electron thermal transport in the pedestal region. With the high-k scattering system on NSTX (Smith 2008) to measure electron-scale density fluctuations around the pedestal top, Canik (2011) showed that electron-scale turbulence exists in NSTX shots with and without lithium and lithium deposition tends to reduce electron-scale turbulence at least in some portion of the wavenumber spectrum. As seen in Fig. 59a and b, compared with the shots without lithium, lithium deposition leads to increased $a/_{T_e}$ and a/L_{n_e} around the pedestal top, while in the pedestal, the T_e profiles are similar with the density gradient significantly reduced close the separatrix (T_e and n_e profiles in Fig. 59a and b were generated by combining several time slices of these shots). A reduction in spectral power at $k_\perp \rho_s < 10$ with lithium is seen at the pedestal top (see Fig. 59c), while a reduction in spectral power at higher wavenumbers with lithium is seen in the pedestal (see Fig. 59d). Since the shots without lithium have a heating power of 5 MW and the shots with lithium have lower heating powers (3 MW for shot 141325 and 2 MW for shot 141328), the measured lower spectral power of the measured electron-scale turbulence in the shots with lithium indicates that the electron-scale

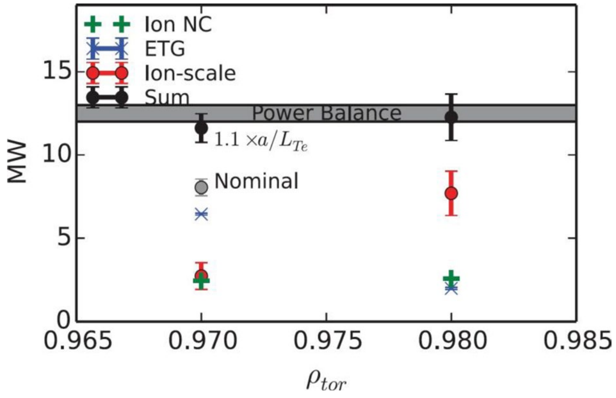

Fig. 58 Comparison of calculated heat flux contributions [ion neoclassical (green plus signs), ETG (blue asterisks), and MTM (red filled circles)] with experimental power balance at two radial locations in the pedestal of a JET ITER-like wall H-mode plasma. The GENE code was used to carry out single-scale nonlinear gyrokinetic simulations for the ion scale (MTM) and the electron scale (ETG). Adiabatic ions were used in the ETG simulations. A good agreement between the calculated total heat flux (black filled circles) with the experimental power loss through transport (~ 12 MW, denoted by the gray band) is seen at $\rho_{\mathrm{tor}} = 0.98$ with nominal equilibrium values, while a good agreement is also reached at $\rho_{\mathrm{tor}} = 0.97$ with a very modest 10% increase in $a/_{T_e}$. Note that ETG has the dominant contribution at $\rho_{\mathrm{tor}} = 0.97$ due to larger η_e, while MTM dominates at $\rho_{\mathrm{tor}} = 0.98$ in the steep-gradient region. The figure is reprinted from Fig. 5 in Ref. (Hatch 2016), with the permission of International Atomic Energy Agency

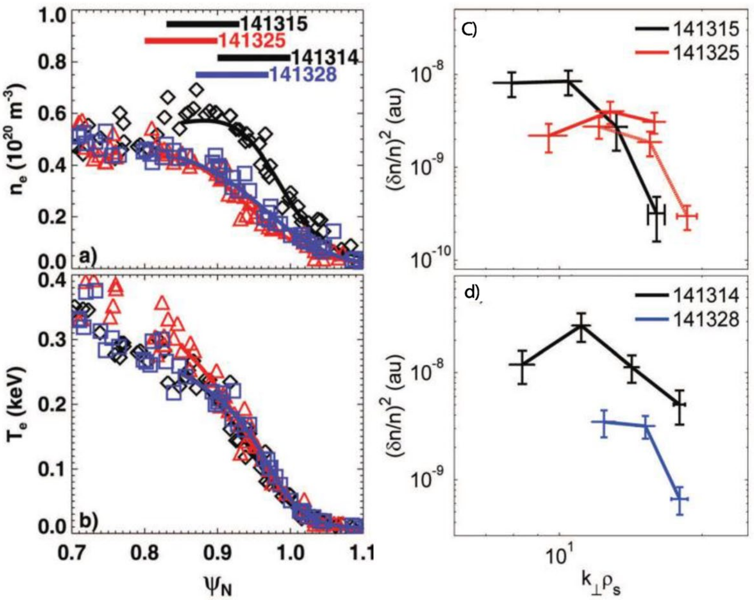

Fig. 59 **a** Electron density profiles for NSTX shots with lithium (blues squares and red triangles) and shots without lithium (black diamonds); **b** the same as in (**a**) but for electron temperature; **c** wavenumber spectra measured at similar radial locations for shot 141325 with lithium (red solid line) and shot 141315 without lithium (black solid line) together with the wavenumber spectrum measured at a larger radial location for shot 141328 with lithium (red dashed line) shown for comparison; **d** wavenumber spectra measured at similar radial locations for shot 141328 with lithium (blue solid line) and shot 141314 without lithium (black solid line). The shots without lithium are ELmy H-mode with 5 MW of heating power, while heating powers are lower for the shots with lithium, i.e., 3 MW for shot 141325 in (**c**) and 2 MW for shot 141328 in (**d**). Note that the radial range for the electron-scale turbulence measurement for each shot is shown as horizontal thick lines in (**a**) denoted with the corresponding shot number. Two radial ranges were configured for the turbulence measurement for shots with lithium and without lithium: one covers the pedestal top at a smaller radius and the other extends further into the pedestal region with steep gradients [the two ranges have some overlap as seen in (**a**)]. Panels a and b are adapted from Fig. 10 and panels c and d are adapted from Fig. 11 in Ref. (Canik 2011). Reprinted from Ref. (Canik 2011), with the permission of AIP Publishing

turbulence could contribute to thermal transport. Linear stability analysis of these plasmas shows that the ETG linear growth rate in the pedestal region of the shots with lithium is significantly higher than that for the shots without lithium (Canik 2013), which indicates that ETG modes may be much more important in plasmas with lithium than in plasmas without lithium. This hypothesis is supported by the observation of a significant reduction in the ion-scale turbulence in the pedestal with lithium measured by edge reflectometers (Canik 2011).

Another pedestal top measurement of electron-scale turbulence at the pedestal top in the H-mode phase was made around the L–H transition in NSTX plasmas (Ren 2019a) with the high-k scattering system (Smith 2008). The evolution of electron-scale turbulence (for $3 \lesssim k_\perp \rho_s \lesssim 12$) was measured across the L–H transition. It is observed that before the high-k turbulence is suppressed to its minimum at about t=365 ms with the L–H transition occurring at about t=350 ms, it gradually decreases from about t=350 to 365 ms, during which time there are intermittent periods of about 0.5–1 ms having close to minimum high-k turbulence (see Fig. 60a and c). This "dithering" phase (from about t=350 to 365 ms) of high-k turbulence coincides with similar "dithering" behavior seen in the D_α signal for the same time period, although no phase correlation between the two is identified (low-f MHD activities are relatively benign after the L–H transition). The measured wavenumber spectra show that the suppression of the high-k turbulence occurs only at lower wavenumbers, namely $k_\perp \rho_s \lesssim 9$. It is after this "dithering" phase that the ETB at $r/a > 0.9$, typical of the H-mode, is fully established. The suppression of high-k turbulence is found to be consistent with a decrease in the maximum ETG linear growth rate from gyrokinetic stability analysis using measured equilibrium profiles. However, such consistency cannot explain the observed intermittency in the high-k turbulence, since equilibrium profiles are not expected to change much on the 0.5–1 ms time scale of the high-k quiescent periods and nonlinear effects must play an important role. In addition, low-k turbulence measurements from Beam Emission Spectroscopy (BES) diagnostic (Smith 2012) at the same location exhibited similar temporal intermittency as the high-k turbulence (see Fig. 60b and c). None of the measured electron-scale turbulence and ion-scale turbulence from the edge into the core is found to be obviously leading in the response to the L–H transition and the overall turbulence suppression after the start of the L–H transition at different radii seems to start at the same time and is a gradual process happening on a tens-of-ms time scale. This observed suppression of electron-scale turbulence indicates the importance of ETG turbulence in the formation of the edge transport barrier in H-mode plasmas.

Evidence of ETG turbulence in the H-mode pedestal region was also provided in the intermediate wavenumber range ($k_\perp \rho_s \approx 3$ to 4), i.e., between ρ_e and ρ_i scales, in the pedestal of MAST ELMy H-mode plasmas by Hillesheim (2016) by combining DBS and cross-polarization scattering (CP-DBS) diagnostic techniques. The measurement locations shown in Fig. 61a are obtained from ray tracing at three different ELM phases each representing one-third of the ELM cycle. There are fewer DBS/CP-DBS channels in the pedestal region early in the ELM cycle, and the measurement locations systematically move outward in the region of $\psi \approx 0.97 - 0.99$ as the density profile evolves in the ELM cycle. In particular, only the 55 GHz channel of the CP-DBS is pedestal localized for the first one-third of the ELM cycle, while there are two and three channels pedestal localized in the later two one-third of the ELM cycle. Compared with measurements in Canik (2011) and Ren (2019a), the measurement locations in these MAST H-mode plasmas are at somewhat larger radii than that in Ren (2019a) and are more comparable to those in Canik (2011). The temporal evolutions of the scattered power from both DBS and CP-DBS in the ELM cycle are shown in Fig. 61b, where, for density fluctuation power, the decrease after the ELM (0.5–1 ms), the small variation in the scattered power between 1 add 2 ms, the sharp rise in the scattered power between 2 and 3 ms, and the saturation afterward can be easily seen. Although the magnetic fluctuation power from the CP-DBS data has a similar behavior as density fluctuations in the first 0.5–1

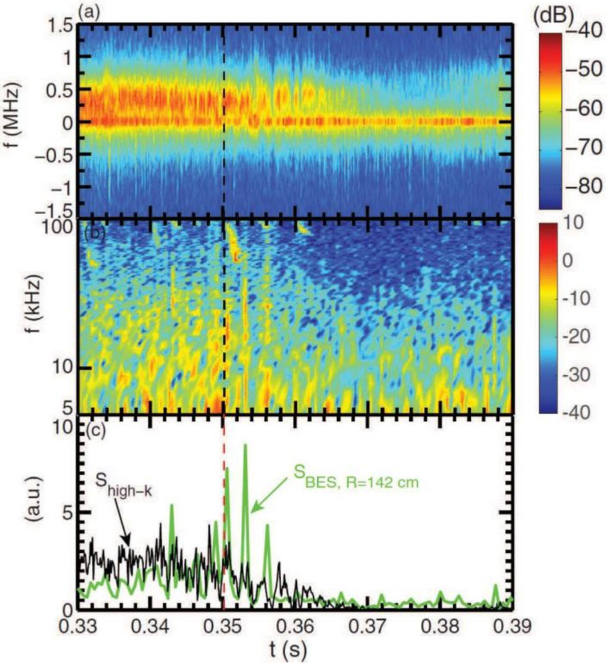

Fig. 60 **a** Spectrogram of scattering channel 3 of the high-k scattering system; **b** spectrogram of a BES channel at R=142 cm; **c** the total scattering power (S_{high-k}) together with the ion-scale density fluctuation power measured by a BES channel at R=142 cm, $S_{\mathrm{BES},R=142\ \mathrm{cm}}$. Measurements were made during the L–H transition induced by NBI power step-up in an NSTX plasma with $B_T = 5.5$ kG and $I_p = 1.1$ MA (shot 139442). The figure is reprinted from Fig. 7 in Ref. (Ren 2019a), with the permission of International Atomic Energy Agency

ms, it rises secularly for the rest of the ELM cycle except for perhaps the last 2–3 ms. The fast rise in the density fluctuation power happening between 2 and 3 ms is found to be correlated with a fast recovery of the density profile at about 2 ms after the ELM. On the other hand, the secular rise in the magnetic fluctuation power is found to follow a similar secular rise of the temperature pedestal. The measured $(\delta B/B)/(\delta n_e/n_e) \approx 1/20$ (taken into account the hardware difference between the DBS and CP-DBS) is comparable to that of ETG modes (≈ 0.02) obtained with GS2 linear stability analysis with experimental profiles, supporting the existence of ETG turbulence in the pedestal region in MAST H-mode plasmas.

5 Discussion

Having presented plenty of theoretical, numerical, and experimental evidence of the importance of the ETG mode in driving electron thermal transport in tokamaks in sections above, here we would like to discuss the potential role of the ETG mode in STs. We emphasize that the ETG mode could be particularly important to STs, since fusion-relevant high-power STs are characterized by large E×B

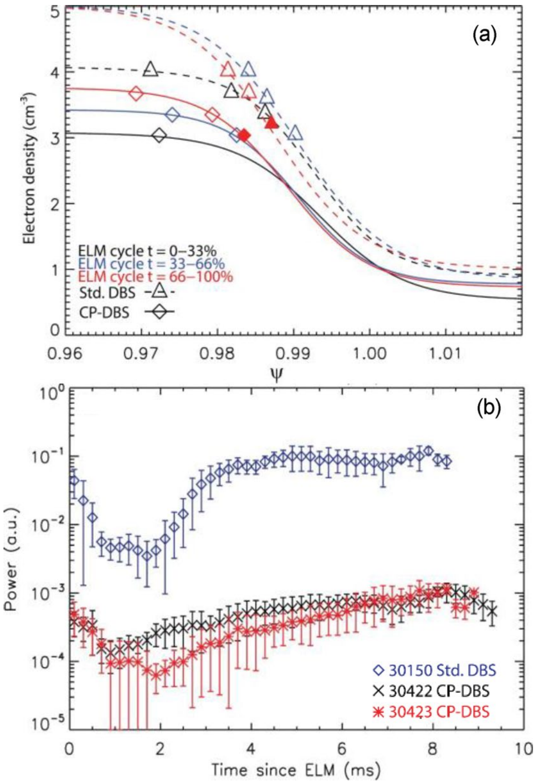

Fig. 61 **a** Conditionally averaged density profiles [solid (dashed) lines for MAST ELMy H-mode shots 30422/30423 (30150)] and turbulence measurement locations (colored symbols) during the ELM cycle with diamonds denoting measurement locations for CP-DBS and the triangles denoting measurement locations for standard DBS measurements. Filled symbols denote the 55 GHz channel location for the last third of the ELM cycle. **b** The average and standard deviation of DBS and CP-DBS data every 200 μs plotted against time since the previous ELM. All data are from the 55.0 GHz channel only. Panel a is adapted from Fig. 6 and panel b is adapted from Fig. 10 in Ref. (Hillesheim 2016). © IOP Publishing. Reproduced with permission. All rights reserved

shear and strong plasma shaping (due to small aspect ratio) which tend to almost completely suppress low-k turbulence and make ion thermal transport neoclassical, e.g., in NSTX H-mode plasmas (Ren 2017) (note that this is not the case in NSTX L-mode plasmas, i.e., see Ren (2013)). The large linear growth rates of the ETG mode render the E×B shear less effective for ETG turbulence [except for the case where the ETG mode is very close to marginal stability (Smith 2009)], and thus, the ETG mode is a natural candidate for driving electron thermal transport in high-power STs, e.g., NSTX, NSTX-U, and MAST. Indeed, experimental measurements and nonlinear gyrokinetic simulations based on measured profiles have shown that ETG-turbulence-driven electron thermal transport (with T_e gradient varied within experimental uncertainties) could match the experimentally inferred transport within its experimental uncertainty at some radial locations in an MAST ELMy H-mode plasma (Joiner 2006), NSTX H-mode plasmas (Guttenfelder 2013; Ren 2012; Ruiz 2019), and NSTX RF-heated L-mode plasmas (Wang 2015; Peterson 2012, 2011). It is also clear that the simulated ETG turbulence could not account for the observed electron thermal transport across the radius in NSTX H-mode plasmas (Ren 2012; Stutman et al. 2007). We note that the present validation efforts of ETG turbulence are still far from covering a wide parametric regime, and thus, a mapping of the operational regime of ETG turbulence has not been achieved. There is also evidence that the residual ion-scale turbulence in NSTX H-mode plasma could contribute to driving electron thermal transport (Ren 2012, 2019b). This leads one to ask whether the residual ion-scale turbulence in ST H-mode plasmas still plays a role in driving electron thermal transport or whether the present gyrokinetic codes are able to adequately simulate ETG turbulence in STs. Furthermore, multi-scale interaction between ion-scale turbulence and ETG turbulence could also play a role in ST plasmas. The principal reason why there lacks a much larger scale validation study of the role of ETG turbulence in driving electron thermal transport in STs is the computational cost of first-principle gyrokinetic simulations, and thus, reduced models of ETG turbulence are required for a larger scale validation study covering much wider parametric space. There has been quite a bit of development of reduced models of ETG turbulence based on the conventional tokamak parameters (Staebler 2005; Kinsey 2008; Rafiq 2013; Casati 2009); however, its usefulness to STs seems to be limited, and further development of reduced ETG models for the ST regime is needed (see more discussion on the reduced model further below). Another important question that we have discussed is the ρ_e^* scaling of ETG turbulence which determines how we can scale the contribution of ETG turbulence to future STs with smaller ρ_e^*. Similar to ITG turbulence (Lin 2002; Candy 2004), the gyro-Bohm scaling for ETG turbulence is expected in the $\rho_e^* \to 0$ limit. Particularly, the ETG-turbulence-driven electron thermal transport is shown to satisfy the gyro-Bohm scaling when ρ_e^* is sufficiently small as seen in Lin (2005), Hatch (2017) and Kotschenreuther (2017), while with larger ρ_e^*, the ETG-turbulence-driven electron thermal transport scaling is found to be not gyro-Bohm (Bottino 2007) (although we note that these studies are based on the conventional tokamak parameters). To approach the gyro-Bohm scaling with small-enough ρ_e^* is certainly good news for future STs featured by smaller ρ_e^*. On the other hand, it is found that the deviation from the gyro-Bohm scaling is better expressed in terms of $\rho_{\text{eff}}^* = \rho_i/\omega$ (McMillan 2010; Villard 2010), where ω is the width of the T_i temperature gradient profile. In other words, if ρ^* is varied with fixed ρ_{eff}^*, ρ^* variations alone do not significantly change the transport level according to McMillan (2010). Thus, if we apply this conclusion to ETG turbulence, in the case that the T_e gradient profile scales with a (i.e., $\omega/a \sim$ constant) when scaled to future STs, the use of local flux-tube predictions of electron thermal transport by ETG turbulence (i.e., using the gyro-Bohm scaling) would be sufficient. We note that the existence of transport barriers may break the $\omega/a \sim$ constant scaling. In this context, the global-effects-induced transport deviation from the gyro-Bohm limit would persist with smaller ρ_e^*, and as a result, global simulations for predicting the ETG-turbulence-driven electron thermal transport would be needed. Furthermore, global simulations may also be needed if one wants to self-consistently simulate the generation of transport barriers (and how their width scales with system size). As for the ETG turbulence in the ST H-mode pedestals, although the edge nonlinear ETG gyrokinetic simulations based on edge parameters of conventional tokamaks have demonstrated the importance of the edge ETG turbulence can generate experimentally relevant electron thermal transport (Jenko 2009;

Told 2012; Hatch 2015, 2016, 2017; Kotschenreuther 2017, 2019; Guttenfelder 2021), the role of ETG turbulence in the ST H-mode pedestals is still an open question, and targeted nonlinear gyrokinetic simulations are needed to address this issue.

We note that given the importance of ETG turbulence in driving experimentally relevant electron thermal transport in fusion plasmas, development and validation of high-fidelity reduced models including electron-scale modes (particularly the ETG mode) (Staebler 2005; Kinsey 2008; Rafiq 2013; Casati 2009) becomes increasingly important for optimizing the performance of future fusion devices due to the high computational cost of first-principle gyrokinetic simulations. The importance of reduced models becomes even more evident in light of the recent discovery of the importance of multi-scale interactions between ion-scale and electron-scale turbulence through the first-principle multi-scale simulations (e.g., (Görler and Jenko 2008; Howard 2016; Maeyama 2015)), the computation cost of which is even more prohibitive for the utilization of these first-principle models for predictive simulations of future devices. We note some success has been made in predicting T_e profiles in DIII-D L and H-mode plasmas, an EAST H-mode plasma, and an NSTX L-mode plasma (Petty 2015; Staebler 2017; Jian 2017; Kaye 2019) with the TGLF reduced model (Staebler 2005), showing the importance of the ETG mode. Particularly, saturation models taken into account of multi-scale interactions between ion-scale and electron-scale turbulence are proven essential for predicting experimental profiles (Staebler 2017; Jian 2017). However, discrepancies found in NSTX H-mode plasmas and C-MOD I-mode plasmas with TGLF (Kaye 2019; Creely 2017) show the need for further development of reduced models. Clearly, the success of present reduced models is still only in a limited parametric regime. Further understanding of how different ETG saturation mechanisms dominate in different parametric regimes would help the development of high-fidelity reduced models. Furthermore, it is well known that there is a great need for reduced ETG models for the H-mode pedestal region given the importance of ETB contribution to the overall energy confinement of fusion devices and the importance of ETG turbulence in driving electron thermal transport as discussed in Sect. 4.2. However, the present reduced models are only validated with core parameters and their validation in the H-mode pedestal region is questionable due to the difference in the ETG mode linear and nonlinear characteristics discussed in Sect. 4, and more research efforts are certainly needed in this area of research.

The studies of ETG turbulence reviewed here would ultimately benefit the prediction and optimization of the confinement performance of future electricity-generating burning plasmas, since burning plasmas feature dominant electron heating due to fusion-generated α particles and higher β which tends to stabilize the ITG mode (Kim 1993; Hirose 2000; Gao 2001; Zocco 2015). We need to emphasize that this finite β stabilization of the ITG mode by no means makes the ITG mode irrelevant in burning plasmas. In fact, more recent nonlinear gyrokinetic simulations have demonstrated the potential importance of the ITG mode (Howard 2021; Nakata and Honda 2022), which is not surprising, since even in burning plasmas, β varies significantly from the plasma core to the edge. Furthermore, a large enough β would destabilize KBM (Aleynikova 2018; Kumar 2021; Mishchenko 2022). We would also like to point out that in addition to the demonstration of the potential importance of ETG turbulence in driving electron thermal transport, potential ways of controlling ETG turbulence have also emerged in the past studies, including density gradient stabilization (Ren 2011; Ruiz 2015), E×B shear stabilization(Smith 2009), negative/reversed magnetic shear stabilization (Yuh 2009, 2011; Mazzucato 2009), and collisionality (Kim 2003; Wang 2015; Colyer 2017). In addition, as we have reviewed the past and ongoing development and validation effects of first-principle/reduced ETG turbulence models (and numerical codes) based on the existing magnetic confinement devices have provided us with some level of prediction capability of the performance of future fusion devices, although as we have pointed out further improvements are certainly needed (particularly for the ST regime).

Here, we would also like to say more about TEM (Kadomtsev and Pogutse 1967, 1969, 1971; Nordman 1990; Ernst et al. 2004; Dannert and Jenko 2005; Ernst et al. 2006; Ernst 2009) which has been shown to be an important mechanism behind particle transport and ion and electron thermal transports and, in certain parameter regimes, is closely related to the shorter wavelength ETG mode (note that the ETG mode mainly drives electron thermal transport, and the particle transport from it is expected to be small due to the adiabatic behavior of ions at the electron scale). As a well-studied mode, TEM is known to be driven unstable by electron density gradient or electron temperature gradient through resonant or non-resonant processes. On the other hand, the ETG mode is driven unstable by electron temperature gradient and stabilized by electron density gradient (Lee 1987; Horton 1988). Thus, the unstable region in terms of a/L_{n_e} and a/L_{T_e} is much larger for TEM than for the ETG mode as having been mapped in Ref. (Ernst 2009). In particular, with $\eta_e < 1$, pure resonant/non-resonant TEM was identified with the maximum linear growth rate in the ion scale, i.e., $k_y\rho_s < 1$, in Ref. (Ernst 2009) with a/L_{T_i} set to zero, while as η_e exceeds 1, the maximum linear growth rate location moves to the intermediate scale, $k_y\rho_s > 1$, which is likely due to the coupling with the ETG mode as both modes now belong to the same branch of solution of the dispersion relation. Nonlinearly, TEM in the $\eta_e < 1$ region drives particle transport and electron and ion thermal transports which do not strongly depend on η_e, while in the $\eta_e > 1$ region, particle transport and ion thermal transport strongly decrease with increasing η_e, and, on the other hand, electron thermal transport driven by TEM is much less affected by η_e than particle transport and ion thermal transport. The decrease in particle transport and ion thermal transport with large η_e is a result of ions becoming more adiabatic as the fastest growing mode moves to higher wavenumber $k_y\rho_s > 1$. Similar to the ITG mode, the ion-scale TEM is susceptible to E×B shear and is likely suppressed in transport barriers where the E×B shearing rate is larger than the linear growth of TEM, while the higher-k ETG mode would likely survive to drive the residual electron thermal transport in transport barriers. Another important parameter related to TEM and the ETG mode is T_e/T_i which has a different effect on TEM and ETG, where a larger T_e/T_i tends to stabilize the ETG mode (see Eq. 12 where T_e/T_i increases the ETG mode linear threshold), while it tends to destabilize TEM, meaning that TEM should be more important in hot-electron plasmas, e.g., burning plasma heated by α particles. As we have discussed in Sect. 2.2.5, the cross-scale interaction between TEM and the ETG mode was investigated in Maeyama (2022), where a mutual suppression effect between TEM and ETG was found. In this case, in a range of T_e/T_i, the total electron heat flux from multi-scale simulations is less than the sum of electron heat fluxes from the ion-scale-only and electron-scale-only simulations.

One area we have not fully addressed in the paper is studies of electron-scale modes in addition to the standard ETG mode, some of which we have mentioned in Sect. 1. These modes have to do with the non-adiabatic response of ions at $b = (k_\perp \rho_i)^2 >> 1$ (Smolyakov 2002; Hirose and Elia 2002; Hirose 2002). The usual large b expansion of ion density response leads to $\tilde{n}_i = -(e\phi/T_i)n_0 + (\omega + \omega_{in}^*)/(\omega + \omega_{Di})(1/\sqrt{2\pi b})(e\phi/T_i)n_0$ (Hirose and Elia 2002), where ω_{in}^* is the ion diamagnetic frequency and ω_{Di} is the magnetic drift frequency. If $b >> 1$ and $\omega >> \omega_{\mathrm{in}}^*$ and ω_{Di}^*, the second term on the RHS becomes small and we obtain the usual ion adiabatic response. However, if $\omega_{Di}^* << \omega << \omega_{\mathrm{in}}^*$, the second term on the RHS becomes finite even with $b >> 1$, since $\omega_{\mathrm{in}}^* \propto \sqrt{b}$. Thus, there is a regime of mode frequency where the ion response remains non-adiabatic with $b >> 1$, and the conventional ITG mode can extend to short wavelength, the so-called SWITG mode (Hirose 2002; Smolyakov 2002; Gao 2005; Chowdhury 2009, 2012). It is found that the SWITG mode is essentially a slab ion mode [propagating in the ion diamagnetic drift with toroidicity being strongly stabilizing (Hirose 2002; Gao 2005)], being unstable even with adiabatic electrons and is driven by both T_i and T_e gradients through Landau damping/inverse Landau damping (Gao 2005). However, nonlinear gyrokinetic simulations (Chowdhury 2012) with adiabatic electrons show that SWITG does not provide significant additional ion thermal transport despite its comparable linear growth with the conventional ITG mode, although its effect on electron thermal transport has not been addressed. Another electron-scale mode is UM (Coppi and Rewoldt 1974; Coppi and Pegoraro 1977; Migliuolo 1995; Shen 2019) which is an extension of the conventional low-k collisionless TEM into $k_\theta \rho_i > 1$ region. In contrast to the low-k TEM, UM can be either purely growing or propagating in the ion diamagnetic drift direction. T_e, T_i, and density gradients all drive UM, and UM can stay unstable even with zero temperature gradients. A study of the parametric dependence of UM onset by Shen et al. Shen (2019) shows that the existence of UM is favored with a small $\hat{s}$, a large inverse aspect ratio, a small T_e gradient (note that a large T_e gradient can lead to a transition to the conventional TEM), a large T_i gradient and a large density gradient. This combination of parameters could more easily be found in lower-aspect-ratio spherical tokamaks. Indeed, UM is identified in hot-ion plasmas in the ST40 spherical tokamak (Ren 2023). We note that electron-scale fluctuations propagating in the ion diamagnetic drift direction were actually observed with a coherent microwave scattering system in TFTR plasmas with reversed magnetic shear (Wong 1997) and its correlation with electron thermal diffusivity was also demonstrated. As we have pointed out, studies on these electron-scale modes are still quite premature, lacking detailed studies on the nonlinear physics and their contributions to electron thermal transport, and thus, the roles of these electron-scale modes in driving electron thermal transport are still an open question.

6 Summary

In summary, the well-known electrostatic ETG mode (also known as η_e mode), despite its small characteristic spatial scale on the order of electron gyroradius, has been shown to be able to make significant contributions to the electron thermal transport and is the most extensively studied electron-scale mode with theoretical analyses, numerical simulations, and experimental measurements. The existence of the ETG mode has long been known by the plasma community (Kadomitsev and Pogutse 1970). However, its role in driving significant transport was initially dismissed due to its small spatial scale. The interest in the ETG mode has been renewed by theoretical analyses of the slab ETG mode with finite β effects (Rozhanskii 1981; Lee 1987) and experiment-relevant quasi-linear estimates of electron thermal transport based on magnetic flutter effects (Rozhanskii 1981) and larger radial extent due to a finite β (Lee 1987). The toroidal ETG mode was studied in subsequent theoretical works, and again, the ETG mode was found to be able to make a significant contribution to electron thermal transport (Horton 1988; Dong 2002, 2003). However, as we have discussed in Sect. 4.1, these linear theories assumed that the ETG mode structure peaks around the outer mid-plane which is applicable with typical core parameters, but may not be satisfied with typical H-mode pedestal parameters (particularly due to large normalized T_e gradient), and an analytical theory was developed to explain the off-mid-plane peaking and low-k_y features of a novel type of toroidal ETG mode in the pedestal region (Parisi 2020). Thanks to major advancements in gyrokinetic theory/numerical codes and computational capabilities, the pioneering work by Dorland (2000), Jenko (2000), and Jenko and Dorland (2002) demonstrated with local flux-tube gyrokinetic simulations that despite the apparent isomorphism between ETG and ITG modes, the ETG mode is able to generate larger normalized electron heat flux than the ITG mode by forming radially elongated E×B flow streamers due to its weaker zonal flow and secondary instability resulting from the difference in electron and ion adiabatic responses. However, later global gyrokinetic simulations seemed to contradict these findings by showing a different initial saturation mechanism (i.e., nonlinear nonlocal toroidal mode coupling) and a much lower normalized electron heat flux driven by ETG turbulence (Lin 2005). This difference was found to be due to the discrete particle noise of PIC codes, (e.g., too few marker particles in a simulation cell) leading to artificial damping of the ETG mode and low electron thermal transport, and the same level of electron thermal transport as continuum flux-tube codes can be recovered once the particle noise is controlled (Nevins 2005; Jenko 2009; Bottino 2007). A cross-codes benchmark by Nevins (2006), Nevins (2007) and Dimits (2007) demonstrated that continuum codes and PIC codes with the same equilibrium input could generate a statistically similar amount of electron thermal transport that is large enough to be experimentally relevant. Gyrofluid/gyrokinetic simulations also demonstrate other initial saturation mechanisms for the ETG mode (Idomura 2005; Li and Kishimoto 2008; Wang 2015), the understanding of which is important for the subsequent nonlinear evolution of ETG turbulence, and what determines the presence of a particular saturation mechanism is still an open question. Although zonal flows are found to be unimportant for the initial saturation of the ETG mode due to its weak amplitude, it is observed that zonal flows can play a role in the subsequent nonlinear evolution phase with magnetic shear likely being the control parameter. It is found that zonal flows play an important role in regulating ETG turbulence with weak/negative-shear plasmas (Idomura 2005). In fact, since the ETG mode with weak/negative shear is essentially slab-type, this observation of the importance of zonal flows is consistent with a preferential generation of secondary large structures like zonal flow (streamers) in weak shear (positive shear) regime found for the slab ETG mode in Li (2005). Even with positive magnetic shear, zonal flows may play an ultimate role in determining the final saturation level in ETG turbulence after a long-time evolution, as shown in Ref. Colyer (2017). Interestingly, this could lead to a collisionality dependence of electron thermal transport driven by the ETG mode due to the collisional damping of ETG zonal flows, which is not found in typical short-time flux-tube ETG mode gyrokinetic simulations. This result could potentially be related to the still-unexplained ST energy confinement scaling dependence on collisionality (Kaye 2007a; Valovič 2011). However, we must caution that it is unclear in Ref. Colyer (2017) whether the predicted electron thermal transport in the late-time low-transport phase is able to match the experimental electron heat flux at the simulated radial location. To address this issue, the dependence of this late-time quasi-stationary low-transport phase on equilibrium quantities (particularly T_e gradient) should be investigated, considering the considerable uncertainties in experimental profile measurements. Particularly, the dependence of the predicted electron thermal transport on T_e gradient should be quantified. We note that the saturation mechanism involving e-GAMs and zonal flows in Wang (2015) might also have a collisionality dependence due to the collisional damping of e-GAMs and zonal flows, which could be promising, since the predicted electron thermal transport already nicely matches the experimental level within experimental uncertainties (see Fig. 34). We also need to caution that the GTS simulation of ETG turbulence in Wang (2015) is based on an NSTX RF-heated L-mode plasma and further investigations using NSTX H-mode equilibria should be carried out to determine the role of e-GAMs and zonal flows in ETG turbulence and their dependence on electron collisionality. The ETG mode is also found to interact with ion-scale modes in the nonlinear phase. The multi-scale interaction is important, since it is only in special situations, e.g., in ITBs and with large E×B shear, that the ETG mode can be treated as standing alone. It is found that ETG turbulence is significantly suppressed by ion-scale turbulence when the ion-scale mode is strongly driven (Görler and Jenko 2008; Howard 2016; Maeyama 2015) and the majority of electron thermal transport is driven by ion-scale turbulence in this case, and there is no clear separation in electron heat flux spectrum between the two scales. On the other hand, when the ion-scale mode is close to marginality, a clear spectral scale separation in the electron heat flux spectrum is observed (Görler and Jenko 2008; Maeyama 2015; Howard 2016), and an enhancement of ion-scale turbulence is also seen due to multi-scale interaction (Howard 2014; Maeyama 2015; Howard 2016), which is attributed to the damping of ion-scale zonal flow by ETG mode streamers (Maeyama 2015; Howard 2016). In contrast, as we have discussed in Sect. 4.2, the nonlinear features of ETG turbulence in the steep-gradientregion of the H-mode pedestal region are quite different from those of ETG turbulence in the core region. In particular, the edge ETG turbulence is characterized by isotropic eddies instead of the typical radially elongated eddies found for the core ETG turbulence, and in addition, the isotropic eddies seem not to be a result of zonal flow regulation, since zonal flows are found to be weak (Told 2012; Hatch 2015; Guttenfelder and Candy 2011), which is different from the observations of breaking up streamers due to large zonal flows that regulate ETG turbulence in simulations with core parameters, e.g., in the regime of which reversed/weak magnetic shear is associated with (Li 2005; Idomura 2005) (also see discussions in Sect. 2.2.3). However, despite the isotropic eddies and much smaller electron-gyro-Bohm unit (due to the lower T_e in the pedestal region), the edge nonlinear ETG gyrokinetic simulations have demonstrated that the edge ETG turbulence can generate experimentally relevant electron thermal transport as a result of the large normalized T_e gradient (Jenko 2009; Told 2012; Hatch 2015, 2016, 2017; Kotschenreuther 2017, 2019; Guttenfelder 2021). Furthermore, since with weak zonal flows, the edge ETG turbulence is not regulated by zonal flow, other saturation mechanisms must be in play, which remains an open question. Thus, as our understanding of the ETG mode deepens, it has become clear that the ETG mode could be a major contributor to electron thermal transport. However, there are major questions still remaining with ETG turbulence as we have discussed.

On the experimental side, there has been plenty of experimental evidence of the ETG mode. There is circumstantial evidence that the observed critical T_e gradient is in agreement with the ETG critical gradient (Hoang 2001; Ryter 2001a) and that the predicted electron heat flux by electron-scale gyrokinetic simulations or multi-scale simulations is in agreement with experimental values (Joiner 2006; Howard 2014, 2015, 2016). Particularly, the multi-scale simulations (Howard 2014, 2015, 2016) are able to explain the puzzling electron thermal transport shortfall observed in L-mode plasmas (White 2013; Howard 2013a, b) and demonstrate that the T_e profile stiffness can only be explained with multi-scale interaction taken into account. Despite these successes, multi-scale simulations for a DIII-D ITER-like discharge show extreme sensitivity to E×B shear with a complete suppression of ion-scale turbulence with the experimental E×B shearing rate, while the corresponding ion-scale simulation shows a comparable ion thermal transport as the experiment. These different results from multi-scale simulations demonstrate that our understanding of the ETG mode and its interaction with ion-scale modes is still limited, and further studies on the reason underlying these discrepancies are needed. We have pointed out that the best evidence of the ETG mode came from direct measurements of electron-scale turbulence. Due to the short-wavelength nature of electron-scale turbulence, coherent scattering diagnostics are usually implemented (Gusakov 2006; Rhodes 2006; Smith 2008; Hillesheim 2015; Barchfeld 2018). With the UHR ES diagnostic on the FT-2 tokamak, positive correlation between measured electron-scale turbulence and the ETG mode critical threshold has been observed (Gusakov 2006; Gurchenko 2010) through edge T_e profile modification by helium puff and a fast current ramp-up. To probe the correlation between electron heat flux and electron-scale turbulence, controlled electron heating experiments were carried out (Gurchenko 2007; Rhodes 2007a, b; Mazzucato 2009), where the correlation between the increased experiment thermal transport and the enhancement in measured electron-scale turbulence was clearly demonstrated. The agreement with the ETG mode linear stability varies, with Gurchenko (2007) and Mazzucato (2009) showing good agreements and Rhodes 2007a only showing agreement at some radii. We would like to point out that detailed experimental studies of the ETG mode (Mazzucato 2009; Smith 2009; Yuh 2009, 2011; Ren 2011, 2012; Ruiz 2015, 2019, 2020) were carried out on NSTX thanks to its large electron gyroradius (easier to measure ETG turbulence), suppressed ion-scale modes due to its large E×B shear and strong plasma shaping and the high-k scattering system that provided a localized turbulence measurement (making it possible to study local parametric dependence). The stabilization of the ETG mode by E×B shear, negative magnetic shear, and density gradient has been clearly demonstrated experimentally, coupled with linear and nonlinear gyrokinetic simulations. We note that a first utilization of a synthetic diagnostic for the NSTX high-scattering system in the validation of the ETG mode physics in an NSTX H-mode plasma has been very successful (Ruiz 2019). On the other hand, the collisionality dependence of ETG turbulence is still an open question for experimental physicists in light of analytic analysis and numerical simulations (Kim 2003; Ren 2012; Wang 2015; Colyer 2017). This is important, since the strong dependence of ST energy confinement scaling on electron collisionality has not been physically understood and understanding the scaling is important for projecting to future ST-based reactors [this is one of the main missions of NSTX-U (Menard et al. 2011)]. Another open question is the experimental proof of the existence of ETG streamers predicted by theories and numerous numerical simulations with core parameters. The existence of ETG streamers is the hallmark of the effectiveness of ETG turbulence in driving electron thermal transport with core parameters. However, its effectiveness in determining electron thermal transport is still being debated (Lin 2005, 2007; Hauff and Jenko 2009; Zhang and Lin 2013). To measure ETG streamers and experimentally study its role in driving electron thermal transport, a coherent scattering system needs to measure the 2D spectral anisotropy in the k_θ and k_r space. The FIR high-k_θ diagnostic (Barchfeld 2018) to be installed on NSTX-U has the potential to make such a measurement and a synthetic diagnostic for the NSTX-U system is being developed (Ruiz 2020). Furthermore, in addition to the core measurements above, measurements of ETG turbulence around the H-mode pedestal region also support the existence of ETG turbulence around the pedestal and its role in driving electron thermal transport (Canik 2011; Hillesheim 2016; Ren 2019a). The isotropic features of the edge ETG turbulence predicted by numerical simulations with H-mode edge parameters (Told 2012; Hatch 2015; Guttenfelder and Candy 2011) could also be addressed in the future by the FIR high-k_θ diagnostic (Barchfeld 2018) to be installed on NSTX-U.

Acknowledgements This work is supported by the U.S. Department of Energy, Office of Science, Office of Fusion Energy Sciences, and has been authored by Princeton University under Contract No. DE-AC02-09CH11466 with the U.S. Department of Energy. The publisher, by accepting the article for publication, acknowledges that the United States Government retains a non-exclusive, paid-up, irrevocable, world-wide license to publish or reproduce the published form of this manuscript, or allow others to do so, for United States Government purposes.

Data availability Data sharing does not apply to this article as no new data were created or analyzed in this article.

Declarations

Conflict of interest S. M. Kaye is an editorial board member for Reviews of Modern Plasma Physics and was not involved in the editorial review or the decision to publish this article. All authors declare that there are no competing interests.

References

R.J. Akers et al., Plasma Phys. Control. Fusion **45**, A175 (2003)
K. Aleynikova et al., J. Plasma Phys. **84**, 745840602 (2018)
T.M. Antonsen, Phys. Rev. Lett. **41**, 33 (1978)
B. Balet et al., Nucl. Fusion **30**, 2029 (1990)
R. Barchfeld et al., Rev. Sci. Instrum. **89**, 10C114 (2018)
M. A. Beer, Ph.D. thesis, Princeton University (1995)
C.D. Beidler et al., Nature **596**, 221 (2021)
A. Bottino et al., Phys. Plasmas **14**, 010701 (2007)
S. Bozhenkov et al., Nucl. Fusion **60**, 066011 (2020)
S.I. Braginskii, *Reviews of Plasma Physiscs, Transport Proccesses in a Plasma* (Consultants Bureau, New York, 1965)
D. Brower et al., Nucl. Fusion **29**, 1247 (1989)
J. Callen et al., Nucl. Fusion **50**, 064004 (2010)
J. Candy et al., Phys. Plasmas **11**, L25 (2004)
J. Candy et al., Plasma Phys. Control. Fusion **49**, 1209 (2007)
J. Candy, R. Waltz, J. Comput. Phys. **186**, 545 (2003)
J.M. Canik et al., Phys. Plasmas **18**, 056118 (2011)
J. Canik et al., Nucl. Fusion **53**, 113016 (2013)
A. Casati et al., Nucl. Fusion **49**, 085012 (2009)
C.S. Chang, F.L. Hinton, Phys. Fluids **25**, 1493 (1982)
L. Chen et al., Plasma Phys. **24**, 743 (1982)
L. Chen et al., Plasma Phys. Control. Fusion **47**, B71 (2005)
Y. Chen, S.E. Parker, J. Comput. Phys. **189**, 463 (2003)
C.Z. Cheng, Phys. Fluids **25**, 1020 (1982)
J. Chowdhury et al., Phys. Plasmas **16**, 082511 (2009)
J. Chowdhury et al., Phys. Plasmas **19**, 102508 (2012)
G.J. Colyer et al., Plasma Phys. Control. Fusion **59**, 055002 (2017)
J.W. Connor et al., Phys. Rev. Lett. **40**, 396 (1978)
J.W. Connor et al., Proc. R. Soc. Lond. A **365**, 1 (1979)
J. Connor et al., Nucl. Fusion **44**, R1 (2004)
B. Coppi et al., Phys. Fluids **10**, 582 (1967)
B. Coppi, F. Pegoraro, Nucl. Fusion **17**, 969 (1977)
B. Coppi, G. Rewoldt, Phys. Rev. Lett. **33**, 1329 (1974)
D. P. Coster et al., *Proc. 22nd Int'l. Atomic Energy Agency Fusion Energy Conference, Geneva, Switzerland, 2008*, *CD-ROM file TH/P4-3* (IAEA, Vienna, 2008)
S.C. Cowley et al., Phys. Fluids B **3**, 2767 (1991)
A.J. Creely et al., Phys. Plasmas **24**, 056104 (2017)
T. Dannert, F. Jenko, Phys. Plasmas **12**, 072309 (2005)
J.C. DeBoo et al., Phys. Plasmas **17**, 056105 (2010)
J.C. DeBoo et al., Phys. Plasmas **19**, 082518 (2012)
P.H. Diamond et al., Plasma Phys. Control. Fusion **47**, R35 (2005)
A.M. Dimits et al., Phys. Rev. Lett. **77**, 71 (1996)
A.M. Dimits et al., Phys. Plasmas **7**, 969 (2000)
A. Dimits et al., Nucl. Fusion **47**, 817 (2007)
S. Ding et al., Nucl. Fusion **60**, 016023 (2019)
J.Q. Dong et al., Phys. Plasmas **9**, 4699 (2002)
J.Q. Dong et al., Phys. Plasmas **9**, 4699 (2002)

J.Q. Dong et al., Nucl. Fusion **43**, 1183–1190 (2003)
W. Dorland, Ph.D. thesis, Princeton University (1993)
W. Dorland et al., Phys. Rev. Lett. **85**, 5579 (2000)
J.F. Drake et al., Phys. Rev. Lett. **44**, 994 (1980)
J.F. Drake et al., Phys. Rev. Lett. **61**, 2205 (1988)
D. R. Ernst et al., *Proc. 20th Int'l. Atomic Energy Agency Fusion Energy Conference, Vilamoura, Portugal, 1–6 November 2004*, *CD-ROM file TH/4-1* (IAEA, Vienna, 2004)
D. R. Ernst et al., *Proceeding of 21st Int'l. Atomic Energy Agency Fusion Energy Conference, Chengdu, China, 2006*, *CD-ROM file TH/1-3* (IAEA, Vienna, 2006), available as http://www-pub.iaea.org/MTCD/Meetings/FEC2006/th_1-3.pdf
D.R. Ernst et al., Phys. Plasmas **16**, 055906 (2009)
D.E. Evans et al., Plasma Phys. **24**, 819 (1982)
D.E. Evans et al., Plasma Phys. **25**, 617 (1983)
H. Evensen et al., Nucl. Fusion **38**, 237 (1998)
R. Farengo et al., Phys. Fluids B **1**, 2181 (1989)
L. Feng et al., Chin. Phys. Lett. **22**, 1170 (2005)
A. R. Field et al., *Proc. 20th Int'l. Atomic Energy Agency Fusion Energy Conference, Vilamoura, Portugal, 1-6 November 2004*, *CD-ROM file EX/P2-11* (IAEA, Vienna, 2004)
J. Freidberg, *Ideal Magnetohydrodynamics, Cellular Organelles* (Plenum Press, ADDRESS, 1987)
A. Fujisawa, Nucl. Fusion **49**, 013001 (2008)
T. Fujita et al., Phys. Rev. Lett. **78**, 2377 (1997)
H.P. Furth et al., Phys. Fluids **6**, 459 (1963)
Z. Gao et al., Phys. Plasmas **8**, 2816 (2001)
Z. Gao et al., Phys. Plasmas **12**, 022502 (2005)
X. Garbet et al., Nucl. Fusion **50**, 043002 (2010)
K.W. Gentle et al., Phys. Plasmas **13**, 012311 (2006)
T. Görler, F. Jenko, Phys. Rev. Lett. **100**, 185002 (2008)
C. Gormezano et al., Nucl. Fusion **47**, S285 (2007)
R.G. Greaves et al., Plasma Phys. Control. Fusion **34**, 1253 (1992)
M. Greenwald et al., Phys. Rev. Lett. **53**, 352 (1984)
J. Guang-De, D. Jia-Qi, Chin. Phys. **13**, 898 (2004)
A. Gurchenko et al., Nucl. Fusion **47**, 245 (2007)
A.D. Gurchenko et al., Plasma Phys. Control. Fusion **52**, 035010 (2010)
A.D. Gurchenko, E.Z. Gusakov, Plasma Phys. Control. Fusion **52**, 124035 (2010)
E.Z. Gusakov et al., Plasma Phys. Control. Fusion **48**, A371 (2006)
E.Z. Gusakov et al., Plasma Phys. Control. Fusion **48**, B443 (2006)
W. Guttenfelder et al., Phys. Rev. Lett. **106**, 155004 (2011)
W. Guttenfelder et al., Nucl. Fusion **53**, 093022 (2013)
W. Guttenfelder et al., Nucl. Fusion **59**, 056027 (2019)
W. Guttenfelder et al., Nucl. Fusion **61**, 056005 (2021)
W. Guttenfelder, J. Candy, Phys. Plasmas **18**, 022506 (2011)
T.S. Hahm, K.H. Burrell, Phys. Plasmas **2**, 1648 (1995)
T.S. Hahm, W.M. Tang, Phys. Fluids B **1**, 1185 (1989)
V.H. Hall-Chen et al., Plasma Phys. Control. Fusion **64**, 095002 (2022)
G.W. Hammett et al., Plasma Phys. Control. Fusion **35**, 973 (1993)
M.R. Hardman et al., Plasma Phys. Control. Fusion **61**, 065025 (2019)
M.R. Hardman et al., J. Plasma Phys. **86**, 905860601 (2020)
D. Hatch et al., Nucl. Fusion **55**, 063028 (2015)
D. Hatch et al., Nucl. Fusion **56**, 104003 (2016)
D. Hatch et al., Nucl. Fusion **57**, 036020 (2017)
T. Hauff, F. Jenko, Phys. Plasmas **16**, 102306 (2009)
R.J. Hawryluk, *Phys. Plasma Close Thermonuclear Conditions* (Pergamon, New York, 1981)
R.D. Hazeltine, H.R. Strauss, Phys. Rev. Lett. **37**, 102 (1976)
P. Helander, G.G. Plunk, Phys. Plasmas **22**, 090706 (2015)
J.C. Hillesheim et al., Nucl. Fusion **55**, 073024 (2015)
J.C. Hillesheim et al., Plasma Phys. Control. Fusion **58**, 014020 (2016)
F.L. Hinton, R.D. Hazeltine, Rev. Mod. Phys. **48**, 239 (1976)
A. Hirose, Phys. Fluids B **2**, 850 (1990)

A. Hirose, Phys. Plasmas **7**, 433 (2000)
A. Hirose et al., Phys. Plasmas **9**, 1659 (2002)
A. Hirose, M. Elia, Phys. Plasmas **9**, 4664 (2002)
M. Hirsch et al., Rev. Sci. Instrum. **72**, 324 (2001)
G.T. Hoang et al., Phys. Rev. Lett. **87**, 125001 (2001)
C. Holland, Phys. Plasmas **23**, 060901 (2016)
C. Holland et al., Nucl. Fusion **57**, 066043 (2017)
C. Holland, P.H. Diamond, Phys. Plasmas **11**, 1043 (2004)
E. Holzhauer et al., Plasma Phys. Control. Fusion **40**, 1869 (1998)
W. Horton and et al., *Plasma Physics and Controlled Nuclear Fusion Research(Nice, France, 1990) (Vienna:International Atomic Energy Agency) vol 2, p 211* (IAEA, Vienna, 1990)
W. Horton et al., Phys. Fluids **24**, 1077 (1981)
W. Horton et al., Phys. Fluids **31**, 2971 (1988)
W. Horton, Rev. Mod. Phys. **71**, 735 (1999)
W. Horton et al., Phys. Plasmas **7**, 1494 (2000)
W. Horton et al., New J. Phys. **5**, 14 (2003)
N.T. Howard et al., Phys. Plasmas **20**, 032510 (2013)
N. Howard et al., Nucl. Fusion **53**, 123011 (2013)
N.T. Howard et al., Phys. Plasmas **21**, 112510 (2014)
N.T. Howard et al., Plasma Phys. Control. Fusion **57**, 065009 (2015)
N.T. Howard et al., Phys. Plasmas **23**, 056109 (2016)
N. Howard et al., Nucl. Fusion **56**, 014004 (2016)
N.T. Howard et al., Phys. Plasmas **28**, 072502 (2021)
Y. Idomura et al., Phys. Plasmas **6**, 4658 (1999)
Y. Idomura et al., Phys. Plasmas **7**, 2456 (2000a)
Y. Idomura et al., Phys. Plasmas **7**, 3551 (2000b)
Y. Idomura et al., Nucl. Fusion **45**, 1571 (2005)
Y. Idomura, J. Comput. Phys. **313**, 511 (2016)
A. Jacchia et al., Nucl. Fusion **42**, 1116 (2002)
S. Janhunen et al., Plasma Phys. Control. Fusion **64**, 015005 (2021)
F. Jenko et al., *in International School of Plasma Physics* (Theory of Fusion Plasmas, Societa Italiana di Fisica, Editrice Compositori Bologna, 2002)
F. Jenko et al., Phys. Plasmas **7**, 1904 (2000)
F. Jenko et al., Phys. Plasmas **8**, 4096 (2001)
F. Jenko, J. Plasma Fusion Res. SERIE **6**, 11 (2004)
F. Jenko et al., Phys. Plasmas **16**, 055901 (2009)
F. Jenko et al., in High Performance Computing, in *Science and Engineering, Garching/Munich 2007*. ed. by S. Wagner et al. (Springer, Berlin, 2009), pp.275–289
F. Jenko, W. Dorland, Phys. Rev. Lett. **89**, 225001 (2002)
X. Jian et al., Nucl. Fusion **58**, 016011 (2017)
X. Jian et al., Phys. Rev. Lett. **123**, 225002 (2019)
N. Joiner et al., Plasma Phys. Control. Fusion **48**, 685 (2006)
B.B. Kadomitsev, O.P. Pogutse, *Reviews of Plasma Physiscs, Turbulence in Toroidal Systems* (Consultants Bureau, New York, 1970)
B.B. Kadomtsev, Sov. J. Plasma Phys. (Engl. Transl.); (United States) **1**, 295 (1975)
B.B. Kadomtsev, O.P. Pogutse, Sov. Phys. JETP **24**, 1172 (1967)
B.B. Kadomtsev, O.P. Pogutse, Sov. Phys. Dokl. **14**, 470 (1969)
B. Kadomtsev, O. Pogutse, Nucl. Fusion **11**, 67 (1971)
C. Kawai et al., Phys. Plasmas **27**, 082302 (2020)
S.M. Kaye et al., Nucl. Fusion **47**, 499 (2007)
S.M. Kaye et al., Phys. Rev. Lett. **98**, 175002 (2007)
S. Kaye et al., Nucl. Fusion **59**, 112007 (2019)
C. Kessel et al., Phys. Rev. Lett. **72**, 1212 (1994)
J.Y. Kim et al., Phys. Fluids B **5**, 4030 (1993)
E.-J. Kim et al., Phys. Rev. Lett. **91**, 075003 (2003)
E.-J. Kim, P.H. Diamond, Phys. Plasmas **10**, 1698 (2003)
J.Y. Kim, W. Horton, Phys. Fluids B **3**, 3194 (1991)
J.E. Kinsey et al., Phys. Plasmas **15**, 055908 (2008)

M. Kotschenreuther et al., Comp. Phys. Comm. **88**, 128 (1995)
M. Kotschenreuther et al., Nucl. Fusion **57**, 064001 (2017)
M. Kotschenreuther et al., Nucl. Fusion **59**, 096001 (2019)
N. Kumar et al., Nucl. Fusion **61**, 036005 (2021)
B. Labit, M. Ottaviani, J. Plasma Phys. **73**, 199–206 (2007)
M. Landreman et al., Phys. Rev. Lett. **114**, 095003 (2015)
B.P. LeBlanc et al., Rev. Sci. Instrum. **74**, 1659 (2003)
Y. Lee et al., Nucl. Fusion **20**, 482 (1980)
Y.C. Lee et al., Phys. Fluids **30**, 1331 (1987)
G.S. Lee, P.H. Diamond, Phys. Fluids **29**, 3291 (1986)
F.M. Levinton et al., Phys. Plasmas **14**, 056119 (2007)
J. Li et al., Nucl. Fusion **45**, 1293 (2005)
J. Li, Y. Kishimoto, Phys. Plasmas **9**, 1241 (2002)
J. Li, Y. Kishimoto, Phys. Rev. Lett. **89**, 115002 (2002)
J. Li, Y. Kishimoto, Phys. Plasmas **10**, 683 (2003)
J. Li, Y. Kishimoto, Phys. Plasmas **11**, 1493 (2004)
J. Li, Y. Kishimoto, Phys. Plasmas **15**, 112504 (2008)
Z. Lin et al., Science **281**, 1835 (1998)
Z. Lin et al., Phys. Rev. Lett. **88**, 195004 (2002)
Z. Lin et al., Phys. Plasmas **12**, 056125 (2005)
Z. Lin et al., Phys. Rev. Lett. **99**, 265003 (2007)
B. Lloyd et al., Plasma Phys. Control. Fusion **46**, B477 (2004)
S. Maeyama et al., Comput. Phys. Commun. **184**, 2462 (2013)
S. Maeyama et al., Plasma Fusion Res. **8**, 1403150 (2013)
S. Maeyama et al., Phys. Rev. Lett. **114**, 255002 (2015)
S. Maeyama et al., Phys. Rev. Lett. **119**, 195002 (2017)
S. Maeyama et al., Nucl. Fusion **57**, 066036 (2017)
S. Maeyama et al., Phys. Plasmas **28**, 052512 (2021)
S. Maeyama et al., Nat. Commun. **13**, 3166 (2022)
P. Maget et al., Nucl. Fusion **39**, 949 (1999)
E. Mazzucato, Phys. Fluids **21**, 1063 (1978)
E. Mazzucato, Phys. Plasmas **10**, 753 (2003)
E. Mazzucato et al., Phys. Rev. Lett. **101**, 075001 (2008)
E. Mazzucato et al., Nucl. Fusion **49**, 055001 (2009)
B.F. McMillan et al., Phys. Rev. Lett. **105**, 155001 (2010)
J. Menard et al., *2011 IEEE/NPSS 24th Symposium on Fusion Engineering (SOFE)*, pp. 1–8
J.E. Menard et al., Phys. Rev. Lett. **97**, 095002 (2006)
J. Menard et al., Nucl. Fusion **56**, 106023 (2016)
S. Migliuolo, Phys. Lett. A **198**, 341 (1995)
R.L. Miller et al., Phys. Plasmas **5**, 973 (1998)
A. Mishchenko et al., Plasma Phys. Control. Fusion **64**, 104009 (2022)
M. Nakata et al., Phys. Plasmas **19**, 022303 (2012)
M. Nakata, M. Honda, Plasma Fusion Res. **17**, 1403083 (2022)
W.M. Nevins et al., Phys. Plasmas **12**, 122305 (2005)
W.M. Nevins et al., Phys. Plasmas **13**, 122306 (2006)
W.M. Nevins et al., Phys. Plasmas **14**, 084501 (2007)
H. Nordman et al., Nucl. Fusion **30**, 983 (1990)
K.M. Novik, A.D. Piliya, Plasma Phys. Control. Fusion **36**, 357 (1994)
T. Ohkawa, Phys. Lett. A **67**, 35 (1978)
ITER Physics Expert Group on Confinement et al., Nuclear Fusion **39**, 2175 (1999)
L. Onsager, Phys. Rev. **37**, 405 (1931)
J.F. Parisi et al., Nucl. Fusion **60**, 126045 (2020)
S.E. Parker et al., AIP Conf. Proc. **871**, 193 (2006)
B. Patel et al., Nucl. Fusion **62**, 016009 (2021)
J. Peterson, Ph.D. thesis, Princeton University, Princeton, NJ 08544, 2011
J.L. Peterson et al., Phys. Plasmas **19**, 056120 (2012)
C. Petty et al., Nucl. Fusion **56**, 016016 (2015)
E.J. Doyle et al., Nucl. Fusion **47**, S18 (2007)

T. Rafiq et al., Phys. Plasmas **20**, 032506 (2013)
Y. Ren et al., Phys. Rev. Lett. **106**, 165005 (2011)
Y. Ren et al., Phys. Plasmas **19**, 056125 (2012)
Y. Ren et al., Nucl. Fusion **53**, 083007 (2013)
Y. Ren et al., Nucl. Fusion **57**, 072002 (2017)
Y. Ren et al., Nucl. Fusion **59**, 096045 (2019a)
Y. Ren et al., Nucl. Fusion **60**, 026005 (2019b)
Y. Ren et al., Plasma Phys. Control. Fusion **65**, 075007 (2023)
C.L. Rettig et al., Phys. Plasmas **8**, 2232 (2001)
T.L. Rhodes et al., Rev. Sci. Instrum. **77**, 10E922 (2006)
T. Rhodes et al., Nucl. Fusion **47**, 936 (2007)
T.L. Rhodes et al., Phys. Plasmas **14**, 056117 (2007a)
T.L. Rhodes et al., Plasma Phys. Control. Fusion **49**, B183 (2007b)
P. Ricci et al., Phys. Plasmas **18**, 032109 (2011)
B.N. Rogers et al., Phys. Rev. Lett. **85**, 5336 (2000)
F. Romanelli, Phys. Fluids B **1**, 1018 (1989)
M. Romanelli et al., Phys. Plasmas **11**, 3845 (2004)
D.W. Ross, S.M. Mahajan, Phys. Rev. Lett. **40**, 324 (1978)
V.A. Rozhanskii, JETP Lett. **34**, 60 (1981)
J.R. Ruiz et al., Phys. Plasmas **22**, 122501 (2015)
J.R. Ruiz et al., Plasma Phys. Control. Fusion **61**, 115015 (2019)
J.R. Ruiz et al., Phys. Plasmas **27**, 122505 (2020)
F. Ryter et al., Phys. Rev. Lett. **86**, 5498 (2001)
F. Ryter et al., Phys. Rev. Lett. **86**, 2325 (2001)
F. Ryter et al., Plasma Phys. Control. Fusion **43**, A323 (2001)
F. Ryter et al., Phys. Rev. Lett. **95**, 085001 (2005)
F. Ryter et al., Plasma Phys. Control. Fusion **48**, b453 (2006)
L. Schmitz et al., Nucl. Fusion **52**, 023003 (2012)
K.C. Shaing, Phys. Fluids **31**, 2249 (1988)
Y. Shen et al., Nucl. Fusion **59**, 106011 (2019)
H. Shirai, Phys. Plasmas **5**, 1712 (1998)
P.K. Shukla et al., J. Plasma Phys. **44**, 393–404 (1990)
P. Shukla, J. Weiland, Phys. Lett. A **137**, 132 (1989)
R. Singh et al., Phys. Plasmas **20**, 112506 (2013)
R.E. Slusher, C.M. Surko, Phys. Fluids **23**, 472 (1980)
D.R. Smith et al., Rev. Sci. Instrum. **79**, 123501 (2008)
D.R. Smith et al., Phys. Rev. Lett. **102**, 225005 (2009)
D.R. Smith et al., Rev. Sci. Instrum. **83**, 10D502 (2012)
S. Smith et al., Nucl. Fusion **55**, 083011 (2015)
A.I. Smolyakov et al., Phys. Rev. Lett. **89**, 125005 (2002)
G.M. Staebler et al., Phys. Plasmas **12**, 102508 (2005)
G. Staebler et al., Nucl. Fusion **57**, 066046 (2017)
B.W. Stallard et al., Phys. Plasmas **6**, 1978 (1999)
D. Stutman et al., in *2007 34th European Physical Society Conf. on Plasma Physics, Warsaw, Poland, 2-6 July 2007 P2.061* (2007)
D. Stutman et al., *Proc. 20th Int'l. Atomic Energy Agency Fusion Energy Conference, Vilamoura, Portugal, 1-6 November 2004*, *CD-ROM file EX/P2-8* (IAEA, Vienna, 2004)
H. Sugama et al., Phys. Plasmas **3**, 2379 (1996)
P. Sun et al., Nucl. Fusion **58**, 016003 (2017)
W. Tang, Nucl. Fusion **18**, 1089 (1978)
W. Tang et al., Nucl. Fusion **20**, 1439 (1980)
D. Told, Ph.D. thesis, University of Ulm (2012)
D. Told et al., Phys. Plasmas **15**, 102306 (2008)
K.T. Tsang et al., Phys. Rev. Lett. **40**, 327 (1978)
M. Valovič et al., Nucl. Fusion **51**, 073045 (2011)
L. Villard et al., Plasma Phys. Control. Fusion **52**, 124038 (2010)
R.E. Waltz et al., Phys. Plasmas **14**, 056116 (2007)
G. Wang et al., Phys. Plasmas **18**, 082504 (2011)

W.X. Wang et al., Phys. Plasmas **14**, 072306 (2007)
W.X. Wang et al., Phys. Plasmas **17**, 072511 (2010)
W.X. Wang et al., Phys. Plasmas **22**, 102509 (2015)
T.-H. Watanabe, H. Sugama, Nucl. Fusion **46**, 24 (2005)
A.E. White et al., Phys. Plasmas **20**, 056106 (2013)
R. Wolf et al., Nucl. Fusion **41**, 1259 (2001)
K. Wong et al., Phys. Lett. A **236**, 339 (1997)
K. Yao et al., J. Instrum. **15**, P12016 (2020)
S. Yi et al., Phys. Plasmas **23**, 102514 (2016)
H.Y. Yuh et al., Phys. Plasmas **16**, 056120 (2009)
H.Y. Yuh et al., Phys. Rev. Lett. **106**, 055003 (2011)
W. Zhang, Z. Lin, Phys. Plasmas **20**, 102306 (2013)
A. Zocco et al., Plasma Phys. Control. Fusion **57**, 085003 (2015)
H. Zohm, Plasma Phys. Control. Fusion **38**, 105 (1996)